A Doctoral Dissertation

Study on the Stern Shape Optimization of a Container Ship using Navier-Stokes Analysis

(ナビエ．ストークス解析を用いたコンテナ船の船尾形状最適化に関する研究)

Graduate School of Engineering

Yokohama National University

Nguyen Duy Trong

(グェン.ズゥイ.チョン)

September, 2015

This thesis is submitted to the Graduate School of Engineering - Yokohama Nation University, in partial fulfillment of the requirements for the degree of Doctor of Engineering. It is entirely my own work except where otherwise state by references or acknowledgments.

Nguyen Duy Trong

Acknowledgement

The opportunity to study at Yokohama National University (YNU) is a wonderful and unforgettable experience in my life. This thesis marks the end of 5 years with much learning in numerical method, flow analysis as well as ship hydrodynamic of both the Master and PhD courses at YNU. All these knowledges could not be acquired without people who has been part. Before present the achieved results, let me say thank to all those who have pulled me through this period and made my stay at YNU be a pleasant one.

First of all, I would like to express my deepest gratitude to my advisor - Professor Hino, for his encouragement, right direction as well as his patience when revise my papers, thesis and supports in my researches, for teaching me many things from basic to expert knowledge of CFD over the past five years from the Master course. This dissertation would not be possible without his supervisions.

Special thanks to Professor Suzuki for giving me an opportunity to come to Japan and do my Master course and his recommendation to Professor Hino after that. I would also like to extend my gratitude to all professors of Department of System Designs for Ocean-Space Engineering (YNU) for giving interesting lectures and supporting my research activities.

I am deeply thankful to the committee members, Prof. Arai, Prof. Suzuki, Prof. Hirakawa and Prof. Miyaji for their valuable comments and suggestions to this research.

Sincere appreciations and thanks are also extended to my tutors Mr. Tokunaga, Mr. Hirano who had given their valuable time on discussions, supports and great helps me from the first day I came to Japan with much strange. I also appreciate Mr. Okada for valuable helps during my research period. My gratitude is dedicated to all my colleagues, friends as well as all student members of the Ship Hydrodynamic Laboratory for making my life in Japan become more convenient and enjoyable.

I gratefully acknowledge the financial support of Japan Ministry of Education, Culture, Sports, Science and Technology (MEXT) during the course of this study.

Last but not the least, I want to extends my special thanks and love to my parents, sisters and my lovely friend for inspiring me. They are sources of my strength and power to complete my research.

Abstract

Optimizing hull form design is playing a more important role in the shipbuilding industry, especially when regulations on the environmental protection and improvement of ship energy efficiency become more stringent than ever. Though the studies on design optimization of ship hull form have a long history and also achieved some significant results, studies on the stern shape optimization of a ship hull have been still a few due to the complexity of flow field behind a ship stern. In this study, a numerical method for optimizing the stern shape of a container ship based on a nonlinear programming method and a Navier-Stokes analysis is proposed. A CFD solver which solves the three-dimensional Reynolds Averaged Navier-Stokes (RANS) equations for incompressible flows is used for evaluation of an objective function and analysis of flow fields around ship hulls. The Sequential Quadratic Programming (SQP) method is utilized as an optimizer which automatically determines values of the design variables in such a way that the objective function is minimized subject to the given constraints. Design variables are selected so that the modified transom shapes are efficiently created through the optimization process. Finally, to demonstrate the applicability of the present method, a transom stern of a container ship is selected for the optimization processes to minimize the pressure resistance coefficient at a model scale. Furthermore, the effects of the initial designs and of the shape modification functions to the optimized results are also examined in this study. The optimized results show that the present optimization system is able to create a stern shape that decreases the pressure resistance coefficient; however, it turns out that special cares should be taken in the selection of the initial designs and the hull form modification functions since the optimization results strongly depend on these parameters.

Table of Contents

Acknowledgement ii

Abstract iv

Table of Contents v

List of Figures vii

List of Tables x

1 Introduction 1

1.1 Background and Motivation 1

1.2 Objectives of this study 3

1.3 Organization of the thesis 4

2 Optimization method 5

2.1 The Sequential Quadratic Program 6

2.2 Navier-Stokes solver 8

2.2.1 Governing Equation 8

2.2.2 Spatial Discretization 10

2.2.2.1 Spatial Discretization 10

2.2.2.2 Discretization of the inviscid fluxes 11

2.2.2.3 Discretization of viscous fluxes 13

2.2.2.4 Time integration 15

2.2.3 Boundary Condition 17

2.2.4 Turbulence Model 18

2.2.5 Free Surface Treatment 20

2.2.5.1 Re-initialization 23

2.2.5.2 Flow Variable Extrapolation 23

2.3 Hull form modification method 25

3 Application **30**

3.1 The initial hull form and computational conditions 30

3.2 Optimized results and Discussions 33

3.2.1 Verification and Validation for CFD solver 33

3.2.2 Optimized results of the optimization process with $x_{st} = 0.51$. . . 39

3.2.3 Effects of the initial design variable value (x_{st}) to the optimization results 48

3.2.4 Effects of the weight function to the final optimization results . . . 59

3.2.5 Dependences of the optimized results on the initial designs and modification functions 66

3.2.6 Grid dependency study 72

4 Concluding Remarks **74**

Appendix **76**

A Computed pressure resistance coefficients **76**

A.1 The computed pressure resistance coefficients using linear function 76

A.2 The computed pressure resistance coefficients using sine function 78

References **81**

List of Figures

2.1 Outline of the optimization process. 5
2.2 Three main elements of the optimization problem. 6
2.3 Cell shapes 10
2.4 Schematic sketch of cell and face indices. 11
2.5 Control volume for the evaluation of velocity gradient. 14
2.6 Pressure condition on free surface 24
2.7 Comparison of the modification methods. 26
2.8 The hull form modification method. 27
2.9 Comparison of framelines by using different modification functions. . . . 29

3.1 Overhangs of the initial KCS and modified ship hull. 30
3.2 Bottom profiles and frame lines at the stern plane of the KCS and modified hull forms. 31
3.3 Computational grid. 32
3.4 Computational grids around transom stern of KCS Container Ship used in V&V procedure 33
3.5 Comparison of the computed and measured wave profile along the KCS hull form. 34
3.6 Computational grids around transom stern of KCS Container Ship used in V&V procedure 37
3.7 History of the objective function of the optimization process with $x_{st} = 0.51$ 39
3.8 Design values of the design variables in the optimization process using $x_{st} = 0.51$ 39
3.9 Overhangs of the initial and optimized hull forms. 40
3.10 Centerline profiles and framelines of the initial and optimized hull forms with $x_{st} = 0.51$ 41
3.11 Pressure patterns on the hull surface of the fore parts. 42
3.12 Pressure distributions on the overhang surfaces 43

3.13 Pressure patterns on the hull surface of the aft parts (backview). 43
3.14 The longitudinal distributions of pressure and frictional components of resistance. 44
3.15 Wave patterns around transom sterns. 45
3.16 Wave profiles behind the stern end of ship hulls 45
3.17 Streamlines in the center plane of ship hulls. 46
3.18 Streamlines at the stern end plane and wakes. 47
3.19 Overhangs of the initial hull forms with different initial values of design variable x_{st}. 48
3.20 Comparisons of the centerline profiles and framelines of the initial hull forms by using $x_{st} = 0.5$ and $x_{st} = 0.51$. 49
3.21 Comparison of histories of the objective function of the optimization process using $x_{st} = 0.5$ and $x_{st} = 0.51$. 51
3.22 Histories of the design values of the optimization process using $x_{st} = 0.5$. 51
3.23 Centerline profiles and framelines of the optimized ship hulls by using different initial designs of $x_{st} = 0.5$ and 0.51. 52
3.24 Overhangs of the initial and optimized hull forms by using $x_{st} = 0.5$. . . . 53
3.25 Pressure distributions on the initial and the optimized overhang surfaces by using $x_{st} = 0.5$. 54
3.26 Pressure distributions on the initial and the optimized hull surfaces in the aft parts using $x_{st} = 0.5$. 54
3.27 The longitudinal distribution of pressure and frictional resistances of ship hulls using $x_{st} = 0.5$ 55
3.28 Wave patterns around the initial and optimized transom sterns using $x_{st} = 0.5$. 56
3.29 Wave profiles behind the stern ends of ship hulls using $x_{st} = 0.5$. 56
3.30 The simulated streamlines under initial and optimized transom bottoms using $x_{st} = 0.5$. 57
3.31 Streamlines and the axial distribution of velocity at the stern end plane of the initial and optimized hull forms by using $x_{st} = 0.5$. 58
3.32 Pressure reduction during the optimization processes using different weight function. 59
3.33 Histories of the design variable values during the optimization process using sine weight function. 60

3.34 Comparison of the optimized overhang by using linear and sine functions. 61
3.35 Bottom profiles at the center plane and framelines at the stern end plane ($x/L_{pp} = 0.526$) of the optimized hull forms using different functions. . . 62
3.36 Pressure patterns on the optimized overhang surfaces by using different modification functions. 63
3.37 Pressure distributions on the aft part of the optimized hull surfaces by using the linear and sine weight functions. 64
3.38 Wave patterns around the optimized transom sterns using the linear and sine weight functions. 64
3.39 Comparison of the streamlines in the center plane of the optimized ship hulls by using the different modification functions. 65
3.40 Comparison of streamlines and wakes at the stern end plane of optimized hull form using different modification functions. 66
3.41 Dependence of the optimized results on the initial designs and modification functions. 67
3.42 Comparison of the initial and optimized overhangs 69
3.43 Comparison of the initial and optimized overhangs. 70
3.44 Contours of the pressure resistance coefficient of the hull form generated by different design variables values. 71
3.45 Computational grids around the ship stern. 72

List of Tables

3.1 Principal paticulars. 31
3.2 Grid convergence study of resistance coefficients of the KCS model . . . 38
3.3 Verified results of the resistance coefficients 38
3.4 Resistance coefficients of the initial and optimized ship hulls with $x_{st} = 0.51$. 40
3.5 The computed trim, sinkage and dipping of the fore and aft perpendiculars of the initial and optimized hull forms with $x_{st} = 0.51$. 42
3.6 The computed resistance coefficients of the initial and optimized hull forms using $x_{st} = 0.5$. 51
3.7 Trim, sinkage and dipping of the fore, aft perpendiculars of the initial and optimized ship hulls using $x_{st} = 0.5$. 55
3.8 The computed resistance coefficients. 60
3.9 Optimization cases. 67
3.10 Optimized values of the design variables. 67
3.11 Sensitivity analysis the gradient of the objective function of the Case I. . . 68
3.12 Sensitivity analysis the gradient of the objective function of the Case II. . 69
3.13 Comparison of the grid dimensions 73
3.14 The computed resistance coefficients. 73

A.1 Computed pressure resistance coefficient using the linear modification function 76
A.2 Computed pressure resistance coefficient using the sine modification function 78

Chapter 1

Introduction

1.1 Background and Motivation

In some recent years, with the accelerating globalization of the world economy, demands for the transportation especially for the sea transportation have been continuously increasing. Keeping up with these demands, the shipbuilding industry have been also developing and now are playing a more important role in the world trade. However, the urgent issues of the environmental protection and increase of fuel cost at the same time make the shipbuilding industry be facing with many challenges. In order to reduce emission of the greenhouse effect gas, the International Maritime Organization (IMO) have released and amended the mandatory measures of Energy Efficiency Design Index (EEDI) applied for new ships, Ship Energy Efficiency Management Plan (SEEMP) applied for all ships and benchmarks of enhancing ship energy efficiency [1, 2]. In these circumstances, design optimization of a ship hull is acknowledged to be one of the most effective and efficient solutions to improve ship efficiency as well as to satisfy the environmental protection criterion. In general, it can be said that study on the hull form design optimization has a long history with many interests of ship designers and researchers. It has also achieved some important results that have been being utilized in the practical designs such as bulbous bow [3], Kawasaki Stern End Wedge [4], ducktail waterline extension [5] and so forth.

With much progress has been made in the development of robust and efficient computational approaches in the last decade, the current Computational Fluid Dynamic (CFD) methods can provide a good evaluation of ship resistance and accurate predictions of flow field that contains both viscous and free-surface effects nowadays. While the development of CFD methods continues unabatedly, the applications of these methods to real world problems become industrial practice in the shipbuilding industry. The successful calcu-

lations and simulations of ship resistances and flow fields can be found in some research works [6, 7]. Based on achievements of the computational techniques, design a ship hull by analyzing the simulated results using a CFD method is being considered as another efficient manner in addition to the conventional towing test based design procedures. There have been also some studies utilizing the numerical techniques and optimization methods to minimize the user defined objective functions.

In the hull form optimization using the numerical flow analysis, taking the advantages of fast computation in evaluation of the objective functions, the potential flow solver is used first. For instance, Suzuki et al. [8] optimized the stern hull form of SR221 and HTC container ship models to minimize energy of the secondary flows. The optimized stern hull form reduced 10% of the drag resistance in case of the SRR221B ship model and depending on each constrain condition, the drag resistance of the HTC container ship reduced 3% - 7%. In order to minimize wave making resistance around the hull forms, Zang [9, 10] optimized the Series 60 (S60) hull form and bulbous bow of a container ship.

Though the potential flow solvers can give the evaluated result of the objective functions during the optimization process fast, the potential flow solver itself is not suitable for simulation of real flows that contain both viscous and free-surface effects. The optimization system based on the Navier-Stokes equations that can solve well flows containing both viscous and free surface effects, therefore, have been also developed. Hino [11] and Tahara et al. [12, 13, 14] developed successfully the optimization systems based on solving RANS equations to optimize ship hull forms that reduces significantly the user defined objective functions.

On the other hand, the optimization studies have also expanded the objective functions from the single objectives to multi-objectives. Tahara et al. [12] developed an optimization system for optimizing the stern shape of a tanker. The selected objective functions are the delivered horsepower and overshoot angle. He also developed an optimization system for optimizing hull surface of a combatant model (DTMB-5415). Parsons et al. [15] developed a method for establishment of the initial parameters of a stern flap in the preliminary design, which can be a baseline design for use in a subsequent program and also can be utilized again to provide multi-criterion optimization to establish the final design parameters for the stern flap.

Recently, the optimization studies have applied not only for mono hull forms but also for multi-hull forms. Tahara et al. [14] developed an optimization method for minimizing

the total drag resistance of a high-speed sealift research model (HSSL-B). Kim and Yang [16] applied the radius basis function interpolation for optimization of the delft-trimaran model. Saha et al. [17] used the Rankine Source method for optimization of a catamaran with large bow and stern bulbs installed at the center plane and so forth.

Despite the studies on hull form design optimization have been attracted many interests and achieved some significant results, the optimization study, particularly for the stern shape of a ship hull has been still limited. In general it can be said that the design optimization of a transom shape or the aft part is more difficult than these of the fore part and of the bulbous. Influences of the turbulent flow, effects of transom configurations and hull propeller interactions make flow field behind the ship stern extremely complicated. It can also be said that most of the studies on stern shape optimization have widely used the frameline modification functions which change breadth and modify the frameline curves of ship hulls [8, 11]. Some experimental studies have shown that the transom configurations and appendages have significant effects on hydrodynamic resistance components and flow field behind the ship stern [18–21]. The main factors defining the stern shape of a ship hull are the transom height, bottom profile together with the frameline curves of the overhang shape. Though determining the transom height and stern shape are an important step in the optimization process, numerical studies on determination of the transom height and the bottom profile by using a CFD method have been still a few. In this study, a numerical method for finding the transom height, bottom profile and frameline curves of the stern shape of a container ship hull is proposed.

1.2 Objectives of this study

The main objective of this study is to describe the development of a numerical method for the stern shape optimization of a container ship hull. As mentioned before, most of the previous studies on the stern shape optimization have used the modification functions that modify only the breadth and framline curves of a hull. With the constrains assigned on the design variables, variations of the framelines somehow are limited. Also effects of the modified framlines on flow fields around the modified ship hull are not so much. In this study, the hull form modification function is applied for not only the frameline modification but also for determination of the transom height at the stern end and bottom profile curves. Since the transom height is not fixed, it is expected that the present hull form modification method has greater flexibility than the previous approaches. The

optimized hull form is also expected to be more optimized and have better performance. In order to demonstrate the applicability of the optimization system, the stern shape of a container ship hull is optimized to minimize the pressure resistance coefficient. Besides, in order to investigate the effects of the initial design and of the frameline modification functions to the optimized hull forms, the optimization processes using different initial designs and modification functions are also carried out and then the optimized results are compared with each other.

1.3 Organization of the thesis

This thesis is organized as 4 chapters. In the chapter 1, a summary of the previous studies on hull form optimization, motivation and objectives of this study are presented.

Chapter 2 presents the optimization method used in this study. Brief description on the mathematical form of the optimization system based on the SQP (Sequential Quadratic Programming (SQP) method are presented. The details of the hull form modification function together with CFD solver are also described in this chapter.

Chapter 3 shows the achieved results of the optimization applications. Results of the investigations on effects of the initial design values and of the hull form modification functions are also described in details. In addition, results of the grid dependency test for one representative case are also provided to validate the optimized results.

Chapter 4 is a brief conclusion of this study. Suggestions for future works are also presented in this chapter.

Chapter 2

Optimization method

In general, the optimization problems are solved systematically by iterative evaluation of the objective functions. It can be briefly described as follows (Figure 2.1):

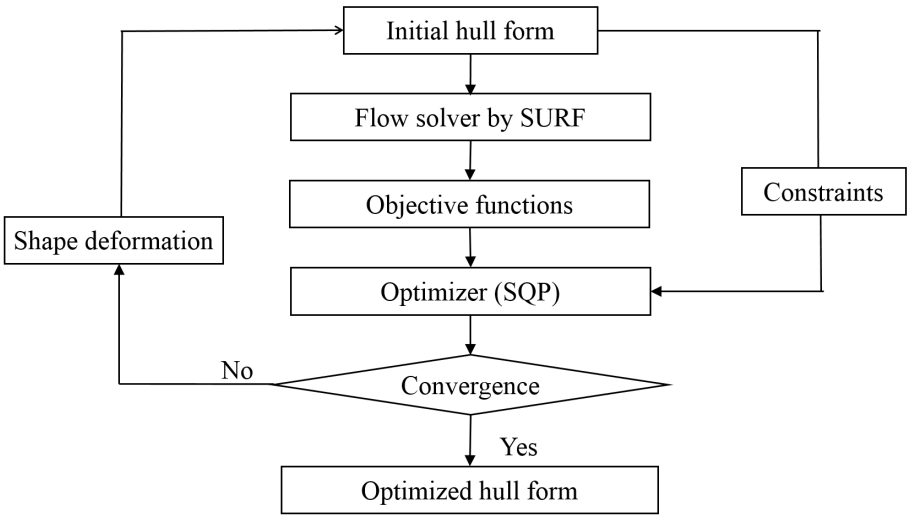

Figure 2.1: Outline of the optimization process.

1. Determine values of the design variables $\boldsymbol{D}$. Values of the design variables are given by user at the beginning then determined by SQP procedure in the following steps during the optimization process.

2. Define a hull form corresponding to the given values of the design variables. The computational grid around the new ship hull is regenerated. The hull modification and grid generator tools are used in this step.

3. The CFD solver is used to compute the flow field surrounding a ship hull by using the computational grid obtained in 2.

4. Compute the objective function F and constraints by using the flow field $\boldsymbol{Q}$ and the hull geometry defined by $\boldsymbol{D}$.

5. The sensitivity coefficients of both objective function and constraints are evaluated by using the finite difference method.

6. The SQP method is used to determine values of the design variables $\boldsymbol{D}$ for the next steps.

7. If value of the objective function converges or satisfies certain criteria, the optimization process finishes. Otherwise, return to 2.

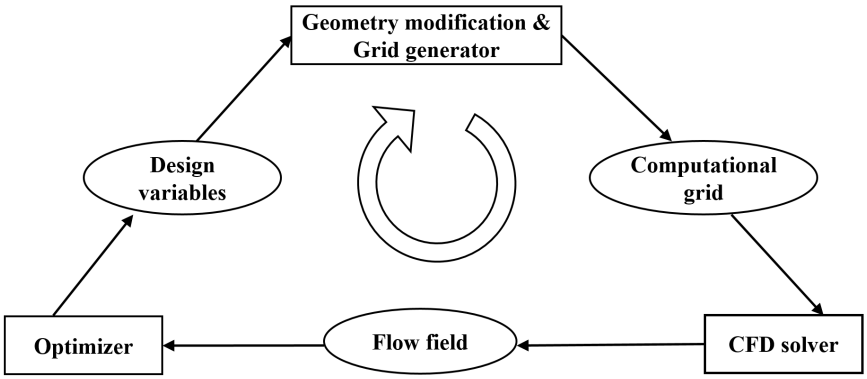

Figure 2.2: Three main elements of the optimization problem.

As shown in Figure 2.2, three main components of an optimization system are a nonlinear optimizer, a CFD solver and a hull shape modification method together with a grid generator. In the present study, the SQP method is utilized as an optimizer which automatically determines values of the design variables. A SURF v6.46 which solves the three-dimensional Reynolds Averaged Navier-Stokes equations for incompressible flows is used for evaluation of the objective function and analysis of flow fields around ship hulls. The details of each item are described in the subsequent sections followed by its applications.

2.1 The Sequential Quadratic Program

The Sequential quadratic programming (SQP) is an iterative method for nonlinear optimization problems and has proven as one of the most successful methods for the

numerical solution of the constrained nonlinear optimization problems. It relies on a profound theoretical foundation and provides powerful algorithm for the solution of larger-scale technologically relevant problems [22]. Assume that the general form of a hull form optimization problem can be written as follows [11]:

$$\begin{aligned} &\text{Minimize} && F\left[\boldsymbol{D}, \boldsymbol{Q}\left(\boldsymbol{D}\right)\right] \\ &\text{Subject to} && C_i\left[\boldsymbol{D}, \boldsymbol{Q}\left(\boldsymbol{D}\right)\right] = 0, \quad i = 1, M_E \\ & && C_i\left[\boldsymbol{D}, \boldsymbol{Q}\left(\boldsymbol{D}\right)\right] \geq 0, \quad i = M_E + 1, M \end{aligned} \tag{2.1}$$

where F is an objective function to be minimized and it is dependent on $\boldsymbol{D}$ and $\boldsymbol{Q}$. $\boldsymbol{D}$ is the vector of design variables which is used to define a ship hull. $\boldsymbol{Q}$ is the vector of flow variables, thus, it is a function of hull geometry $\boldsymbol{D}$. $C_i = 0$ and $C_i \geq 0$ are equality and inequality constraints, respectively. Note that, C_i is either the function of $\boldsymbol{D}$ only (geometric constraint) or the function of $\boldsymbol{D}$ and flow field $\boldsymbol{Q}$ which is determined by the Navier-Stokes analysis.

When the current design point $\boldsymbol{D}^{(k)}$ is determined, the next design point $\boldsymbol{D}^{(k+1)}$ is evaluated as follows. First, the following quadratic programming problem is solved to obtain the search vector $\boldsymbol{d}$:

$$\begin{aligned} &\text{Minimize} && \nabla F[\boldsymbol{D}^{(k)}]^T \boldsymbol{d} + \frac{1}{2} \boldsymbol{d}^T \boldsymbol{B}^{(k)} \boldsymbol{d} \\ &\text{Subject to} && C_i[\boldsymbol{D}^{(k)}] + \nabla C_i[\boldsymbol{D}^{(k)}]^T \boldsymbol{d} = 0, \quad i = 1, M_E \\ & && C_i[\boldsymbol{D}^{(k)}] + \nabla C_i[\boldsymbol{D}^{(k)}]^T \boldsymbol{d} \geq 0, \quad i = M_E + 1, M \end{aligned} \tag{2.2}$$

In the above equations, objective function F is approximated as the quadratic function of $\boldsymbol{D}^{(k)}$ and the constraints are approximated as the linear functions of $\boldsymbol{D}^{(k)}$. $\boldsymbol{B}$ is an approximation to the Hessian matrix of the Lagrange function $L[\boldsymbol{D}, \boldsymbol{u}]$ as follows:

$$\boldsymbol{B} \approx \nabla^2 L\left[\boldsymbol{D}, \boldsymbol{u}\right] = \nabla^2 \left(F[\boldsymbol{D}] - \sum_{i=1}^{M} u_i C_i[\boldsymbol{D}] \right) \tag{2.3}$$

where $\boldsymbol{u} = (u_1, u_2, \ldots)^T$ are the Lagrange multipliers.

The next design point $\boldsymbol{D}^{(k+1)}$ is obtained by the line search along the vector $\boldsymbol{d}$. Step size t is determined in such a way that the following penalty functions:

$$F[\boldsymbol{D}] + r \left(\sum_{i=1}^{M_E} |C_i[\boldsymbol{D}]| + \sum_{i=M_E+1}^{M} |\min\left(0, C_i[\boldsymbol{D}]\right)| \right) \tag{2.4}$$

becomes smaller than a certain value with r being a parameter. Finally, the next design point is computed by:

$$\boldsymbol{D}^{(k+1)} = \boldsymbol{D}^{(k)} + t^{(k)} \boldsymbol{d}^{(k)} \tag{2.5}$$

And the design iteration continues until the convergence criterion are satisfied.

In the SQP methods, the gradients of the objective function (∇F) and of the constraints (∇C_i) with respect to the design variables which are called the sensitivity coefficients are required. The sensitivity coefficients can be simply evaluated by using the finite difference of solutions with a slight perturbation of the design variables. Grid generations and flow computations, therefore, should be repeated as many times as number of the design variables.

The sensitivity coefficients, (∇F) and (∇C_i) can be analytically expressed as follows (only the objective function F is used in the following discussion, the fluid dynamic constraints can be treated similarly):

$$\nabla F = \left(\frac{\partial F}{\partial D_1}, \frac{\partial F}{\partial D_2}, \ldots, \frac{\partial F}{\partial D_j}, \ldots \right)^T \tag{2.6}$$

where $\boldsymbol{D} = \left(D_1, D_2, \ldots, D_j, \ldots \right)$ is the vector of design variables. The gradient of the objective function F with respect to the design variable D_j is evaluated by the central finite difference approximation as follows:

$$\frac{\partial F}{\partial D_j} = \frac{F[D_1, \ldots, D_j + \varepsilon_j, \ldots] - F[D_1, \ldots, D_j - \varepsilon_j, \ldots]}{2\varepsilon_j} \tag{2.7}$$

with ε_j being the step size of the design variable D_j. The procedure for estimation of the gradient of the constraints is carried out in the similar way.

2.2 Navier-Stokes solver

2.2.1 Governing Equation

The CFD code used in this study is SURF[1] v6.46 that has been developed at National Maritime Research Institute - Japan. SURF is an advanced CFD code that has been developed as a practical ship design tool and now being used in many shipyards in Japan. Successful computations and simulations of ship resistances and free-surfaces by using SURF could be found in some research works [6, 7, 23].

In the SURF code, the governing equations to be solved are the three-dimensional Reynolds averaged Navier-Stokes (RANS) equations for incompressible flows. The final vector form using non-dimensional variables of the flow equations in the Cartesian

[1] Solution algorithm for Unstructured RANS with FVM.

coordinate system can be written as follows [24, 25]:

$$\frac{\partial \vec{q}}{\partial t} + \frac{\partial(\vec{e} - \vec{e}^{v})}{\partial x} + \frac{\partial(\vec{f} - \vec{f}^{v})}{\partial y} + \frac{\partial(\vec{g} - \vec{g}^{v})}{\partial z} = 0 \tag{2.8}$$

where $\vec{q} = [p, \ u, \ v, \ w]^T$ is the vector of flow variables which consists of pressure p and (u, v, w) - the velocity components in the (x, y, z) directions. Note that, to achieve the above final form, the artificial compressibility is included into the continuity equation to couple pressure with a velocity field. And, to exclude the gravitational acceleration term in the z-momentumn equation, pressure p is modified as

$$p = p^* + \frac{z}{Fn^2}$$

where p^* is the original pressure and Fn is the Froude number.

The inviscid fluxes $\vec{e}, \vec{f}$ and $\vec{g}$ are defined as:

$$\vec{e} = \begin{bmatrix} \beta u \\ u^2 + p \\ uv \\ uw \end{bmatrix}, \quad \vec{f} = \begin{bmatrix} \beta v \\ vu \\ v^2 + p \\ vw \end{bmatrix}, \quad \vec{e} = \begin{bmatrix} \beta w \\ wu \\ wv \\ w^2 + p \end{bmatrix}$$

where β is a parameter for artificial compressibility. $\vec{e}^{v}, \vec{f}^{v}$ and $\vec{g}^{v}$ are the viscous fluxes defined as follows:

$$\vec{e}^{v} = \begin{bmatrix} 0 \\ \tau_{11} \\ \tau_{12} \\ \tau_{13} \end{bmatrix}, \quad \vec{f}^{v} = \begin{bmatrix} 0 \\ \tau_{21} \\ \tau_{22} \\ \tau_{23} \end{bmatrix}, \quad \vec{g}^{v} = \begin{bmatrix} 0 \\ \tau_{31} \\ \tau_{32} \\ \tau_{33} \end{bmatrix}$$

where

$$\tau_{ij} = \left(\frac{1}{Rn} + \nu_t\right)\left(\frac{\partial u_i}{\partial x_j} + \frac{\partial u_j}{\partial x_i}\right)$$

with $(x_1, x_2, x_3) = (x, y, z)$ and $(u_1, u_2, u_3) = (u, v, w)$. In the above expressions, all the variables are made dimensionless using the reference density ρ, velocity U and length L. Rn is the Reynolds number defined as UL/ν where ν is the kinematic viscosity. ν_t is the non-dimensional kinematic eddy viscosity determined by a turbulence model.

2.2.2 Spatial Discretization

2.2.2.1 Spatial Discretization

Spatial discretization of the solution scheme is based on a finite-volume method for an unstructured grid. Cell shape of the present solver that can cope with are tetrahedron, prism, pyramid or hexahedron and face shapes are either triangular or quadrilateral as shown in Figure 2.3 [24, 25]

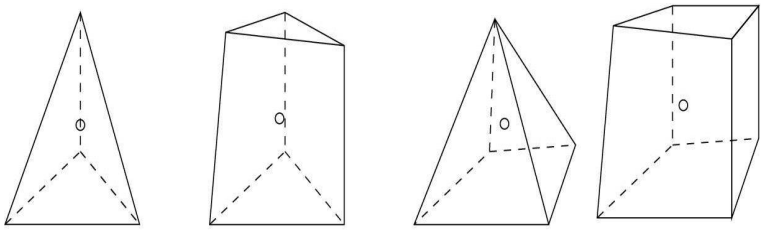

Figure 2.3: Cell shapes

These four types of cells give better flexibility in handling complex geometries. In particular, it is suitable for a hybrid grid approach in which prisms and hexahedra are placed in the region close to a solid wall for the efficient resolution of boundary layers while tetrahedron and pyramids are used in handling the remaining region in a flexible manner. A cell centered layout is adopted which means flow variables $\vec{q}$ are defined at the centroid of each cell and a control volume is a cell by itself.

Integrating form of the Equation (2.8) over a cell volume V_i yields [24]:

$$\iiint_{V_i} \left[\frac{\partial \vec{q}}{\partial t} + \frac{\partial(\vec{e} - \vec{e}^{v})}{\partial x} + \frac{\partial(\vec{f} - \vec{f}^{v})}{\partial y} + \frac{\partial(\vec{g} - \vec{g}^{v})}{\partial z} \right] dV = 0 \tag{2.9}$$

The first term in the integral can be expressed as the product of the cell volume V_i and the time derivative of the cell averaged value of flow variables $\vec{q}_i$, since the grid is stationary in the current applications. The remaining terms are converted into surface integration over cell faces using the divergence theorem. This yields the semi-discrete form of the governing equation as follows:

$$V_i \frac{dq_i}{dt} + \sum_j F_{i+j/2} - \sum_j R_{(i+j)/2} = 0 \tag{2.10}$$

where i is a cell index and j is the index of next cells of the cell i. Subscript $(i + j)/2$ denotes the face between cells i and j as shown in Figure 2.4. Equation (2.10) is solved

using 2nd order upwind scheme based on flux difference splitting in space and Euler implicit scheme in time [24].

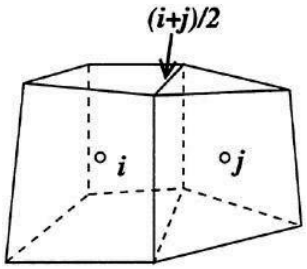

Figure 2.4: Schematic sketch of cell and face indices.

$\boldsymbol{F}$ and $\boldsymbol{R}$ are the inviscid and viscous fluxes and be defined as:

$$\boldsymbol{F} = eS_x + fS_y + gS_z \tag{2.11}$$

$$\boldsymbol{R} = e^v S_x + f^v S_y + g^v S_z \tag{2.12}$$

where (S_x, S_y, S_z) are the (x, y, z)-components of the area vector of a cell face in the direction from the cell i to the cell j.

2.2.2.2 Discretization of the inviscid fluxes

Components of the inviscid fluxes $\boldsymbol{F}$ can be written as [24, 26]:

$$\boldsymbol{F}(q) = \begin{pmatrix} \beta_{ac} U \\ uU + pS_x \\ vU + pS_y \\ wU + pS_z \end{pmatrix} \tag{2.13}$$

where $U = uS_x + vS_y + wS_z$. The inviscid fluxes are evaluated by the upwind scheme based on the flux-difference splitting of Roe [27]. In this scheme, the numerical fluxes are computed as

$$F_{(i+j)/2} = \frac{1}{2}\left[F(q^R) + F(q^L) - |A|(q^R - q^L)\right] \tag{2.14}$$

where q^R, q^L are the flow variables on the right and left sides of a cell face, respectively. $|A|$ is defined in the following way. First, let A be the Jacobian of the inviscid flux $\boldsymbol{F}$ at a cell face:

$$A = \frac{\partial \boldsymbol{F}}{\partial q} \tag{2.15}$$

where the flow variables at the cell face $q_{(i+j)/2}$ are evaluated by using simple average of the right and the left side values, i.e.,

$$q_{(i+j)/2} = \frac{1}{2}(q^R + q^L) \tag{2.16}$$

The eigenvalues of $\boldsymbol{A}$ are $U, U, U + c, U - c$ where c is the pseudo-speed-of sound and be as defined as

$$c = \sqrt{U^2 + \beta_{ac}(S_x^2 + S_y^2 + S_z^2)} \tag{2.17}$$

By using the right-eigenvector $\boldsymbol{R}$, $\boldsymbol{A}$ can be expressed as

$$\boldsymbol{A} = \boldsymbol{R}\boldsymbol{\Lambda}\boldsymbol{R}^{-1} \tag{2.18}$$

where $\boldsymbol{\Lambda}$ is

$$\boldsymbol{\Lambda} = \mathrm{diag}(U, U, U + c, U - c) \tag{2.19}$$

Finally, $|\boldsymbol{A}|$ is given by

$$\boldsymbol{A} = \boldsymbol{R}|\boldsymbol{\Lambda}|\boldsymbol{R}^{-1} \tag{2.20}$$

with

$$|\boldsymbol{\Lambda}| = \mathrm{diag}(|U|, |U|, |U + c|, |U - c|) \tag{2.21}$$

To archive the second order accuracy in space, the MUSCL approach is used in which the flow variables $\boldsymbol{q}$ is reconstructed as a linear polynomial function inside each cell using the cell centroid values. Let the scalar quantity q be a component of $\boldsymbol{q}$ and q is assumed to be linearly varying in the vicinity of the cell i, i.e.,

$$q(\boldsymbol{x}) = q_i + \nabla q_i(\boldsymbol{x} - \boldsymbol{x}_i)) \tag{2.22}$$

where $\nabla q_i = (\partial q_i/\partial x, \partial q_i/\partial y, \partial q_i/\partial z)^T$ is the gradient of q at the cell i and $\boldsymbol{x}_i$ is the coordinates of the cell centroid i. This equation is applied to the cell j which is adjacent to the cell i, which yields

$$q_j = q_i + \nabla q_i(x_j - x_i) \tag{2.23}$$

or

$$(x_j - x_i)\nabla q_i = q_j - q_i \tag{2.24}$$

A similar equation can be written for all the neighbor cells of i, thus,

$$\begin{bmatrix} \Delta x_1 & \Delta y_1 & \Delta z_1 \\ \Delta x_2 & \Delta y_2 & \Delta z_2 \\ \vdots & \vdots & \vdots \\ \Delta x_3 & \Delta y_3 1 & \Delta z_3 \end{bmatrix} \begin{pmatrix} \dfrac{\partial q_i}{\partial x} \\ \dfrac{\partial q_i}{\partial y} \\ \dfrac{\partial q_i}{\partial z} \end{pmatrix} = \begin{pmatrix} q_1 - q_i \\ q_2 - q_i \\ \vdots \\ q_m - q_i \end{pmatrix} \tag{2.25}$$

where

$$\Delta x_j = x_j - x_i$$

The above equation gives the overdetermined system for ∇q_i and the least squares solution can be obtained by solving it via QR decomposition. Finally, $\boldsymbol{q}^R$ and $\boldsymbol{q}^L$ are extrapolated using the gradient with the limiter function as follows

$$\boldsymbol{q}^L = \boldsymbol{q}_i + \Phi \nabla q_i (\boldsymbol{x}_{(i+j)/2} - \boldsymbol{x}_i) \tag{2.26}$$

$$\boldsymbol{q}^R = \boldsymbol{q}_j + \Phi \nabla q_j (\boldsymbol{x}_{(i+j)/2} - \boldsymbol{x}_j) \tag{2.27}$$

where $\boldsymbol{x}_{(i+j)/2}$ is the coordinates of the center of face $(i + j)/2$.

The limiter function Φ is used to enforce the monotonicity of the reconstruction. The form proposed by Barth [28, 29] is used in the present scheme which is written as:

$$\Phi = \begin{cases} \min\left(1, \dfrac{q^{\max} - q_i}{q_{(i_j)/2} - q_i}\right) & \text{if} \quad q_{(i+j)/2} - q_i > 0 \\ \min\left(1, \dfrac{q^{\min} - q_i}{q_{(i_j)/2} - q_i}\right) & \text{if} \quad q_{(i+j)/2} - q_i < 0 \\ 1 & \text{if} \quad q_{(i+j)/2} - q_i = 0 \end{cases} \tag{2.28}$$

where $q^{\max}$ and $q^{\min}$ are the maximum and minimum values of q at the cell i and its neighbors.

2.2.2.3 Discretization of viscous fluxes

The viscous fluxes components can be briefly described as [24, 30]:

$$\boldsymbol{R}(\boldsymbol{q}) = \begin{pmatrix} 0 \\ S_x \tau_{xx} + S_y \tau_{xy} + S_z \tau_{xz} \\ S_x \tau_{yx} + S_y \tau_{yy} + S_z \tau_{yz} \\ S_x \tau_{zx} + S_y \tau_{zy} + S_z \tau_{zz} \end{pmatrix} \tag{2.29}$$

The computation of $\boldsymbol{R}_{(i+j)/2}$ requires velocity gradient on a cell face. These are computed again by applying the divergence theorem to another control volume surrounding a cell face as shown in Figure 2.5.

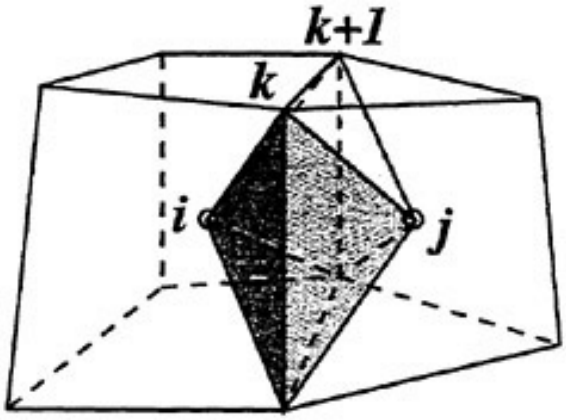

Figure 2.5: Control volume for the evaluation of velocity gradient.

The values of $\boldsymbol{q}$ at the centroids i and j as well as at the nodes surrounding the face $(i+j)/2$ $(k, k+1, \ldots)$ are used for the surface integration. For example, $\partial u/\partial x$ is computed as:

$$\begin{aligned}\frac{\partial u}{\partial x_{(i+j)/2}} &= \frac{1}{V^*}\sum_{\text{Faces}} uS_x \\ &= \frac{1}{V^*}\left(\frac{u_i+u_k+u_{k+1}}{3}S_{x,i,k,k+1} + \frac{u_j+u_k+u_{k+1}}{3}S_{x,j,k,k+1}\right)\end{aligned} \tag{2.30}$$

where V^* is the volume of the current control volume and $S_{x,\alpha,\beta,\gamma}$ is the x-component of the outward area vector of the face formed by the nodes α, β and γ. This formulation is equivalent to centered differencing in the structured grid case and is second order accuracy.

The velocity values at the nodes $k, k+1$ etc. are computed from the values at the cell centroids by the Laplacian weighted average as follows [31]:

$$\boldsymbol{q}_k = \frac{\sum_j w_j \boldsymbol{q}_j}{\sum_j w_j} \tag{2.31}$$

where the summation is for all the cells that share the node k. The weight w_j is computed as:

$$w_j = 1 + \lambda_x(x_j - x_k) + \lambda_y(y_j - y_k) + \lambda_z(z_j - z_k) \tag{2.32}$$

where λ_x, λ_y and λ_z are the solution of

$$\begin{bmatrix} I_{xx} & I_{xy} & I_{xz} \\ I_{yx} & I_{yy} & I_{yz} \\ I_{zx} & I_{zy} & I_{zz} \end{bmatrix} \begin{pmatrix} \lambda_x \\ \lambda_y \\ \lambda_z \end{pmatrix} = \begin{pmatrix} R_x \\ R_y \\ R_z \end{pmatrix} \tag{2.33}$$

with

$$I_{xx} = \sum_j (x_j - x_k)^2 \quad I_{yy} = \sum_j (y_j - y_k)^2 \quad I_{zz} = \sum_j (z_j - z_k)^2$$
$$I_{xy} = \sum_j (x_j - x_k)(y_j - y_k) \quad I_{yz} = \sum_j (y_j - y_k)(z_j - z_k) \quad I_{zx} = \sum_j (z_j - z_k)(x_j - x_k)$$
$$R_x = \sum_j (x_j - x_k) \quad R_y = \sum_j (y_j - y_k) \quad R_z = \sum_j (z_j - z_k)$$

This formulation gives the exact values for linearly varying functions and is second order accuracy.

2.2.2.4 Time integration

With the introduction to the artificial compressibility into the governing equations, incompressible flow fields then can be obtained only as a steady state limit. Therefore, transient solutions are not physically valid. The time integration in the present scheme is thus the way to drive solutions to a steady state and time accuracy of the scheme is not important [24, 26].

The first order backward Euler scheme is used for the time integration in which the governing equation is written as

$$V_i \frac{\Delta \boldsymbol{q}_i}{\Delta t_i} + \sum_j F^{n+1}_{(i+j)/2} - \sum_j R^{n+1}_{(i+j)/2} = 0 \tag{2.34}$$

where

$$\Delta q = q^{n+1} - q^n$$

and the superscripts denote the time step. Δt_i is time increment in local time stepping in which Δt_i is determined cell by cell in such a way that the CFL number is globally constant as follows

$$\Delta t_i = CFL \frac{V_i}{\sum\limits_{Faces} (|U| + c)} \tag{2.35}$$

where CFL is the CFL number. The summation of the denominator is taken over all faces of the current cells.

The linearization of the inviscid flux F^{n+1} with respect to time is made as follows

$$\boldsymbol{F}^{n+1} = \boldsymbol{F}^n + \frac{\partial \boldsymbol{F}}{\partial \boldsymbol{q}} \Delta \boldsymbol{q} \tag{2.36}$$

When the Jacobian $\partial \boldsymbol{F}/\partial \boldsymbol{q}$ is evaluated, the flux $\boldsymbol{F}$ is computed with the first order upwind scheme by setting

$$\boldsymbol{q}^L = \boldsymbol{q}_i$$
$$\boldsymbol{q}^R = \boldsymbol{q}_j$$

i.e., the inviscid flux is approximated by

$$\boldsymbol{F}_{(i+j)/2} \approx \frac{1}{2}\left[\boldsymbol{F}(q_j) + \boldsymbol{F}(q_i) + |\boldsymbol{A}|(q_j - q_i)\right] \tag{2.37}$$

Thus, $\partial \boldsymbol{F}/\partial \boldsymbol{q}.\Delta q$ is expressed as

$$\frac{\partial \boldsymbol{F}}{\partial \boldsymbol{q}}\Delta \boldsymbol{q} = \frac{1}{2}\left[\boldsymbol{A}_j \cdot \Delta \boldsymbol{q}_j + \boldsymbol{A}_i \cdot \Delta \boldsymbol{q}_i - |A| \cdot (\Delta \boldsymbol{q}_j - \Delta \boldsymbol{q}_i)\right] \tag{2.38}$$

where

$$\boldsymbol{A}_i = \frac{\partial \boldsymbol{F}(q)_i}{\partial \boldsymbol{q}_i}$$

In the similar manner, the viscous flux is linearized in time as

$$\boldsymbol{R}^{n+1} = \boldsymbol{R}^n + \frac{\partial \boldsymbol{R}}{\partial \boldsymbol{q}} \cdot \Delta \boldsymbol{q} \tag{2.39}$$

For the evaluation of the Jacobian $\partial \boldsymbol{R}/\partial \boldsymbol{q}$, the velocity gradients are approximated by neglecting the contribution from the values at the nodes $\boldsymbol{q}_k$, etc. Equation (2.30) is replaced by

$$\begin{aligned} \frac{\partial u}{\partial x_{(i+j)/2}} &= \frac{1}{V*}\sum_{\text{Faces}} uS_x \\ &\approx \frac{1}{V^*}\left(\frac{u_i}{3}S_{x,i,k,k+1} + \frac{u_j}{3}S_{x,j,k,k+1} + \ldots\right) \\ &= \frac{S_x}{3V^*}(u_j + u_i) \end{aligned} \tag{2.40}$$

where S_x is the area vector component of the face $(i + j)/2$ as defined above. Using the similar approximation for the other velocity gradients, $\boldsymbol{R}$ can be written as

$$\boldsymbol{R} \approx \boldsymbol{B} \cdot (\boldsymbol{q}_j - \boldsymbol{q}_i) \tag{2.41}$$

where

$$\boldsymbol{B} = \frac{(1/R + \nu_t)}{3V^*} \times \begin{bmatrix} 0 & 0 & 0 & 0 \\ 0 & S^2 + S_x^2 & S_xS_y & S_xS_z \\ 0 & S_yS\,x & S^2 + S_y^2 & S_yS_z \\ 0 & S_zS_x & S_yS_z & S^2 + S_x^2 \end{bmatrix}$$

Thus, $\partial \boldsymbol{R}/\partial \boldsymbol{q} \cdot \Delta \boldsymbol{q}$ becomes

$$\frac{\partial \boldsymbol{R}}{\partial \boldsymbol{q}} \cdot \Delta \boldsymbol{q} \approx \boldsymbol{B}(\Delta \boldsymbol{q}_j - \Delta \boldsymbol{q}_i)$$

And, Equation (2.34) now becomes

$$V_i \frac{\Delta \boldsymbol{q}_i}{\Delta t_i} + \sum_j F^n_{(i+j)/2} - \sum_j R^n_{(i+j)/2} + \sum_j \frac{1}{2}\left[\boldsymbol{A}_j \cdot \Delta \boldsymbol{q}_j + \boldsymbol{A}_i \cdot \Delta \boldsymbol{q}_i - |\boldsymbol{A}| \cdot (\Delta \boldsymbol{q}_j - \Delta \boldsymbol{q}_i)\right] \quad (2.42)$$

The Δ terms are rearranged into a form as follows

$$\left[\frac{V_i}{\Delta t_i}\boldsymbol{I} + \sum_j \left(\frac{\boldsymbol{A}_i + |\boldsymbol{A}|}{2} + \boldsymbol{B}\right)\right] \cdot \Delta \boldsymbol{q}_i + \sum_j \left[\left(\frac{\boldsymbol{A}_j - |\boldsymbol{A}|}{2} - \boldsymbol{B}\right) \cdot \Delta \boldsymbol{q}_i\right] = -\left(\sum_j F^{n+1}_{(i+j)/2} - \sum_j R^{n+1}_{(i+j)/2}\right) \quad (2.43)$$

The above equation is a linear equation with respect to $\Delta \boldsymbol{q}$. In order to solve this equation, the Symmetric Gauss-Seidel (SGS) iteration is adopted. And, to improve convergent speed, the cells are ordered from upstream to downstream in the preprocessing stage. The Gauss-Seidel sweep is carried out form the upstream cell to the downstream first, then the second sweep follows in the reverse order. The following sweeps change the direction alternately.

2.2.3 Boundary Condition

The cell faces on the boundaries are classified as the boundary faces. The boundary conditions are implemented by giving the approximate fluxes on the boundary faces based on the following conditions [24, 25]:

Solid wall:

$$\frac{\partial p}{\partial n} = 0, \quad u = v = w = 0$$

Inflow:

$$\frac{\partial p}{\partial n} = 0, \quad (u, v, w) = (\text{Uniform flow})$$

Outflow:

$$p = 0, \quad \frac{\partial u}{\partial n} = \frac{\partial v}{\partial n} = \frac{\partial w}{\partial n} = 0$$

Side:

$$\frac{\partial p}{\partial n} = \frac{\partial u}{\partial n} = \frac{\partial v}{\partial n} = \frac{\partial w}{\partial n} = 0$$

Symmetry:

Symmetric Conditions

In case of the Dirichlet conditions, the fluxes can be computed using given values, while in case of the Neumann conditions, that flow variables on the faces is set equal to those at the cell that contains the current faces. In the time integration process, all the boundary conditions are treated implicitly.

2.2.4 Turbulence Model

A turbulence model is indispensable for simulation of the high Reynolds number flows from the practical point of view. There are a number of turbulence models ranged from simple algebraic models or one-or two equations models for the eddy viscosity concept to Reynolds stress models for the second order closure. However, no model has been proved to be universally applicable to general fluid engineering problems. In practice, a turbulence model should be selected based on the characteristics of a flow field of each problem. Ship flows, particularly stern flows, are extremely complicated because they are essentially three dimensional separated flows with strong longitudinal vortices and free surface effects can not be neglected in some cases. These extremely complicated ship flows are beyond the capability of most of existing turbulence models [24, 32].

Since the original Spallart - Allmaras turbulence model is known to be relatively simple and yet produce reasonable predictions for ship flows, especially flows at bow and stern. To cope with these difficulties, SURF code has adapted a newly proposed evaluation of the vorticity component in production term and has obtained Modified Spalart-Allmaras turbulence model which has proven better than original model in simulation flow field at bow and stern [33]. In the present study, the Modified Spalart-Allmaras turbulence model is utilized for simulation of the free surface flow and analysis of effects of transom shape on the stern waves. The original Spallart-Allmaras model is a one equation model which solves a transport equation for a viscosity - like variable $\tilde{\nu}$ and be described mathematically as below [32, 34].

The eddy viscosity ν_t is defined by:

$$\nu_t = \tilde{\nu} f_{v1}, \; f_{v1} \frac{\chi^3}{\chi^3 + C_{v1}^3}, \; \chi := \frac{\tilde{\nu}}{\nu}$$

with ν is the molecular viscosity, $\tilde{\nu}$ is determined by solving the transport equation defined

as following:

$$\begin{aligned}\frac{\partial\tilde{\nu}}{\partial t}+u_j\frac{\partial\tilde{\nu}}{\partial x_j}=&C_{b1}\left[1-f_{t2}\right]\tilde{S}\,\tilde{\nu}+\frac{1}{\sigma}\left\{\nabla\cdot\left[\left(\frac{1}{Re}+\tilde{\nu}\right)\nabla\tilde{\nu}\right]+C_{b2}\left|\nabla\nu\right|^2\right\}\\&-\left[C_{w1}f_w-\frac{C_{b1}}{\kappa^2}f_{t2}\right]\left(\frac{\tilde{\nu}}{d}\right)^2+f_{t1}\nabla U^2\end{aligned}\tag{2.44}$$

Here

$$\tilde{S}=|\omega|+\frac{\tilde{\nu}}{\kappa^2d^2}f_{v2},\quad f_{v2}=1-\frac{\chi}{1+\chi f_{v1}}$$

where ω is the magnitude of the vorticity, and d is the distance to the closet wall. The function f_w is:

$$f_w=g\left[\frac{1+c_{w3}^6}{g^6+c_{w3}^6}\right]^{1/6}$$

where

$$g=r+c_{w2}\left(r^6-r\right),\ r\equiv\frac{\tilde{\nu}}{\tilde{S}\,\kappa^2d^2}$$

$$f_{t1}=c_{t1}g_t\exp\left(-c_{t2}\frac{\omega_t^2}{\nabla U^2}\left[d^2+g_t^2d_t^2\right]\right),\ g_t\equiv\min\left(0.1,\nabla U/\omega_t\nabla x_t\right)$$

The function f_{t2} is:

$$f_{t2}=c_{t3}\exp\left(-c_{t4}\chi^2\right)$$

The constants are:

$$\begin{aligned}&c_{b1}=0.135,\sigma=2/3,c_{b2}=0.622,\kappa=0.41,c_{w1}=c_{b1}/\kappa^2+(1+c_{b2})/\sigma,\\&c_{w2}=0.3,c_{w3}=2,c_{v1}=7.1,c_{t1}=1,c_{t2}=2,c_{t3}=1.2,c_{t4}=0.5\end{aligned}$$

The right hand terms of the Equation (2.44) represent the production, diffusion, destruction and trip.

The original Spalart-Allmaras turbulence model over-predicts the level of eddy viscosity in the core of a vortex and thus produce excessive diffusion. In order to reduce the eddy viscosity calculated from the original model in the stern area, the vorticity component $|\omega|$ is modified as follows:

$$|\omega|\rightarrow|\omega|+\mathrm{C}\min\left(0,|S|-|\omega|\right)$$

where $|S|$ is the magnitude of the strain - rate tensor. The advantage of this formulation is that the eddy viscosity is reduced in the regions where the magnitude of the vorticity exceeds that of the strain rate, such as in the vortex core. On the other hands, the axial vortex correction is passive in thin shear layers where $|S|$ and $|\omega|$ are very close. C is an arbitrary constant and set to 20 in the SURF code [33].

2.2.5 Free Surface Treatment

In the ship hydrodynamic applications, the free surface is an interface between air and water. Free surface conditions consist of dynamic and kinematic conditions and they are implemented in the interface capturing framework [7, 30].

The kinematic condition is the condition that fluid particles on a free surface remain on an interface. This is written in a mathematical form as follows [7]:

$$\frac{DH}{Dt} \equiv \frac{\partial H}{\partial t} + u\frac{\partial H}{\partial x} + v\frac{\partial H}{\partial y} + w\frac{\partial H}{\partial z} = 0$$

where a free surface shape is defined as:

$$H(x, y, z, t) = 0.$$

In the present scheme, this kinematic condition is formulated based on the localized level set method which improves the efficiency of the original level set approach [35].

The level set function ϕ is defined as the signed distance from the interface, i.e.,

$$\phi \begin{cases} > 0 & \text{in water,} \\ = 0 & \text{on the interface,} \\ < 0 & \text{in air.} \end{cases}$$

Since $\phi(x, y, z; t) = 0$ defines the free surface shape, the kinematic condition can be satisfied if the following equation is used to update ϕ:

$$\frac{D\phi}{Dt} \equiv \frac{\partial \phi}{\partial t} + u\frac{\partial \phi}{\partial x} + v\frac{\partial \phi}{\partial y} + w\frac{\partial \phi}{\partial z} = 0 \tag{2.45}$$

In the localized version of the level set method, the two parameters γ_1 and γ_2 where $0 < \gamma_1 < \gamma_2$ are introduced. The signed distance function is rewritten as $d(x, y, z; t)$ and the definition of the level set function is modified as:

$$\phi = \begin{cases} \gamma_2 & \text{if } d > \gamma_2, \\ d & \text{if } |d| \leq \gamma_2, \\ -\gamma_2 & \text{if } d < -\gamma_2. \end{cases}$$

Thus, the level set function is localized within the bandwidth $2\gamma_1$ from the interface. The transport Equation (2.45) is also modified as:

$$\frac{\partial \phi}{\partial t} + C(\phi)\left(u\frac{\partial \phi}{\partial x} + v\frac{\partial \phi}{\partial y} + w\frac{\partial \phi}{\partial z}\right) = 0 \tag{2.46}$$

where $C(\phi)$ is the cut - off function defined as [7]:

$$C(\phi) = \begin{cases} 1 & \text{if } |\phi| \leq \gamma_1, \\ \dfrac{(|\phi| - \gamma_2)^2 (2|\phi| + \gamma_2 - 3\gamma_1)}{(\gamma_2 - \gamma_1)^3} & \text{if } \gamma_1 \leq |\phi| \leq \gamma_2, \\ 0 & \text{if } \gamma_2 < |\phi|. \end{cases}$$

is such a way that the update of ϕ is performed only in the region where $|\phi| \leq \gamma_2$.

The numerical solution for Equation (2.46) is identical to the one for the flow (2.8). The cell centered finite volume discretization applied for the cell i yields:

$$V_i \frac{\partial \phi_i}{\partial t} + \sum_j C(\phi_i) \left(\phi_{(i+j)/2} U_{(i+j)/2} \right) = 0 \tag{2.47}$$

where

$$U_{(i+j)/2} \equiv u_i S_{x,(i+j)/2} + v_i S_{y,(i+j)/2} + w_i S_{z,(i+j)/2}$$

V_i is the cell volume and j is the neighbor cells of the cell i. The subscript $(i+j)/2$ means the cell face between the cells i and j and (S_x, S_y, S_z) are the area vectors of the cell faces. $\phi_{(i+j)/2}$ is the value of ϕ on the cell face, is extrapolated from the cell centered values in the second order upwind manner. The gradient of ϕ at the cell center used in the extrapolation above is obtained by the least squares method. The time integration is carried out by the Euler backward scheme.

The discrete Equation (2.47), however, does not necessarily gives $\partial\phi/\partial t = 0$, unless

$$\sum_j \left(\phi_{(i+j)/2} S_{x,(i+j)/2} \right) = 0$$

is satisfied. Since the current function $\phi = -z$ is a linearly varying function, the extrapolation of the face value $\phi_{(i+j)/2}$ from the cell centered values can be performed to give the exact values. The approach taken here to remedy this problem is to introduce a new variable $\tilde{\phi}$ which is defined as $\tilde{\phi} = \phi + z$ and to solve $\tilde{\phi}$ instead of ϕ. Thus, the Equation (2.45) is modified as [7]:

$$\frac{\partial \tilde{\phi}}{\partial t} + C\left(\tilde{\phi}\right) \left(u \frac{\partial \tilde{\phi}}{\partial x} + v \frac{\partial \tilde{\phi}}{\partial y} + w \frac{\partial \tilde{\phi}}{\partial z} - w \right) = 0 \tag{2.48}$$

and in the discrete form as follows:

$$V_i \frac{\partial \tilde{\phi}_i}{\partial t} + \sum_j C(\phi_i) \left(\tilde{\phi}_{(i+j)/2} U_{(i+j)/2} \right) - C(\phi_i) V_i w_i = 0 \tag{2.49}$$

In order to avoid the reflection of free surface waves in the outer boundaries of a computational domain, the wave damping method which has been proved to be effective

in the interface fitting approach is also applied to the level set method. The damping term which makes $\tilde{\phi}$ approach to zero is added to the level set equation (2.49) as follows:

$$V_i \frac{\partial \tilde{\phi}_i}{\partial t} + \sum_j C(\phi_i)\left(\tilde{\phi}_{(i+j)/2} U_{(i+j)/2}\right) - C(\phi_i) V_i w_i + V_i W \tilde{\phi}_i = 0 \tag{2.50}$$

with $W(x, y, z)$ is weight function defined as:

$$\begin{aligned} W(x,y,z) =& A \times \max\left(W_x(x), W_y(y)\right) \\ W_x(x) =& \begin{cases} \left(\dfrac{x - x_d}{x_0 - x_d}\right)^2 & \text{if } x_d \leq x \leq x_0 \\ 0 & \text{otherwise} \end{cases} \\ W_y(y) =& \begin{cases} \left(\dfrac{y - y_d}{y_0 - y_d}\right)^2 & \text{if } y_d \leq y \leq y_0 \\ 0 & \text{otherwise} \end{cases} \end{aligned}$$

where x_d, y_d are the coordinate from which the damping region starts and x_0, y_0 are the location of outflow and side boundaries. The parameter A controls the amount of damping. The added term $V_i W \tilde{\phi}_i$ is proved to effectively make $\tilde{\phi}$ approach to zero in the damping region and thus dissipates outgoing waves.

There is a singular behavior of the interface in the region closed to a solid wall. The no - slip condition imposed on a wall prevents the interface movement there, while the interface in the outer region moves following the fluid motion. It causes the large deformation of ϕ near a solid wall. The extrapolation approach is employed here to remove this singularity, in which the value of ϕ for the cells closed to the wall is extrapolated from the outer cell.

In order to carry out the extrapolation, the distance to the closet wall d_i (where i is the cell index) is computed and stored for each cell first. In the region where extrapolation is needed, ϕ is extrapolated from outside in such a way that it is constant in the direction normal to the wall. Thus, the pseudo convection equation:

$$\frac{\partial \phi}{\partial \tau} - \frac{\nabla d}{|\partial d|} \cdot \nabla \phi = 0 \tag{2.51}$$

is solved in the pseudo time τ in the extrapolation region. Note that the convection velocity $\nabla d / |\nabla d|$ is the unit vector normal to the wall from outside to a wall. It ensures the extrapolation from outside when an upwind scheme is used for the discretization. Upon convergence, ϕ becomes constant in the direction normal to the wall as desired.

2.2.5.1 Re-initialization

The re-initialization of the level set function is an important step in the level set method, since the level set function is no longer a distance function after convection. The re-initialization process can be done using the partial differential equation.
The equation to be solved has form as:

$$\frac{\partial \phi}{\partial \tau} + S\left(\phi_0\right)\left(|\nabla \phi| - 1\right) = 0 \tag{2.52}$$

where ϕ_0 is the initial value and S is the sign function [7]:

$$S\left(\phi\right) = \begin{cases} -1 & \text{if } \phi < 0 \\ 0 & \text{if } \phi = 0 \\ 1 & \text{if } \phi > 0 \end{cases}$$

Upon the convergence, ϕ becomes the distance function again, since $|\nabla \phi| = 1$.
In a numerical process, $S\left(\phi\right)$ is approximated as:

$$S_{\varepsilon}\left(\phi\right) = \frac{\phi}{\sqrt{\phi^2 + \varepsilon^2}}$$

where ε is a typical grid spacing. Then, Equation (2.52) is rewritten as:

$$\frac{\partial \phi}{\partial \tau} + S_{\varepsilon}\left(\phi_0\right) \frac{\nabla \phi}{|\nabla \phi|} \cdot \nabla \phi = S_{\varepsilon}\left(\phi_0\right) \tag{2.53}$$

which can be viewed as the convection equation with the convection velocity being $S_{\varepsilon}\left(\phi_0\right) \nabla \phi / |\nabla \phi|$.

The numerical procedure for Equation (2.53) is similar to the convection Equation (2.49). First, $\nabla \phi$ is computed using the least squares method for each cell center. The convection velocity $S_{\varepsilon(\phi_0)} \nabla \phi / |\nabla \phi|$ is then evaluated. The second term $\nabla \phi$ in Equation(2.53) is discretized by the first order upwind scheme in a finite volume framework. The pseudo time integration is made by the Euler implicit scheme [35].

2.2.5.2 Flow Variable Extrapolation

Since almost hydrodynamics applications require a flows field of water region only, a one-phase flow approach is used, i.e., the flow equations are solved only in a water region. Flow variables in air region are extrapolated from a water region in way so that the dynamics condition on the free surface boundary is satisfied. This method also has an advantage that it is not necessary to cope with the large density difference between air and water. At this point, the present method differs from the original level set method where a two phases flow approach is employed [35].

The dynamics free surface condition can be approximated by the two following conditions. First, the velocity gradients normal to the free surface are zero. Second, the pressure on the free surface is equal to the atmospheric pressure. In order to satisfy the first condition, the velocity components are extrapolated in the direction normal to the interface. Following the localized level set method, it can be achieved by solving the following equation in an air region where $\phi < 0$ for the pseudo time τ.

$$\frac{\partial \vec{q}}{\partial \tau} - \frac{\nabla \phi}{|\nabla \phi|} \cdot \nabla \vec{q} = 0 \tag{2.54}$$

Note that the quantity $-\nabla\phi/|\nabla\phi|$ is the unit vector normal to the interface and whose direction is from water to air. In the region away from the interface where ϕ is constant,

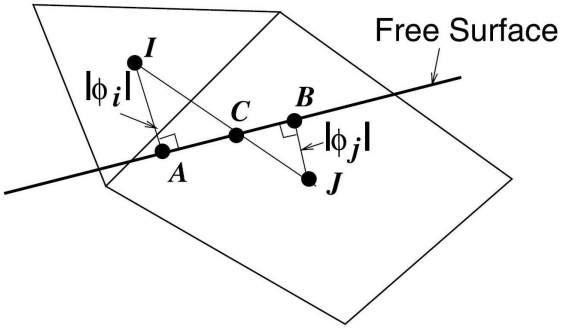

Figure 2.6: Pressure condition on free surface

$-\nabla\phi/|\nabla\phi|$ is replaced by the vector $(0, 0, 1)^T$.

The pressure boundary condition is written as:

$$p = \frac{\zeta}{Fn^2} \qquad \text{on the free surface} \tag{2.55}$$

where atmospheric pressure is assumed to be zero and ζ is the z-coordinate of the interface. For an air cell which is next to a water cell, pressure is extrapolated in the following way. Suppose that the cell i is the air cell for which the pressure must be extrapolated and the cell j is the neighboring water cell as shown in the Figure 2.6. From the definition, $|\phi|$ is the distance to the interface with $\phi_i < 0$ and $\phi_j > 0$. The interface is supposed to be located between the cell centers i and j.

As shown in Figure 2.6, the interface is locally approximated by a flat surface (a straight line in 2D) and the closet point on the interface from the cell center i (point I in Figure 2.6) is denoted as A and the closet point from the cell center j (point I in Figure 2.6) is denoted as B. Also the intersection of the interface and the line connecting the cell

centers i and j is denoted as C. Since the triangle IAC is similar to the triangle JBC and the length $\overline{IA} = |\phi_i|$ and $\overline{JB} = |\phi_j|$. The Z_C, $z-$ coordinate of the point C, is given by:

$$Z_C = \frac{|\phi_i| Z_j + |\phi_j| Z_i}{|\phi_i| + |\phi_j|}.$$

Thus pressure is extrapolated as:

$$p_i = \frac{\left(Z_C / Fn^2\right)\left(|\phi_i + \phi_j|\right) - p_j |\phi_i|}{|\phi_j|}$$

in such a way that:

$$p_C = \frac{Z_C}{Fn^2}$$

Note that this procedure uses only the value of ϕ and the actual free surface shape does not need to be constructed.

In case that an air cell has several adjacent water cell, the pressure values is obtained by taking the average of the extrapolated values from each water cell. In the remaining air region, pressure is extrapolated by using Equation (2.54).

2.3 Hull form modification method

The role of shape modification is to provide a link between the design variables and a hull form which should be defined geometrically. In the optimization system whenever the design variables are determined, the corresponding hull form should be created efficiently. Therefore, the modification method should be flexible enough to cover the wide range of the design variables. Moreover, to enhance the efficiency of the optimization process, number of the design variables should be as small as possible and the hull form modification should be as simple as possible at the same time [11].

As mentioned in the Chapter 1, most of the previous studies on the stern shape optimization have frequently used the user defined modification functions which change the width of the frameline curves to optimize the given hull form [8, 11]. With the constraints assigned on the design variables, variation of the framelines somehow is limited (Figure 2.7(a)). In this study, the hull form modification method is applied for not only the modification of the frameline but also for determination of the transom height at the stern end of a ship hull. Since the transom bottom is not fixed, the hull form modification method is expected to give a greater flexibility (Figure 2.7(b)) and the modified hull form is also expected to have better performance.

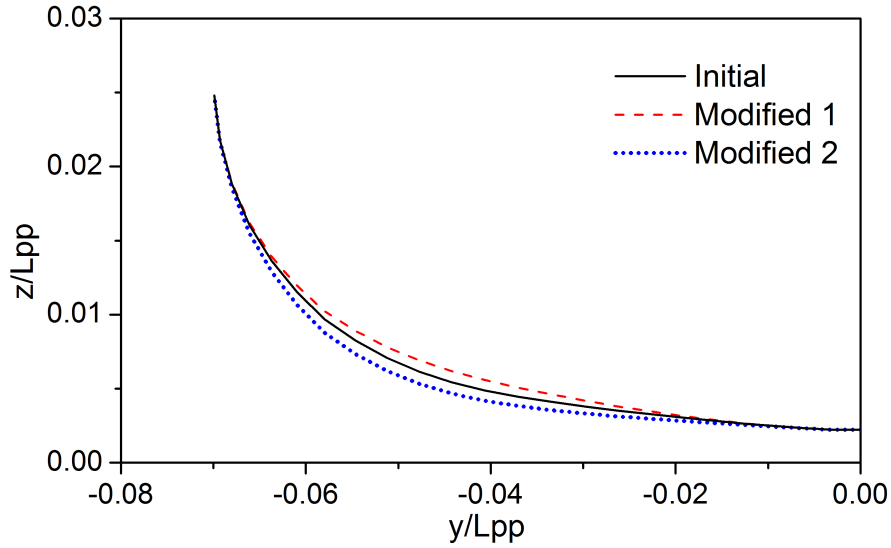

(a) Former modification method

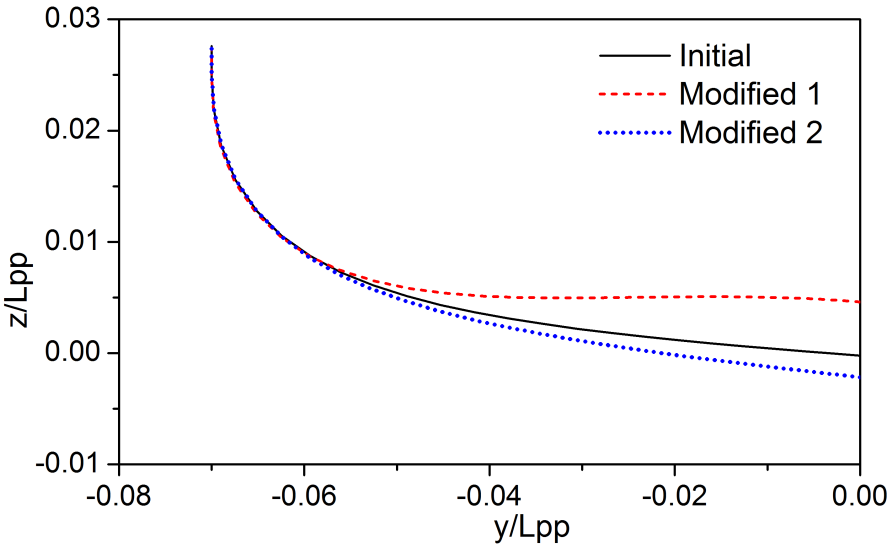

(b) New modification method

Figure 2.7: Comparison of the modification methods.

In this study, the Cartesian coordinate system is used in the grid generation in which x, y, z are the streamwise, lateral and vertical with upward positive directions, respectively. Since only the stern overhang region is concerned, the other parts are kept fixed during the optimization process. Two design variables named x_{st} and d_z are used to define a new stern shape in which x_{st} is the x-coordinate of the starting point of the modified region and d_z is the vertical displacement of the bottom profile at the stern end with positive upward direction (Figure 2.8(a)). Since x_{st} and d_z are used to define the transom stern only, the constraints upon x_{st} and d_z should be assigned to make sure that the main hull form is preserved throughout the optimization process.

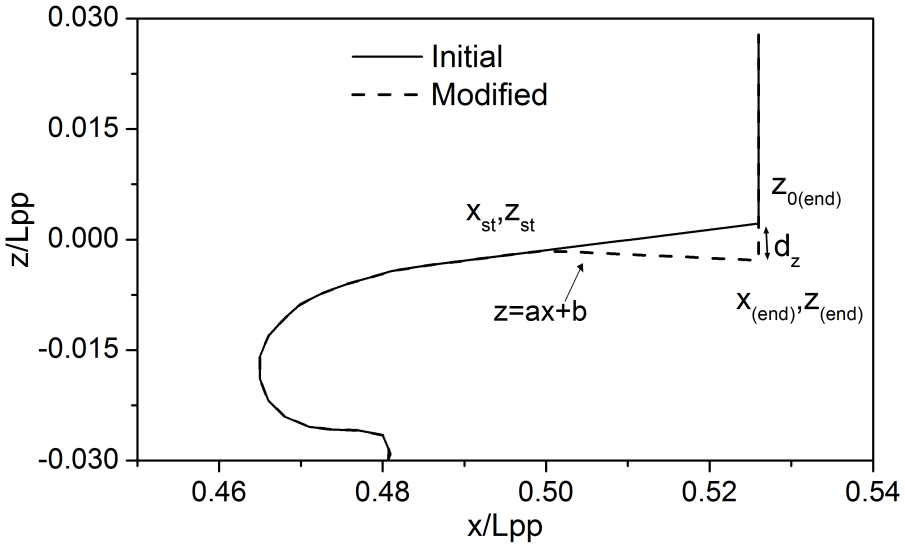

(a) The modification of bottom profile

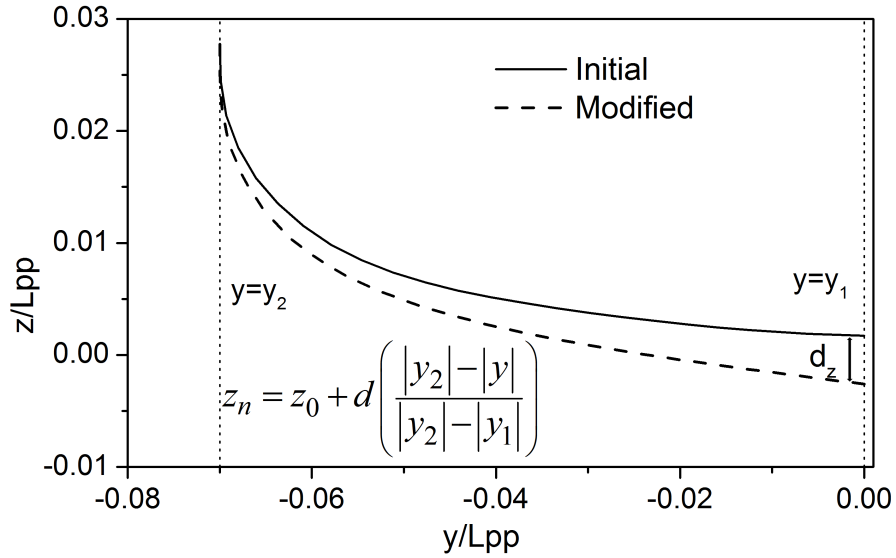

(b) The modification of frameline

Figure 2.8: The hull form modification method.

When the design variables are given, new transom shape is redefined as follows:

Firstly, the straight line connecting the upstream point (x_{st}, z_{st}) to the ending point (x_{end}, z_{end}) of ship hull is determined by using the following equation (Figure 2.8(a)):

$$z = ax + b \tag{2.56}$$

in which a and b are determined by simply solving the system of linear equations as follows:

$$\begin{cases} z_{st} & = ax_{st} + b \\ z_{end} & = ax_{end} + b \end{cases} \tag{2.57}$$

where (x_{end}, z_{end}) are the coordinates of centreline profile at the stern end. z_{st} is the z-coordinate of the starting point in the symmetry plane where $x = x_{st}$. Since d_z is the vertical translation of the centerline profile at the stern end, z_{end} is calculated as follows:

$$z_{end} = z_{0(end)} + d_z \tag{2.58}$$

with $z_{0(end)}$ being the z-coordinate of the original bottom profile at the stern end.

New z-coordinate of the grid points along the modified bottom profile can be computed simply by substituting its x-coordinate into Equation (2.57). The vertical translation d of each grid point on the bottom profile from its initial is evaluated as:

$$d = z_n - z_0 \tag{2.59}$$

Following the changes of the bottom profile, the overhang surface of the modified hull form is also regenerated to keep the smoothness of hull surface. Framelines of the modified hull form are redefined by using the vertical displacement d determined in Equation (2.59) as follows (Figure 2.8(b)):

$$z_n = z_0 + d\left(\frac{|y_2| - |y|}{|y_2| - |y_1|}\right) \tag{2.60}$$

where z_0, z_n are the original and new z-coordinates of grid points on the framelines. y_1, y_2 are the lower and upper bounds of frameline used in the modification process. Since only a half of hull form in the port side with $y_1 = 0$ being the symmetry plane used in the grid generation, the Equation (2.60) can be rewritten as:

$$z_n = z_0 + d\left(1 - \frac{|y|}{|y\text{max}|}\right) \tag{2.61}$$

where y_{max} is the y-coordinate of the ship breadth at each modified station.

In this study, effects of the frameline modification functions to the final optimized results are also included in the examination. For this purpose, the linear form of the modification function in Equation (2.61) is replaced by a sine form as follows:

$$z_n = z_0 + d \times \text{sine}\left[\frac{\pi}{2}\left(1 - \frac{|y|}{|y\text{max}|}\right)\right] \tag{2.62}$$

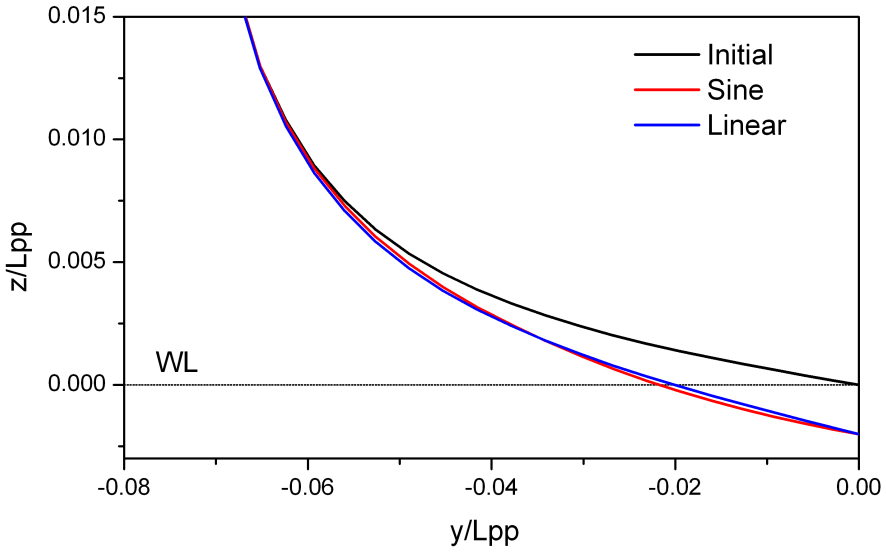

Figure 2.9: Comparison of framelines by using different modification functions.

The modified framelines by using the linear and sine functions are compared in Figure 2.9. Obviously, the differences of the modified framelines are very small, i.e., curve breadth of the framelines modified by the sine function is wider a little compared to that of the linear form under the still water level. However, it is narrower on the air region.

It is important to note that, in the optimization process whenever a hull form is redefined following the changes of the design variables, the computational grid around the modified ship hull itself should be regenerated to get accurate CFD analysis. In this study, the coordinates of grid points X along the grid lines in the direction from the hull surface to outer boundary are modified as follows:

$$X_k^{\text{new}} = X_k^{\text{old}} + w_k \left(X_1^{\text{new}} - X_1^{\text{old}} \right) \tag{2.63}$$

Chapter 3

Application

3.1 The initial hull form and computational conditions

In order to demonstrate the applicability of the present method, transom stern of a container ship is optimized for minimizing the pressure resistance coefficient. The initial hull form is based on the original KRISO Container Ship (KCS) ship hull [36] with a slight modification in such a way that transom bottom of the modified one is on the still water level at rest as depicted in Figures 3.1 and 3.2. Following the changes of the bottom profile, framelines in the overhang domain of the modified hull form are also redefined as shown in Figure 3.2(b). The principal particulars of the original KCS and of the modified hull form are compared in Table 3.1. The modified hull form is selected as the initial hull form of the optimization processes because the original KCS is a practical ship hull based on a professional design and therefore its hull form has been already optimized by some ways.

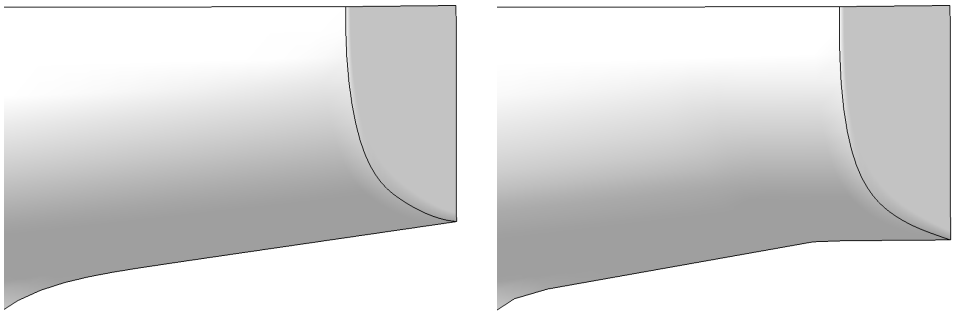

(a) Initial KCS. (b) Modified ship hull.

Figure 3.1: Overhangs of the initial KCS and modified ship hull.

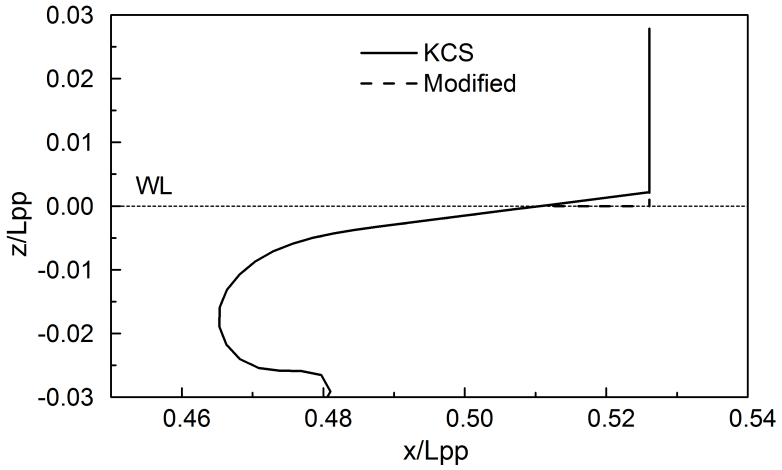

(a) Centerline profiles.

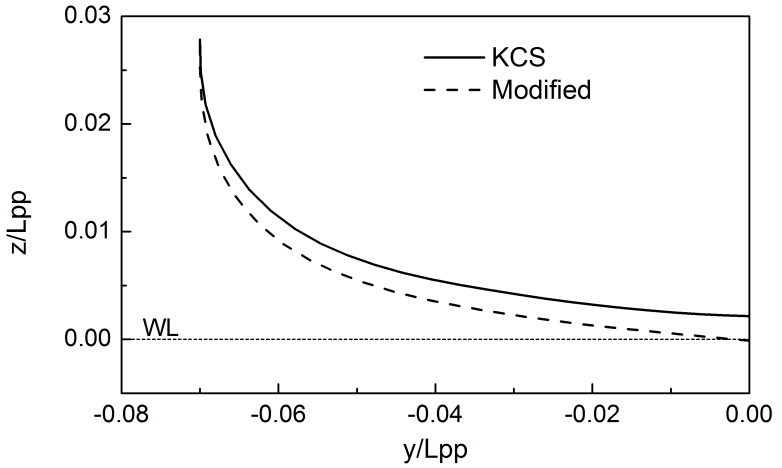

(b) Frame lines at the stern end plane.

Figure 3.2: Bottom profiles and frame lines at the stern plane of the KCS and modified hull forms.

Table 3.1: Principal paticulars.

Principal particulars	Full scale	
	KCS	Modified ship hull
Length L(m)	230.0	230.0
Breath B(m)	32.2	32.2
Depth D(m)	19.0	19.0
Draft T(m)	10.8	10.8
Block coefficient C_b	0.65	0.65
S/L× L	1.785×10^{-1}	1.788×10^{-1}

As shown in Table 3.1, most of the principal particulars of the modified hull form are the same as those of the original KCS hull. There is only the wetted surface area of the modified hull larger a little compared to that of the KCS hull form.

It is also important to note that the CPU time for solving a hull form optimization problem is mostly spent for solving a flow field around a ship hull to evaluate the objective functions, therefore in order to get the optimized results quickly, the CPU time needed for one CFD computation should be as short as possible, which means that size of the computational grid should be small. In this study, the computational grid is generated based on the structured grid of an O-O type in which the grid numbers in the longitudinal, girth and outward directions are $121 \times 25 \times 41$, respectively (Figure 3.3). The corresponding CPU time for one CFD computation by using a computer with 8 CPU I7-3770 and 8GB of RAM is approximately 0.9 hours. The solution domain is set as $-1.5 \leq x/L_{pp} \leq 2.5, -1.5 \leq y/L_{pp} \leq 0, -1.472 \leq z/L_{pp} \leq 0.028$ in which ship hull is located at $-0.53 \leq x/L_{pp} \leq 0.526$. Reynolds number is set $Rn = 1.4 \times 10^7$ and Froude number $Fn = 0.26$ which corresponds to a model scale of a ship model having length L = 7.2 [m]. Flow field around ship hull is computed in the free trim condition.

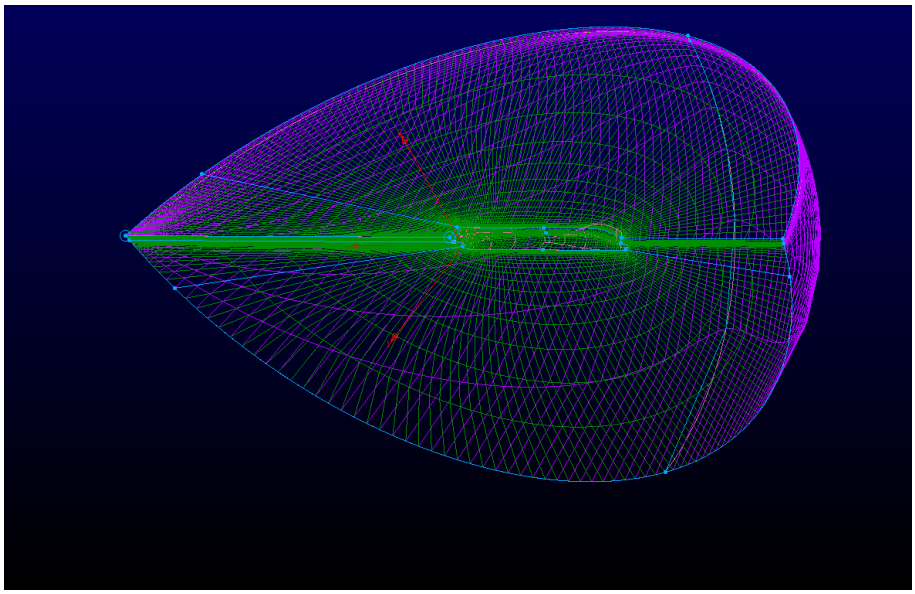

Figure 3.3: Computational grid.

3.2 Optimized results and Discussions

3.2.1 Verification and Validation for CFD solver

Verification and validation are important for CFD solver, especially in hull form optimization problem. If the computational grid and the CFD solver are good enough and reliable, the optimized results are significantly meaningful. Therefore, in this study, the author has verified the SURF solver for the case of KCS hull form first. The computed results of wave profile and simulated wave pattern around ship hull are compared to those of experimental data are shown in Figure 3.4 and Figure 3.5, respectively.

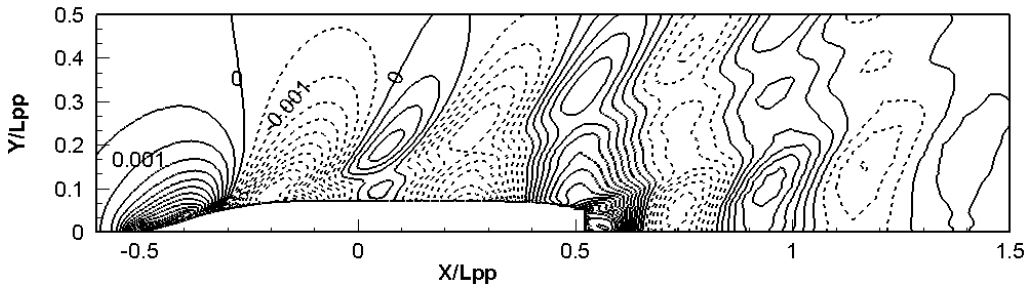

(a) computed

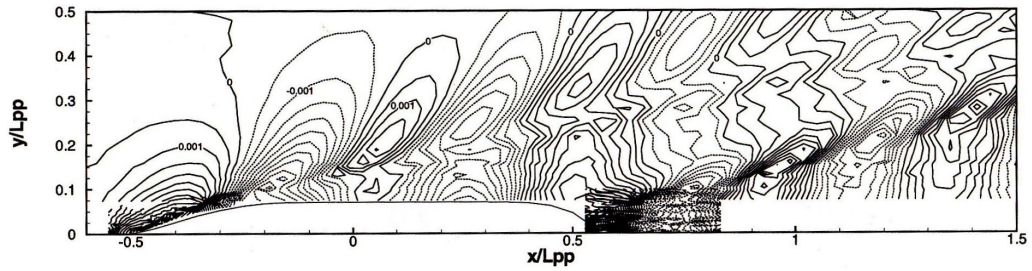

(b) measured

Figure 3.4: Computational grids around transom stern of KCS Container Ship used in V&V procedure .

Obviously, as shown in Figures 3.4 and 3.5, the computed wave pattern and wave profile are reproduced reasonably well in comparison with measured data, although the waves are dissipated in the region far from ship hull where grid resolution is not fine enough. The simulated results of wave pattern behind the stern end (Figure 3.4) are not really good in comparison with experimental data because prediction of wave patterns in the transom region is known as one of the most difficult problems in the computational fluid dynamics. On the other hand, getting the accurate flows field at stern by experiment is also very difficult since the stern region is acknowledged to be much influenced by turbulent effects. However, the good agreement of results in other sections indicates that

the SURF solver has a robust and accurate solution scheme for this kind of problems.

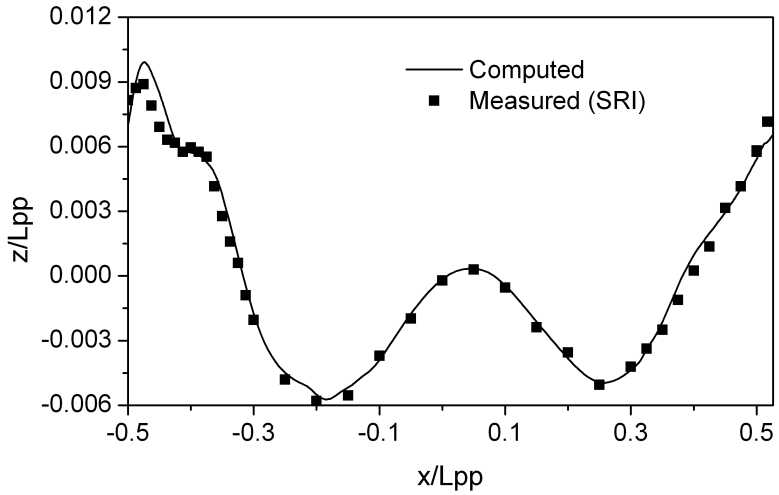

Figure 3.5: Comparison of the computed and measured wave profile along the KCS hull form.

Verification and validation of the computed hydrodynamic resistance are performed following the recommended procedures of ITTC 7.5-03-02-01 [37] and ITTC 7.5-03-01-01 [38]. The simulation error δ_S is defined as the difference between a simulation results S and the truth T and is composed of additive modeling δ_{SM} and numerical δ_{SN} error. For certain conditions, both the sign and magnitude of the numerical error can be estimated as $\delta_{SN} = \delta^*_{SN} + \varepsilon_{SN}$ where δ^*_{SN} is an estimate of the sign and magnitude of δ_{SN}; and ε_{SN} is the error in that estimate. The simulation value is corrected to provide a numerical benchmark S_C, which is defined as [37, 38]:

$$S_C = S - \delta^*_{SN}$$

For the uncorrected simulation approach, numerical error is decomposed into contributions from iteration number δ_I, grid size δ_G, time step δ_T and other parameters δ_P, which gives the following expression for simulation numerical uncertainty:

$$U^2_{SN} = U^2_I + U^2_G + U^2_T + U^2_P$$

For the corrected simulation approach, the solution is corrected to produce a numerical benchmark S_C and the estimated simulation numerical error δ^*_{SN} and corrected uncertainty U_{S_cN} are given by:

$$\delta^*_{SN} = \delta^*_I + \delta^*_G + \delta^*_T + \delta^*_P$$

$$U_{S_cN}^2 = U_{I_c}^2 + U_{G_c}^2 + U_{T_c}^2 + U_{P_c}^2$$

Iterative and parameter convergence studies are conducted using multiple solutions with systematic parameter refinement by varying the i^{th} input parameter Δx_i while holding all other parameters constant. Convergence study requires a minimum of $m = 3$ solution to evaluate convergence with respect to input parameter. Change between medium - fine $\varepsilon_{i,21} = \hat{S}_{i,2} - \hat{S}_{i,1}$ and coarse - medium $\varepsilon_{i,32} = \hat{S}_{i,3} - \hat{S}_{i,2}$ solution are used to define the convergence ratio:

$$R_i = \frac{\varepsilon_{i,32}}{\varepsilon_{i,21}}$$

where $\hat{S}_{i,3}, \hat{S}_{i,2}$, and$\hat{S}_{i,1}$ are solutions of coarse, medium and coarse grid. Depending on the value of R_i, 3 convergence conditions are possible:

(i) Monotonic convergence: $0 < R_i < 1$

(ii) Oscillatory convergence: $R_i < 0$

(iii) Divergence: $R_i > 1$

For the condition (i), generalized Richardson extrapolation (RE) is used to estimate U_i or δ_i^* and U_{i_C}. For condition (ii), uncertainties are estimated simply by attempting to bound the error based on oscillation maximums S_U and minimum S_L, i.e.,

$$U_i = \frac{1}{2}(S_U - S_L)$$

For oscillatory convergence (ii), the solution exhibit oscillations, which may be erroneously identified as condition (i) or (iii). This is apparent if one considers evaluating convergence condition from 3 points on a sinusoidal curve. Depending on where the three points fall on the curve, the condition could be incorrectly diagnosed as either monotonic convergence or divergence. Bounding the error based on oscillation maximum and minimum for condition (ii) requires more than m=3 solutions. For condition (iii), errors and uncertainties can not be estimated.

In condition (i), solution convergence occurs and generalized Richardson extrapolation is used to estimate for error and order of accuracy:

$$\delta_{RE_{i,1}}^{*(1)} = \frac{\varepsilon_{i,21}}{r_i^{p_i} - 1}$$

$$p_i = \frac{\ln(\varepsilon_{i,32}/\varepsilon_{i,21})}{\ln(r_i)}$$

where $r_i = \triangle x_{i2}/\triangle x_{i1} = \triangle x_{i3}/\triangle x_{i2}$ is the refinement factor which defines the relation between the considered grid. When $\delta^{*(1)}_{RE_{i,1}}$ and p_i is determined, it is possible to estimate the grid uncertainty. There are 2 ways to do this depending on whether the solutions are closed to the asymptotic range or not. If the correction factor defined by:

$$C_G = \frac{r_G^{P_G} - 1}{r_G^{P_{Gest}} - 1}$$

where $P_{G_{est}}$ is the limiting or theoretical accuracy of the applied numerical method, is closed to unity, the solution are closed to the asymptotic range. The numerical error, δ^*_{SN}, benchmark S_C and uncertainty U_{GC} can be calculated from [**?**]:

$$\delta^*_{SN} = C_G \delta^{*(1)}_{RE_{i,1}}$$

$$S_C = S - \delta^*_{SN}$$

$$U_{G_C} = |1 - C_G| \left|\delta^*_{SN}\right|$$

If the correction factor is away from unity only the numerical uncertainty is calculated:

$$U_G = (2|1 - C_G| + 1) \left|\delta^*_{SN}\right|$$

Validation is defined as a process for assessing simulation modeling uncertainty U_{SM} by using benchmark experimental data and when conditions permit, estimating the sign and magnitude of the modeling error δ_{SM} itself. The comparison error E is given by the difference in the data D and simulation S values [37, 38]:

$$E = D - S = \delta_D - (\delta_{SM} + \delta_{SN})$$

Modeling errors δ_{SM} can be decomposed into modeling assumptions and use of previous data. To determine if validation has been achieved, E is compared to the validation uncertainty U_V given by:

$$U_V^2 = U_D^2 + U_{SN}^2$$

If $|E| < U_V$, the combination of all errors in D and S is smaller than U_V and validation is achieved at the U_V level. If $U_V \ll |E|$, the sign and magnitude of $E \approx \delta_{SM}$ can be used to make modeling improvements. For the corrected simulation, equations equivalent to (3.2.1), (3.2.1) are:

$$E = D - S_C = \delta_D - (\delta_{SM} + \varepsilon_{SN})$$

$$U^2_{V_c} = U^2_{E_c} - U^2_{SM} = U_D^2 + U_{SN}^2$$

In the present study, three systematically refined grids (*coarse, medium* and *fine*) with refinement ratio of $\sqrt{2}$ are used to estimate the grid uncertainty (Figure 3.6). The computed resistance coefficients and number of grid cells for each grid are presented in Table 3.2. The resistance coefficients are defined based on the length between perpendiculars, i.e., total resistance coefficient $C_t = R_t/0.5\rho U^2 L_{pp}^2$, frictional resistance coefficient $C_f = R_f/0.5\rho U^2 L_{pp}^2$ and pressure resistance coefficient $C_p = R_p/0.5\rho U^2 L_{pp}^2$ in which R_t, R_f and R_p are the total resistance, frictional resistance and pressure resistance, respectively. An error (ε) is the difference of the computed results of the coarse and medium grids compared to that of the fine grid.

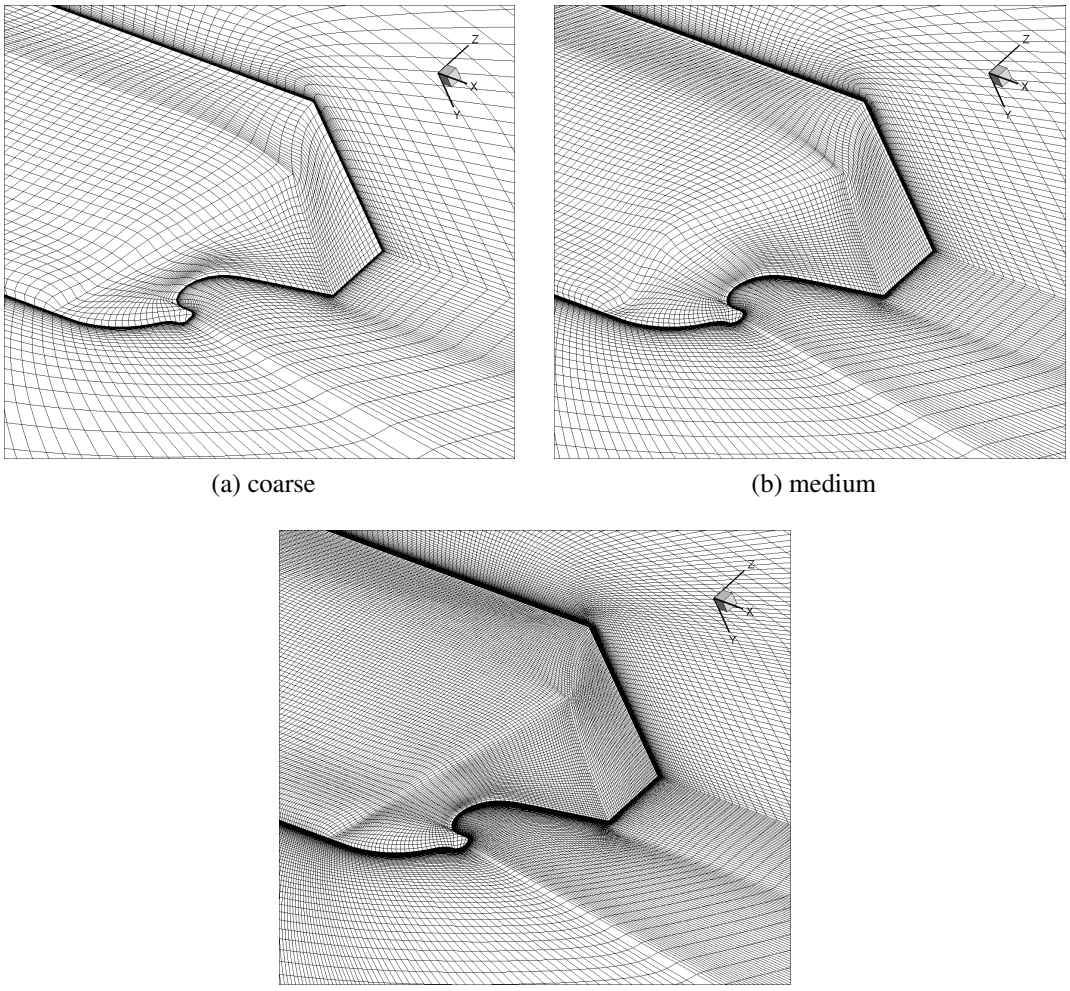

(a) coarse

(b) medium

(c) fine

Figure 3.6: Computational grids around transom stern of KCS Container Ship used in V&V procedure .

Table 3.2: Grid convergence study of resistance coefficients of the KCS model

	Coarse (S_3)	Medium (S_2)	Fine (S_1)	Data (D)
No. cells	491520	1383120	3932160	-
C_t	6.92×10^{-4}	6.63×10^{-4}	6.46×10^{-4}	6.38×10^{-4}
$\varepsilon(C_t)$	7.12%	2.63%	-	-

% is referred to S_1

Table 3.3: Verified results of the resistance coefficients

	R_G	P_G	C_G	U_G	δ_G^*	U_{G_C}	S_C
C_p	1.04						
C_f	-1.33			0.77%			
C_t	0.59	1.54	0.71	5.92%	2.63%	1.10%	6.29×10^{-4}

% is referred to S_1

A grid convergence ratio (R_G) of each resistance component can be estimated easily based on the computed resistance coefficients as listed in Table 3.3. For the pressure resistance, with $R_G = 1.04$ which shows the divergence, the grid uncertainty then cannot be estimated. The grid uncertainty in case of the frictional resistance is estimated by simply averaging of the upper (S_2) and lower (S_1) bounds since the grid convergence ratio $R_G = -1.33$. The Richardson extrapolation is used in the estimation of grid uncertainty of the total resistance which has convergence ratio $R_G = 0.59$.

In order to validate the computed total resistance, the comparison error and validation uncertainty need to estimate. The comparison error of the total resistance coefficient is calculated as follows:

$$E = D - S = -1.21\%D$$

And the validation uncertainty is calculated by using the following equation:

$$U_V = \sqrt{U_{SN}^2 + U_D^2} = 6.08\%D$$

where $U_{SN} = U_G = 6\%D$ and $U_D = 1\%D$ [39]. Since $|E| < U_V$ it can be said that the validation has been achieved in this computational scheme for the total resistance with the uncertainty of $6.08\%D$.

3.2.2 Optimized results of the optimization process with $x_{st} = 0.51$.

In this section, results of the optimization process based on the linear modification function with the initial values of $x_{st} = 0.51$, $d_z = 0.0$ are presented. The constraints assigned for the design variables x_{st} and d_z to restrict the modified domain are $0.49 \leq x_{st} \leq 0.52$ and $-0.01 \leq d_z \leq 0.01$, respectively. Histories of the objective function (pressure resistance coefficient that is defined as $C_p = R_p/0.5\rho U^2 L_{pp}^2$) and of the evaluated values of the design variables at each iteration step are shown in Figures 3.7 and 3.8, respectively.

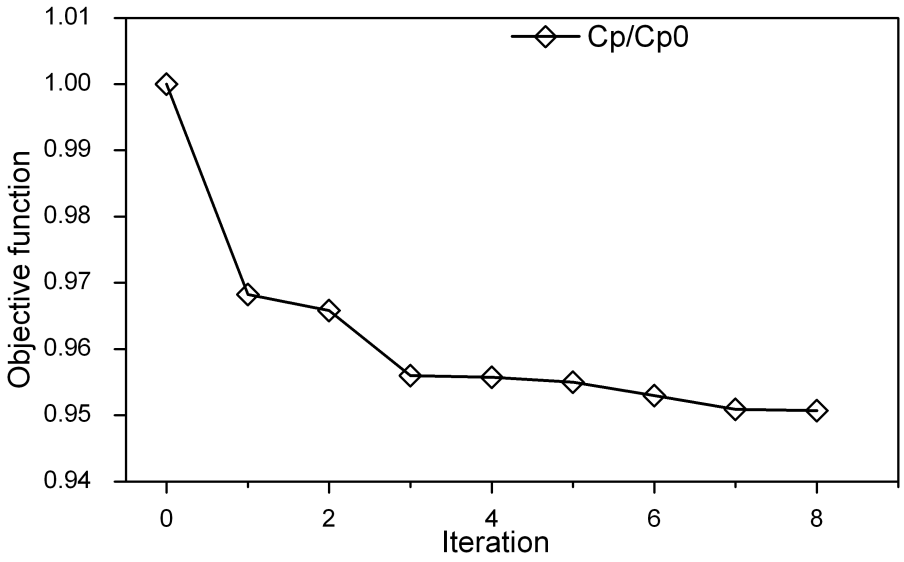

Figure 3.7: History of the objective function of the optimization process with $x_{st} = 0.51$

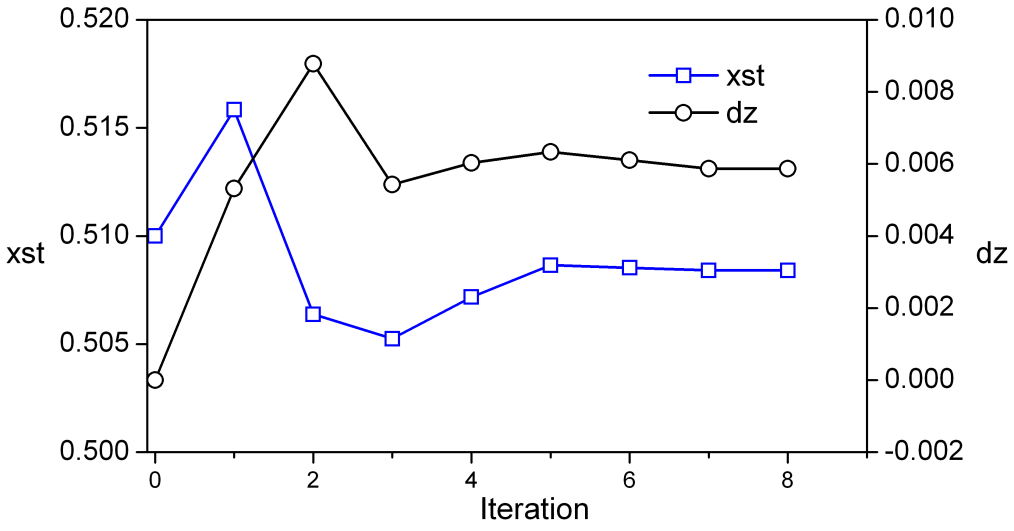

Figure 3.8: Design values of the design variables in the optimization process using $x_{st} = 0.51$

As shown in Figure 3.8, the evaluated values of the design variables of the last two iteration steps are almost the same and the optimization process stops after 8 iterations when the change in successive values of the design variables became too small ($< 1.0 \times 10^{-6}$). The final optimized results, thus, can be considered as the optimized solution and the reduction of pressure resistance coefficient is approximately 5% as shown in Figure 3.7.

Table 3.4: Resistance coefficients of the initial and optimized ship hulls with $x_{st} = 0.51$.

Coef.	Total resistance $C_t = \frac{R_t}{0.5\rho U^2 L_{pp}^2}$	Frictional resistance $C_f = \frac{R_f}{0.5\rho U^2 L_{pp}^2}$	Pressure resistance $C_p = \frac{R_p}{0.5\rho U^2 L_{pp}^2}$
Initial	8.19×10^{-4}	5.14×10^{-4}	3.05×10^{-4}
Optimized	8.03×10^{-4}	5.14×10^{-4}	2.90×10^{-4}

The computed hydrodynamic resistance coefficients of the initial and optimized hull forms by using $x_{st} = 0.51$ are presented in Table 3.4. Obviously, the pressure resistance coefficient shows significantly reduction from that of the initial one. On the contrary to the pressure resistance coefficient, the frictional resistance coefficients of ship hulls do not so big difference. Based on the reduction of pressure resistance coefficient, the total resistance coefficient of the optimized hull form reduces approximately 1.88% from that of the initial ship hull.

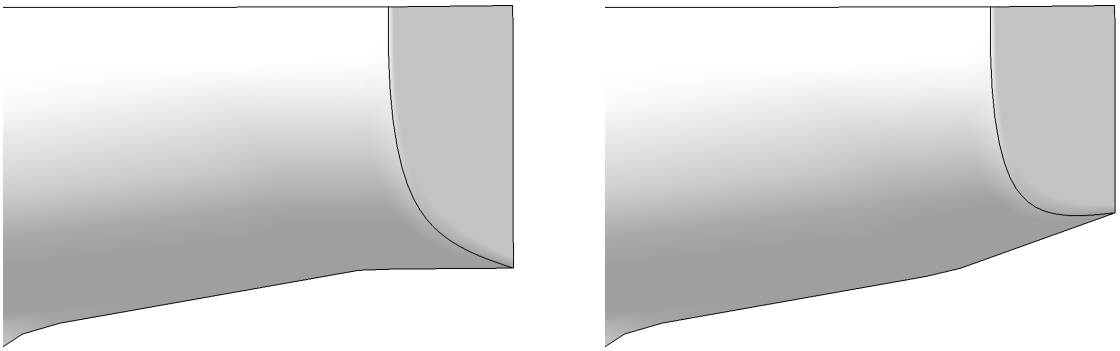

(a) Initial (b) Optimized

Figure 3.9: Overhangs of the initial and optimized hull forms.

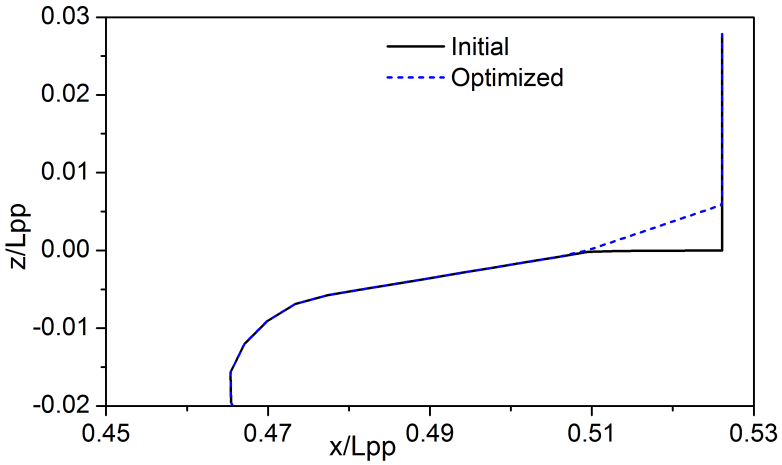

(a) Centerline profiles

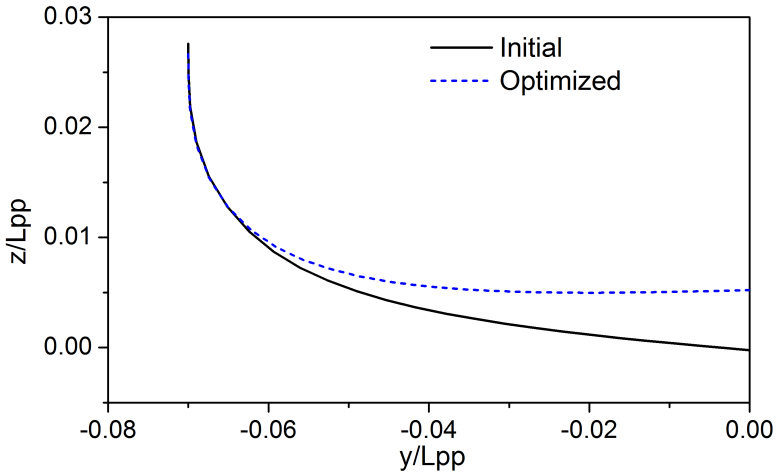

(b) Framelines

Figure 3.10: Centerline profiles and framelines of the initial and optimized hull forms with $x_{st} = 0.51$

Overhang shapes of the initial and optimized hull forms are compared in Figure 3.9. Centerline profiles and framelines at the stern end plane ($x/L_{pp} = 0.526$) of the initial and optimized ship hulls are compared in Figure 3.10. As shown in Figure 3.10(a), centerline profile of the optimized ship hull rises up from the still water level making the flat transom of the initial hull form change to a convex shape. Following the increase of transom height, framelines of the optimized hull form also rise up and become horizontal near the bottom as depicted in Figure 3.10(b).

The computed results of trim (t), sinkage (s) and dipping at the fore (d_f) and aft perpendiculars (d_a) of the initial and optimized ship hulls are listed in Table 3.5. Though the computed sinkages of both initial and optimized hull do not show big differences, the running trims of ship hulls change considerably between each other. The running trim of

Table 3.5: The computed trim, sinkage and dipping of the fore and aft perpendiculars of the initial and optimized hull forms with $x_{st} = 0.51$.

Coef.	Sinkage $s = \frac{d_a + d_f}{2L_{pp}}$	Trim $t = \frac{d_a - d_f}{L_{pp}}$	$\frac{d_f}{L_{pp}}$	$\frac{d_a}{L_{pp}}$
Initial	1.91×10^{-3}	-3.17×10^{-3}	3.41×10^{-3}	0.33×10^{-3}
Optimized	1.96×10^{-3}	-2.62×10^{-3}	3.27×10^{-3}	0.65×10^{-3}

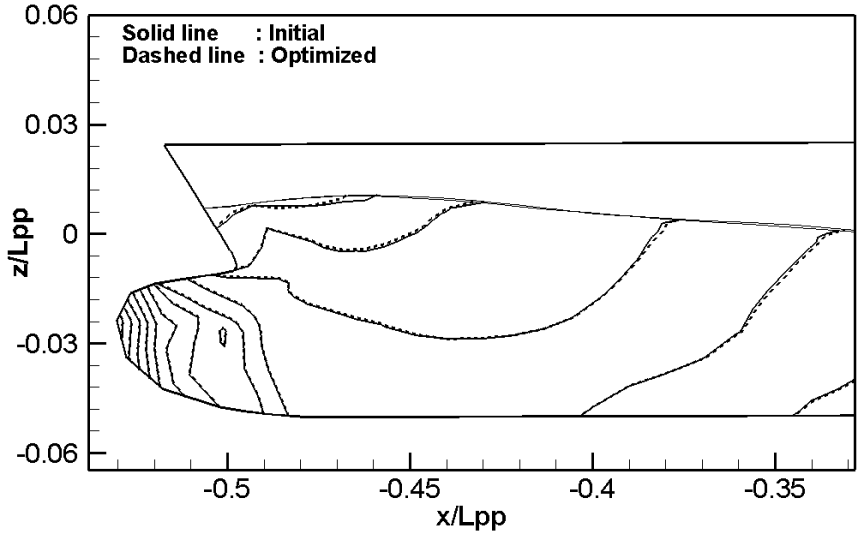

Figure 3.11: Pressure patterns on the hull surface of the fore parts.

the optimized hull form is smaller than that of the initial one. It is due to the fact that the optimized hull decreases dipping of the fore perpendiculars and also increases the immersion of the aft perpendiculars from that of the initial hull form making running trim of the optimized hull form smaller than that of the initial one. The change of running trim makes the pressure pattern on the optimized hull surface of the fore part slightly different from that of the initial one despite both main hull forms are identical as depicted Figure 3.11 (since the modification is applied for the ship stern only).

The distributions of pressure on the initial and optimized overhang surfaces with the views by side and behind the ship stern are compared in Figures 3.12 and 3.13, respectively. Obviously, the flat overhang caused by the reduction of transom height at the stern end makes flows under the initial transom bottom slightly change its directions following the hull geometry. Pressure caused by the change of flow directions increases a little at the inflecting point and decreases at the aft end. On the contrary, the upward shape makes flows under the optimized transom bottom can rise up when ship runs, whereupon pres-

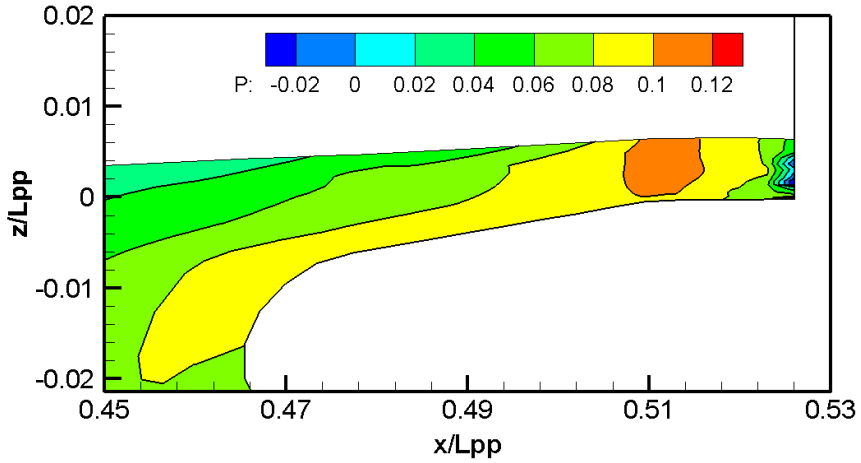

(a) Initial

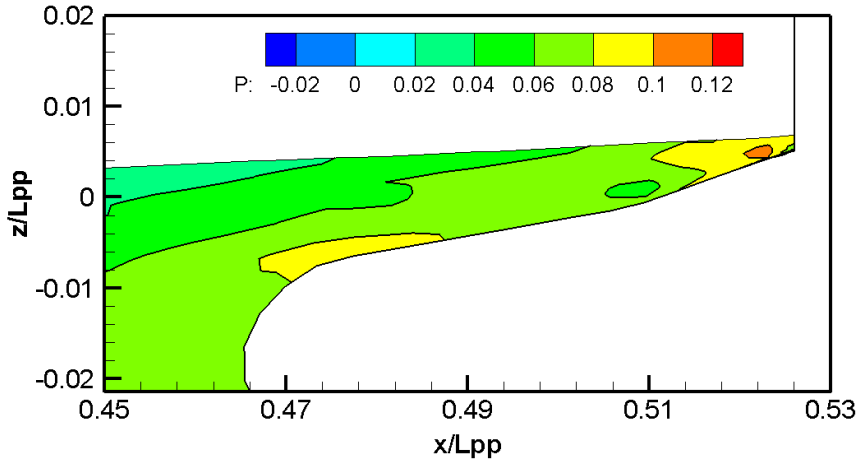

(b) Optimized

Figure 3.12: Pressure distributions on the overhang surfaces

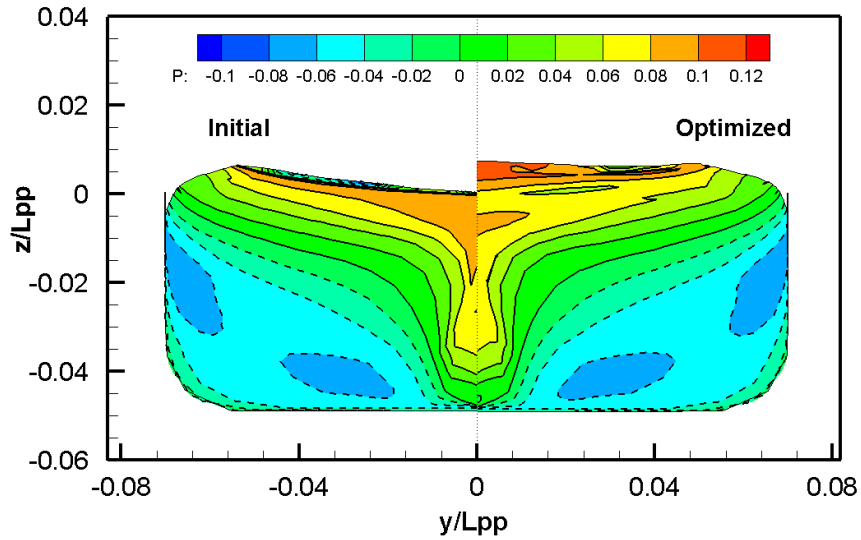

Figure 3.13: Pressure patterns on the hull surface of the aft parts (backview).

sure acting on the optimized overhang surface decrease. Pressure increases slightly again at the aft end only. Furthermore, the change of stern shape effects to the pressure distributions not only in the modified transom but also in the other regions of the optimized hull form. As shown in Figure 3.13, though the pressure patterns in the skeg region of ship hulls are the same, pressure on the hull surface ahead of the optimized domain is slightly different from that of the initial one.

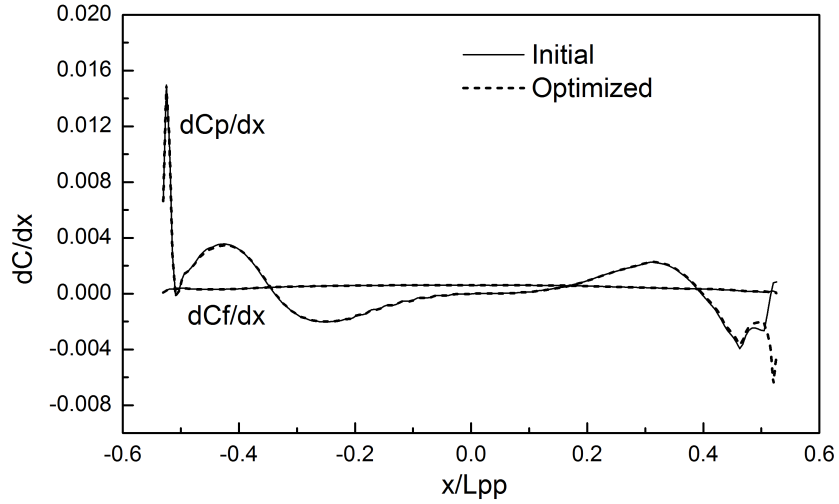

Figure 3.14: The longitudinal distributions of pressure and frictional components of resistance.

The longitudinal distributions of pressure and frictional component of resistance are compared in Figure 3.14. Note that the pressure evaluated here is based on the original pressure, i.e., C_p is integrated without the hydrostatic component by using the following formula $C_p = \int_{\text{girth}} C_p n_x ds$ in which C_p is the original pressure and n_x is the normal vector of the area unit ds. Since reduction of the frictional resistance coefficient is small, differences of the frictional resistance cannot be seen by this plot. Pressure resistance of the optimized hull decreases mostly in the aft part before increases little again at the aft end. Reduction of the pressure resistance in the aft part is consistent with decrease of the pressure resistance of the optimized overhang surface as shown in Figures 3.12 and 3.13.

Wave patterns around the transom sterns and wave profiles behind the stern end of the initial and optimized ship hulls are compared in Figures 3.15 and 3.16, respectively. Obviously, the wave pattern around the optimized hull changes considerably from that of the initial one, i.e., the hollow which appears just behind the stern end of initial hull form is not created in case of the optimized one; instead of that, the crest of stern wave moves toward and closes to the stern end. The movement toward to the stern end of

the wave peak there is due to the changes of overhang shape and state at rest of the transom bottoms. It is important to note that while the initial transom bottom is on the still water level, the optimized one is in the air. Therefore, there is a space between the still water level and transom bottom of the optimized hull form. The free surface flow under the optimized transom bottom, thus, can rise up when ship runs. On the other hand, overhang of the optimized hull form is also smaller than that of the initial one due to the increase of transom height and decrease of frameline's width (Figure 3.10). Elevation of the stern waves near the optimized overhang becomes higher than that of the initial one. As shown in Figure 3.16, the wave profile behind the optimized stern end is higher making its transom wet. While, the hollow behind the stern end of the initial ship hull makes its wave profile lower. The initial transom, thus, is mostly dry.

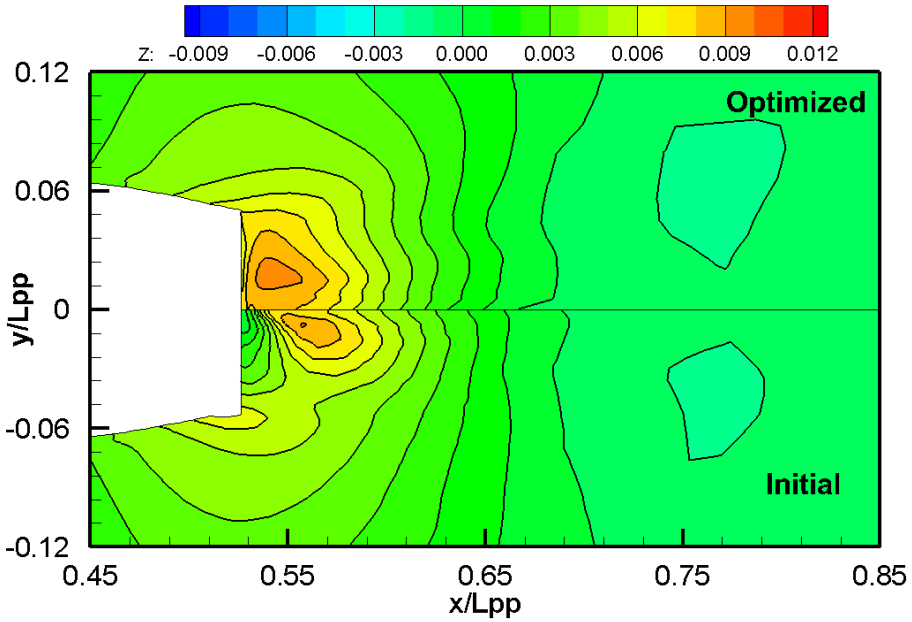

Figure 3.15: Wave patterns around transom sterns.

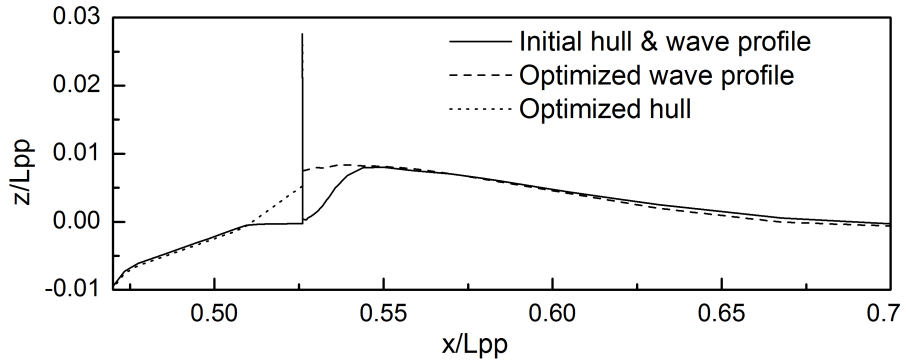

Figure 3.16: Wave profiles behind the stern end of ship hulls .

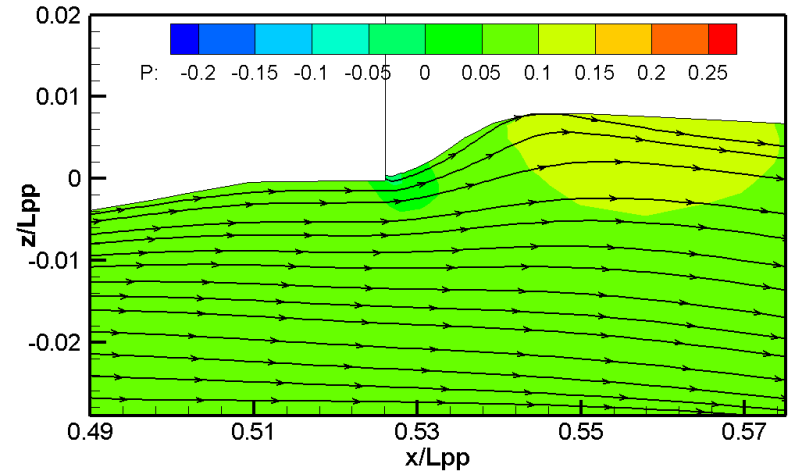

(a) Initial

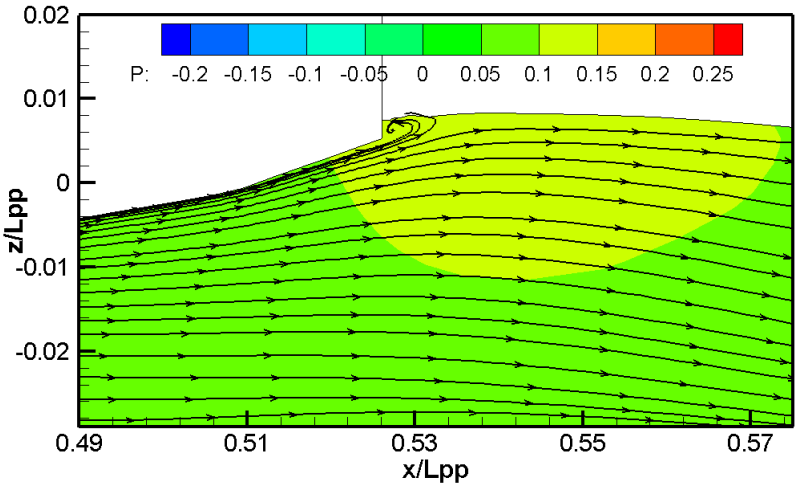

(b) Optimized

Figure 3.17: Streamlines in the center plane of ship hulls.

Figure 3.17 illustrates the simulated streamlines in the symmetry plane of ship hulls. As shown in Figure 3.17(a), the rising up flows under the initial transom bottom change its direction slightly following the hull form geometry. Streamlines near bottom surface become horizontal before rise up behind the stern end. On the contrary, streamlines under transom bottom of the optimized one rise up since its transom bottom is above the still water level. Flows close to the hull form are separated behind the stern end and create a small vortex there. It can be also concluded that the higher wave profile and the wetted transom in case of the optimized hull form are caused by inflection of the ship flows from the wave crest behind the stern end (Figure 3.17(b)).

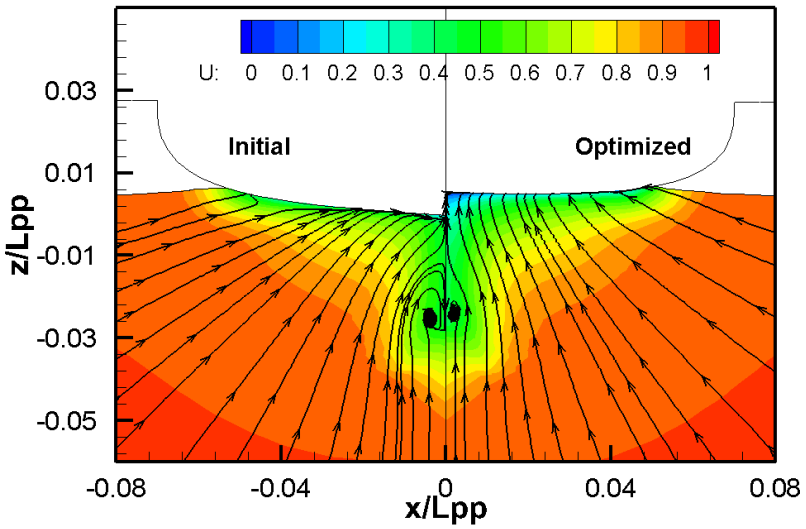

(a) Initial

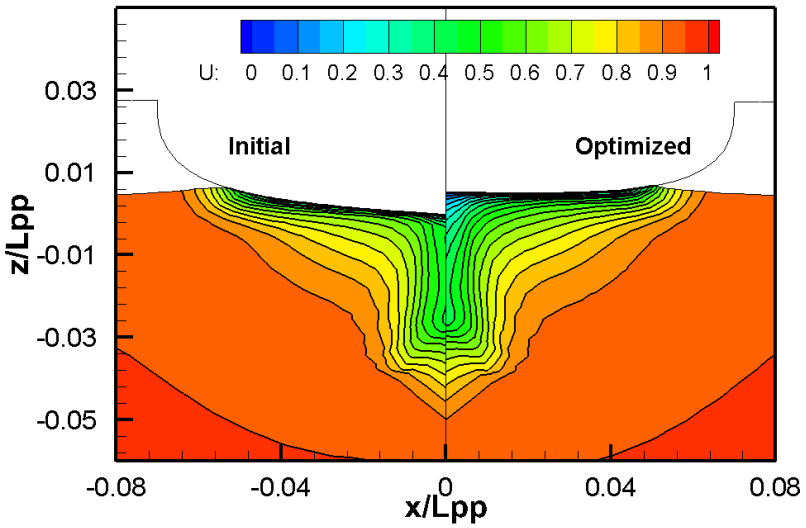

(b) Optimized

Figure 3.18: Streamlines at the stern end plane and wakes.

Figure 3.18 compares streamlines and the axial distributions of velocity at the stern end plane of ship hulls. In consistence with the simulated streamlines in the symmetry plane as depicted in Figure 3.17, streamlines under the initial transom bottom almost go horizontal near hull surface, while streamlines under the optimized hull form rise up mostly. The vortex under the optimized ship hull is also smaller (Figure 3.18(a)). In addition, the boundary layer around the optimized hull is almost the same as that of the initial one (Figure 3.18(b)). However, the velocity pattern is slightly different, i.e., flow speed decreases a little around transom bottom. The difference of the velocity pattern is consistent with the change of streamlines under the transom bottom and increase of pressure behind the ship stern as shown in Figures 3.17(a), (b) and 3.18(a).

3.2.3 Effects of the initial design variable value (x_{st}) to the optimization results

It is important to note that with the different design values of x_{st} or d_z the system of linear equations (Equation (2.57)) gives different coefficients of the linear equation used in determination of centerline profile (Equation (2.56)). The bottom profiles of the modified hull forms, therefore, are not the same. The initial hull forms are then not identical. The pressure resistance coefficients of the modified hull forms are different, consequently. Thus, sensitivity coefficients of the SQP analysis makes the line search procedure give different values for the next design variables. Then the optimized hull forms is maybe different following the changes of the design values. Effects of the initial design values, therefore, should be taken into the investigation. In this study, effects of the different initial values of x_{st} to the final optimized results are included in the examination. Two different values $x_{st} = 0.5$ and $x_{st} = 0.51$ are selected as the initial designs of the optimization processes to investigate effects of the initial values to the final optimization results. Note that, the initial and optimized hull forms as well as flow fields surrounding themselves of the optimization process by using $x_{st} = 0.51$ has been already presented and discussed in the previous section.

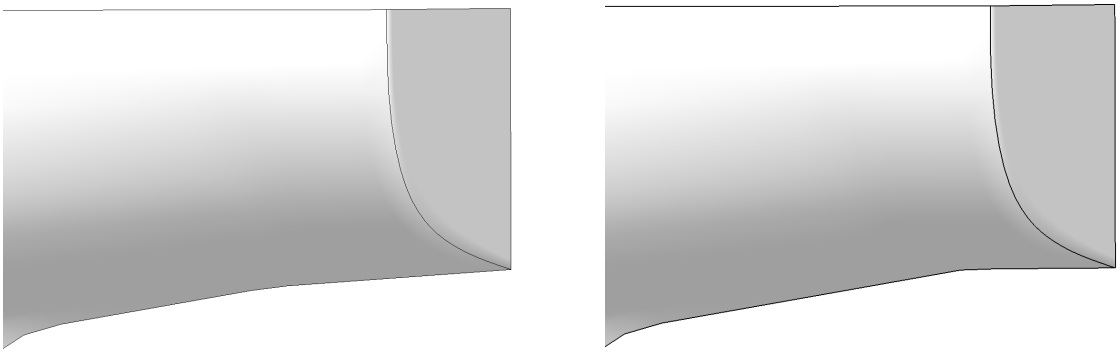

(a) Initial $x_{st} = 0.5$ (b) Initial $x_{st} = 0.51$

Figure 3.19: Overhangs of the initial hull forms with different initial values of design variable x_{st}.

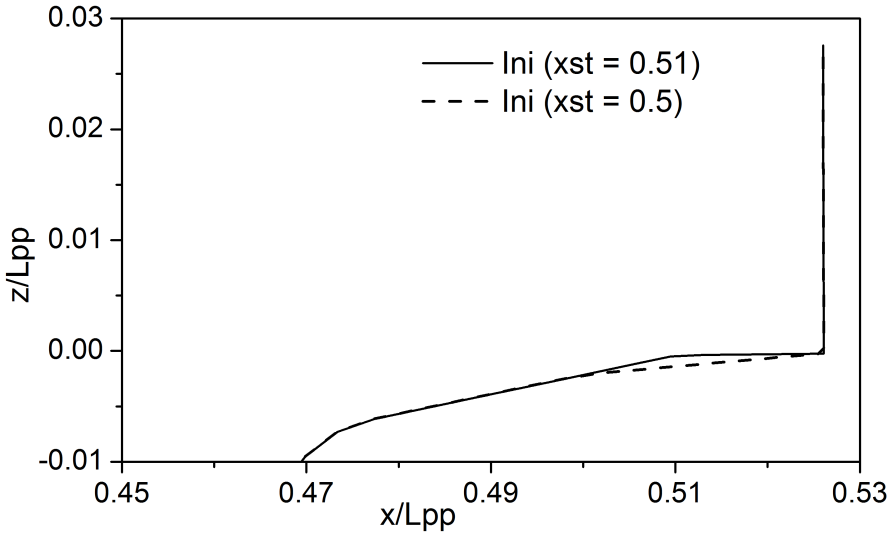

(a) Centerline profiles

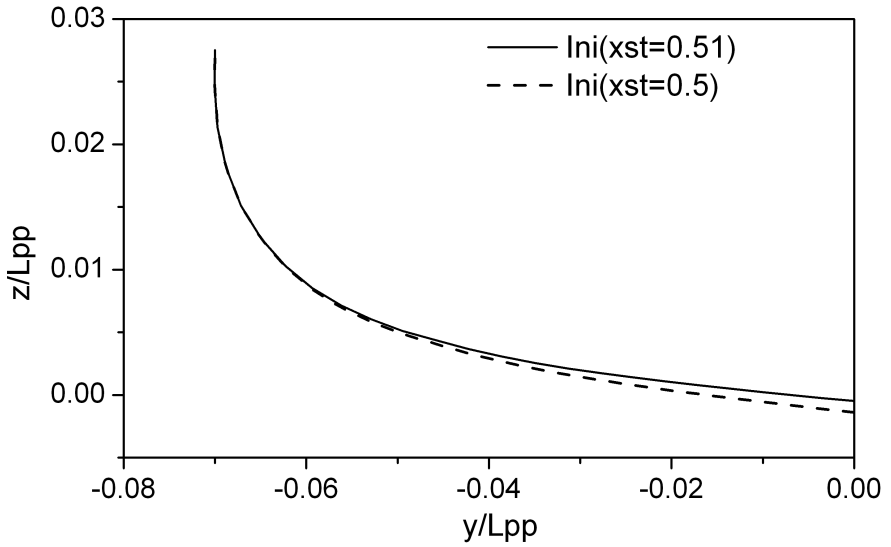

(b) Framlines at $x/L_{pp} = 0.51$

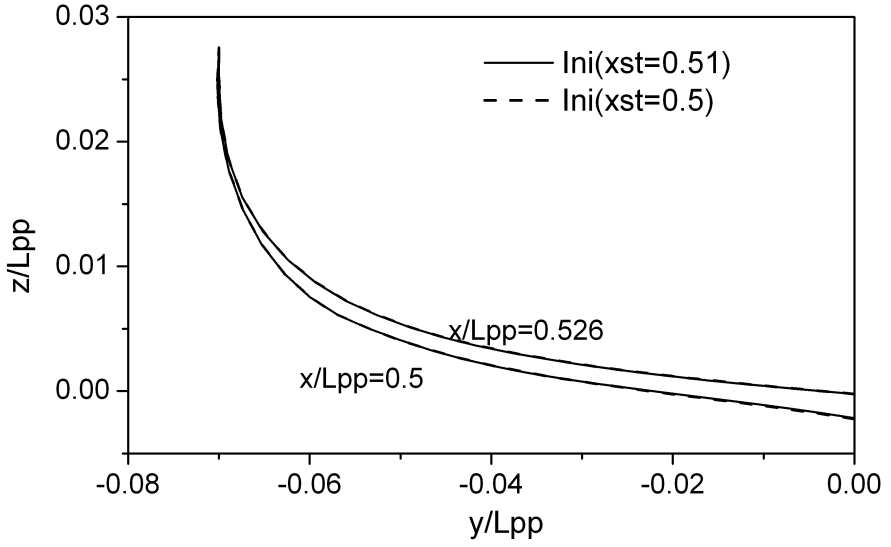

(c) Framlines at $x/L_{pp} = 0.526$

Figure 3.20: Comparisons of the centerline profiles and framelines of the initial hull forms by using $x_{st} = 0.5$ and $x_{st} = 0.51$.

Differences of the initial overhang shapes by using the different values $x_{st} = 0.5$ and $x_{st} = 0.51$ are presented in Figure 3.19. Centerline profiles and framelines of the initial hull forms are compared in Figure 3.20. Obviously, since the starting point of the modified overhang moves forward, the straight line connecting the starting point to the ending point of the hull form by using $x_{st} = 0.5$ is lower than that of the initial hull form (Figure 3.20(a)). The centerline profile of the hull form by using $x_{st} = 0.51$, while, is identical to that of the initial hull form because its starting point is on the flat bottom profile of the initial ship hull. The initial framelines in the modified domain of ship hulls are also slightly different (Figure 3.20(b)) due to the vertical translation (d) (Equation (2.59)) of the grid points along centerline profiles are not the same in each case though the framelines of the domain before station $x/L_{pp} = 0.5$ and at the stern end plane ($x/L_{pp} = 0.526$) are identical (Figure 3.20(c)).

The optimization process by using $x_{st} = 0.5$ as the initial design value is performed with the constraints assigned on the design variables are kept the same as those of the previous case. Histories of the objective function in the optimization processes by using $x_{st} = 0.5$ and $x_{st} = 0.51$ are compared in Figure 3.21. Note that Cp_0 is the initial pressure resistance coefficient of the initial hull form created by using $x_{st} = 0.51$. Histories of the evaluated values of the design variables at each iteration step in the optimization process by using $x_{st} = 0.5$ are presented in Figure 3.22. As shown in Figure 3.21, pressure resistance coefficient of the initial hull form by using $x_{st} = 0.5$ is slightly larger than that of the initial hull form using $x_{st} = 0.51$ (approximately 0.0072%). Augmentation of the initial pressure resistance coefficient comes from the fact that the displacement volume of the initial hull form generated by using $x_{st} = 0.5$ increases a little from that of the hull form generated by $x_{st} = 0.51$. As shown in Figure 3.20, centerline profile and the framelines of the overhang using $x_{st} = 0.5$ are lower and wider than those of the initial ship hull by using $x_{st} = 0.51$. The displacement volume of ship hull using $x_{st} = 0.5$ increases slightly (approximately 0.168%) compared to that of the initial ship hull by using $x_{st} = 0.51$. Furthermore, in contrast with the optimization process by using $x_{st} = 0.51$ that stops after 8 iteration steps (Figure 3.7), the optimization process by using $x_{st} = 0.5$ reaches convergent after 9 iteration steps. The objective function also reduces more than that of the previous case with reduction of the pressure resistance coefficient is approximately 6% from its initial value. Since the solution gets convergent, the evaluated values of design variables in the last 4 iteration steps are mostly the same as depicted in Figure 3.22.

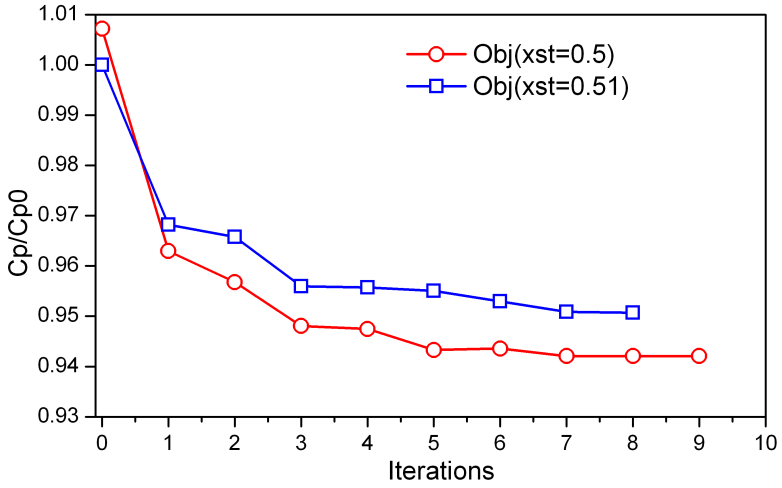

Figure 3.21: Comparison of histories of the objective function of the optimization process using $x_{st} = 0.5$ and $x_{st} = 0.51$.

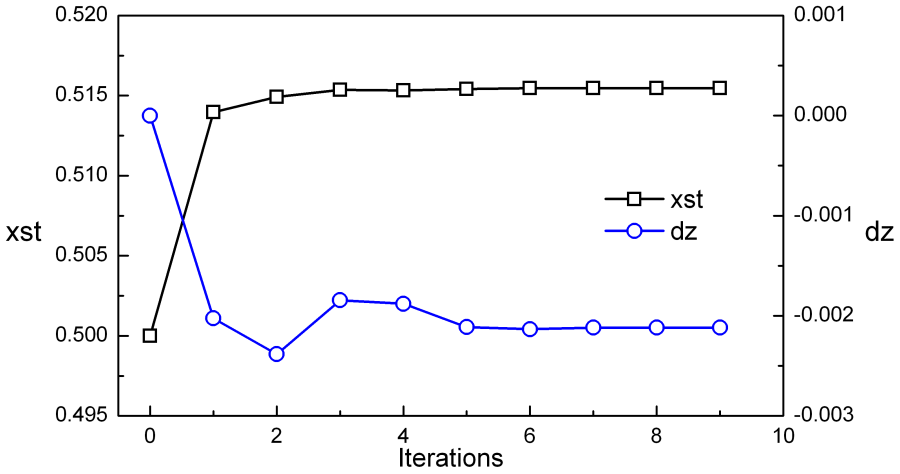

Figure 3.22: Histories of the design values of the optimization process using $x_{st} = 0.5$.

Table 3.6: The computed resistance coefficients of the initial and optimized hull forms using $x_{st} = 0.5$.

Coef.	Total resistance $C_t = \frac{R_t}{0.5\rho U^2 L_{pp}^2}$	Frictional resistance $C_f = \frac{R_f}{0.5\rho U^2 L_{pp}^2}$	Pressure resistance $C_p = \frac{R_p}{0.5\rho U^2 L_{pp}^2}$
Initial	8.21×10^{-4}	5.14×10^{-4}	3.07×10^{-4}
Optimized	8.02×10^{-4}	5.15×10^{-4}	2.87×10^{-4}

Table 3.6 presents the computed resistance coefficients of the initial and optimized hull forms using the initial design $x_{st} = 0.5$. On the contrary to the optimization process

using x_{st} = 0.51 that makes frictional resistance coefficient of the optimized hull form unchanged, the frictional resistance coefficient of the optimized ship hull by using x_{st} = 0.5 increases a little. However, by the larger reduction of pressure resistance coefficient (approximately 6%) its absolute resistance coefficient of the optimized ship hull decreases more than that of the optimized ship hull by using x_{st} = 0.51. Total resistance coefficient of the optimized one by using x_{st} = 0.5 reduces approximately 2.31% from that of the initial ship hull (reduction of the total resistance of the optimized hull form by using x_{st} = 0.51 is approximately 1,88%).

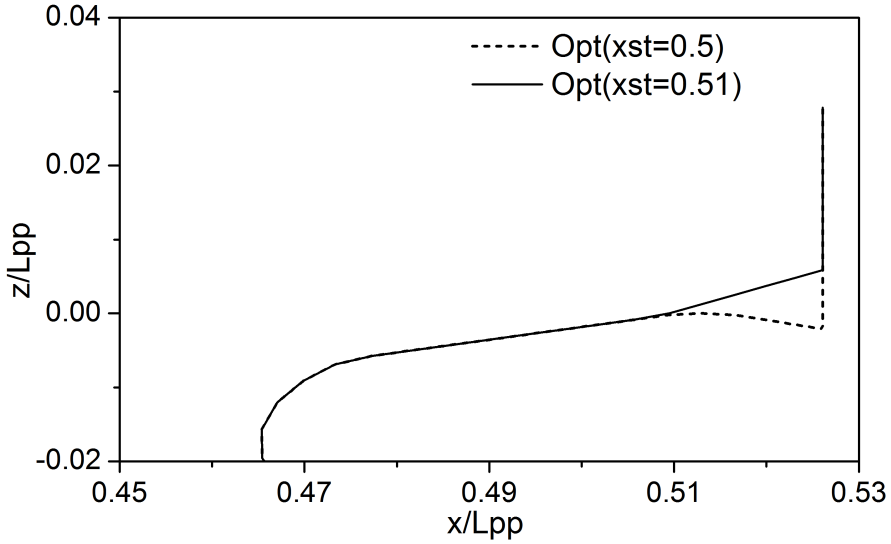

(a) Centerline profiles

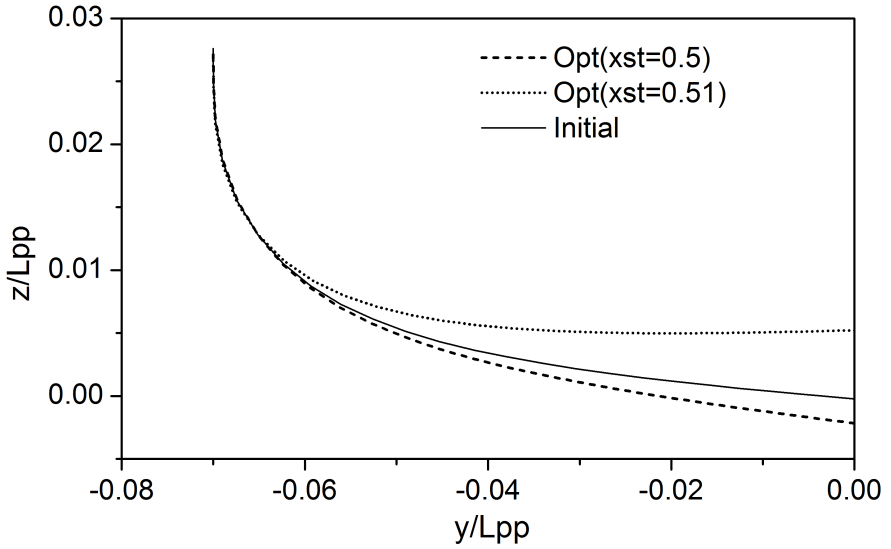

(b) Framlines at the stern end plane

Figure 3.23: Centerline profiles and framelines of the optimized ship hulls by using different initial designs of x_{st} = 0.5 and 0.51.

Figure 3.23 compares centerline profiles and framelines at the stern end of the optimized ship hull by using $x_{st} = 0.5$ and $x_{st} = 0.51$. Figure 3.24 presents the initial and optimized overhang shapes by using $x_{st} = 0.5$. On the contrary to the case using $x_{st} = 0.51$ that makes the stern end of the initial hull form move up and the optimized transom gets convex shape (Figure 3.10); with $x_{st} = 0.5$ the transom height at the stern end of the optimized hull is reduced making its transom bottom move down and get a concave shape, consequently (Figure 3.23(a)). The optimized frame line by using $x_{st} = 0.5$, therefore, are also lower than that of the initial one (Figure 3.23(b)).

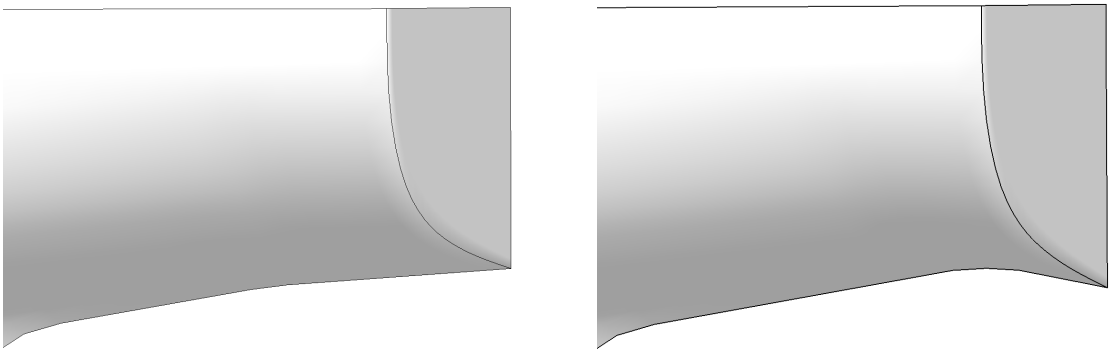

(a) Initial (b) Optimized

Figure 3.24: Overhangs of the initial and optimized hull forms by using $x_{st} = 0.5$.

The distributions of pressure on the overhang surfaces of the initial and optimized hull forms by using $x_{st} = 0.5$ with the views by side and from the behind of ship are compared in Figures 3.25 and 3.26, respectively. As shown in Figures 3.12(a) and 3.25(a), the pressure pattern on the initial overhang surface by using $x_{st} = 0.5$ changes slightly compared to that of the initial overhang surface by using $x_{st} = 0.51$ since transom bottom of the initial hull form using $x_{st} = 0.5$ inclines a little from the initial one. However, following the change of the initial design value x_{st} the pressure distributions on the optimized overhang surfaces are significantly different (Figures 3.12(b) and 3.25(b)). While pressure on the optimized transom by using $x_{st} = 0.51$ becomes higher at the aft end, pressure on the optimized stern by using $x_{st} = 0.5$ increases at the inflecting point and decreases at the stern end. And also from Figure 3.13, with the upward transom shape the pressure distribution in the aft part ahead of the modified domain of the optimized transom by using $x_{st} = 0.51$ are significantly different from its initial; however, the distribution of pressure in same region under the concave shape of the optimized stern by using $x_{st} = 0.5$ are almost the same as that of the initial hull form (Figure 3.26).

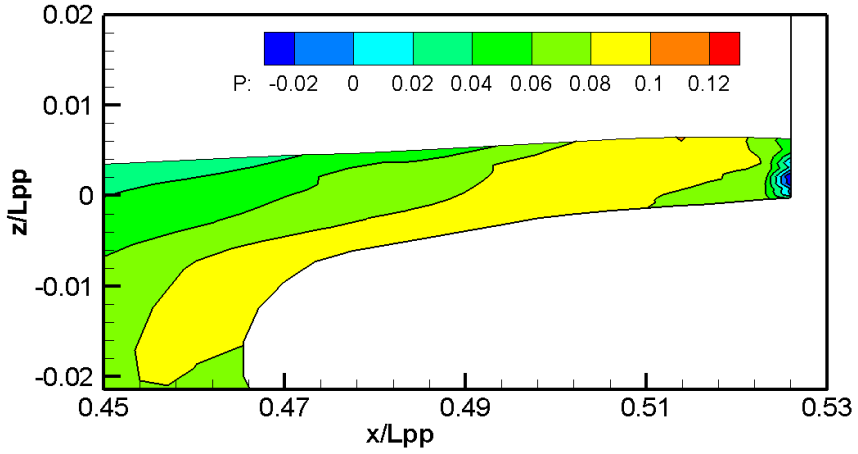

(a) Initial

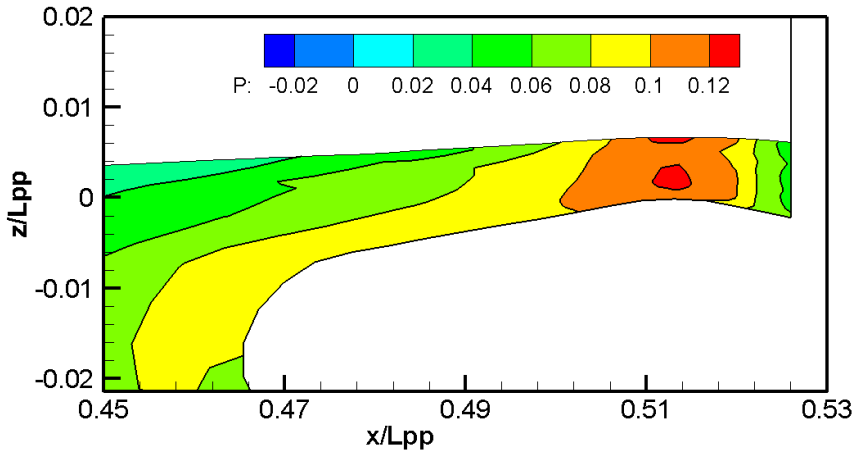

(b) Optimized

Figure 3.25: Pressure distributions on the initial and the optimized overhang surfaces by using $x_{st} = 0.5$.

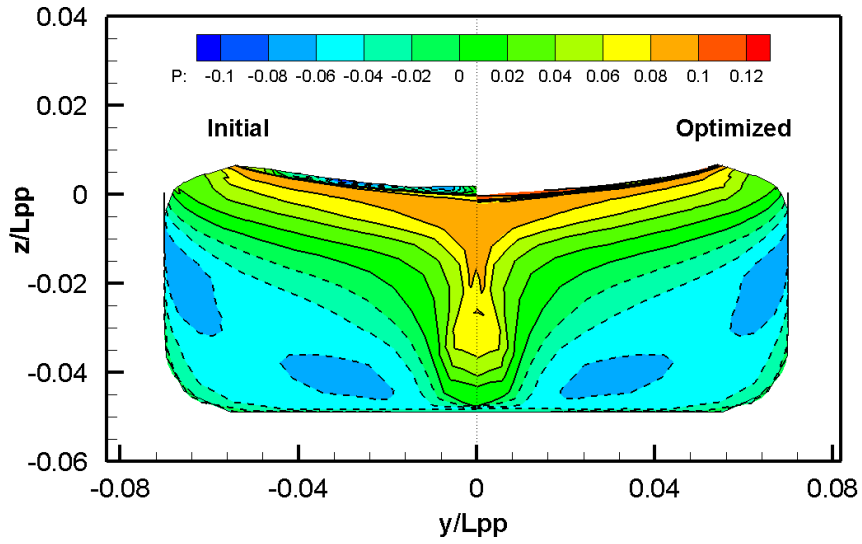

Figure 3.26: Pressure distributions on the initial and the optimized hull surfaces in the aft parts using $x_{st} = 0.5$.

The distributions of pressure and frictional components of resistances along the initial and optimized hull forms using $x_{st} = 0.5$ are compared in Figure 3.27. Similarly to the previous case, the difference of frictional resistance cannot be observed by this plot since augmentation of the frictional resistance are small. The similarity of pressure patterns on the hull surfaces makes the local pressure resistance of ship hulls are almost the same. Pressure resistance in the aft part of the optimized one increases at the inflecting point (around $x/L_{pp} = 0.5$) before decreases at the aft end that corresponds to the pressure distributions on the optimized overhang surface as depicted in Figure 3.25(b).

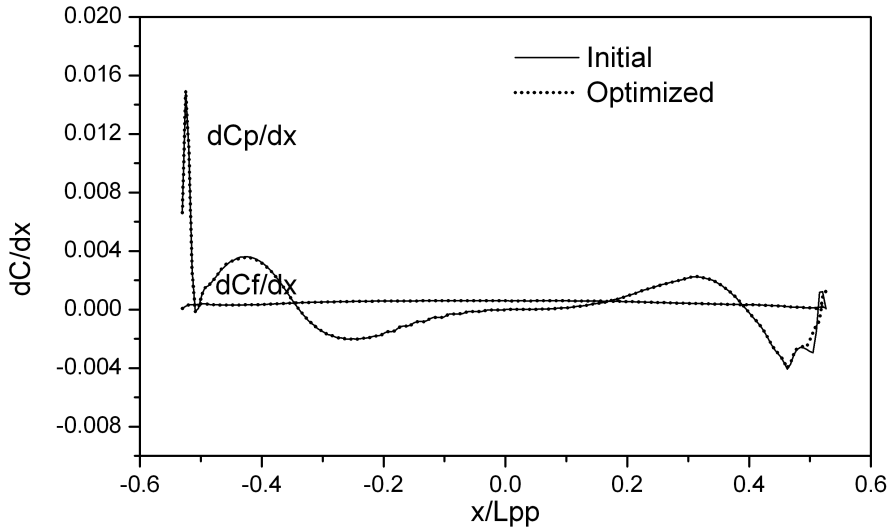

Figure 3.27: The longitudinal distribution of pressure and frictional resistances of ship hulls using $x_{st} = 0.5$

Table 3.7: Trim, sinkage and dipping of the fore, aft perpendiculars of the initial and optimized ship hulls using $x_{st} = 0.5$.

Coef.	Sinkage $s = \frac{d_a + d_f}{2L_{pp}}$	Trim $t = \frac{d_a - d_f}{L_{pp}}$	d_f	d_a
Initial	1.91×10^{-3}	-3.21×10^{-3}	3.51×10^{-3}	0.30×10^{-3}
Optimized	1.89×10^{-3}	-3.43×10^{-3}	3.61×10^{-3}	0.17×10^{-3}

The computed trim, sinkage and the dipping values at the fore (d_f) and at the aft (d_a) perpendiculars of the initial and optimized hull forms by using $x_{st} = 0.5$ are listed in Table 3.7. Since the differences of hull geometries of the initial hull forms generated by using $x_{st} = 0.5$ and $x_{st} = 0.51$ are only at the transom stern, the computed trim and

sinkage of these two initial hull forms are almost the same as presented in Tables 3.5 and 3.7. However, the changes of the dipping values at the bow and aft parts make trim angle of the optimized hull by using x_{st} = 0.5 differ significantly from that of the optimized hull by using x_{st} = 0.51. The optimized transom by using x_{st} = 0.51 reduces the dip of the fore part and increases the dip of the aft part making the trim angle smaller than that of its initial hull form. While, the optimized transom by using x_{st} = 0.5 causes the dipping value of the fore perpendicular increase and the dipping of the aft perpendicular decrease from those of the initial one. The running trim angle of the optimized hull form by using x_{st} = 0.5 is larger than that of the initial one, consequently.

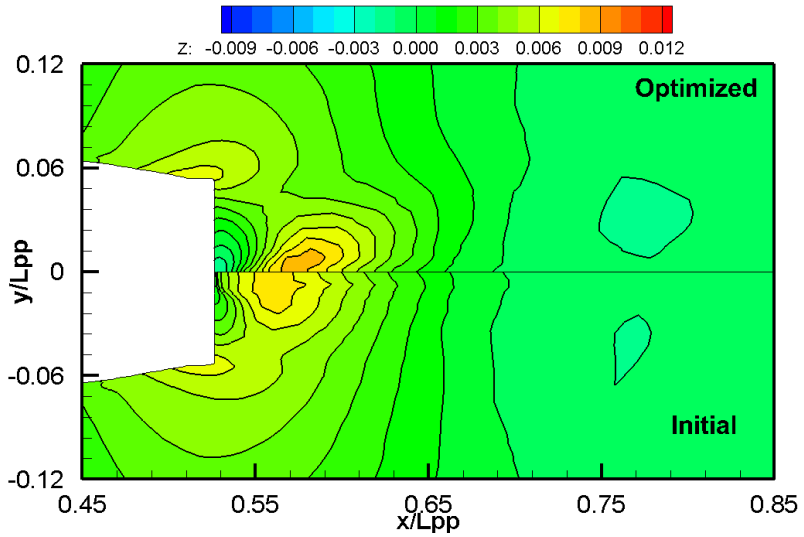

Figure 3.28: Wave patterns around the initial and optimized transom sterns using x_{st} = 0.5.

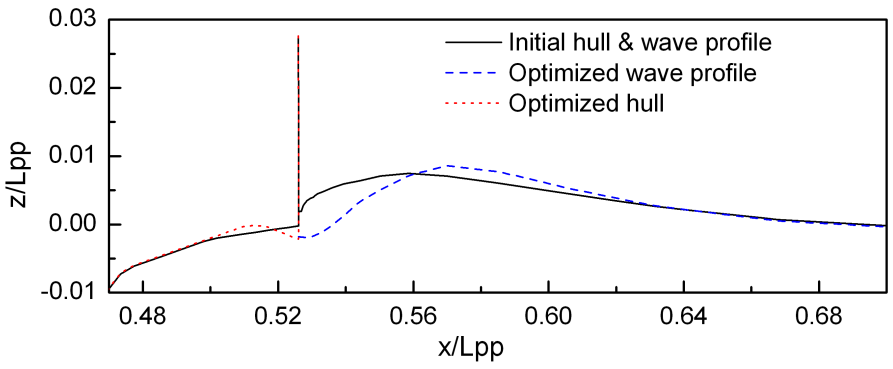

Figure 3.29: Wave profiles behind the stern ends of ship hulls using x_{st} = 0.5.

The wave patterns around the transom stern and wave profiles behind the stern end of the initial and optimized hull forms with x_{st} = 0.5 are compared in Figures 3.28 and 3.29,

respectively. Obviously, the wave peak behind the stern end of the optimized hull form moves further downstream and the hollow just behind the stern end become wider and dipper compared to those of the initial one. The dipper hollow behind the stern end there also makes the wetted transom of the initial ship hull become dry with the free surface flow leaves the stern end at the transom bottom (Figure 3.29).

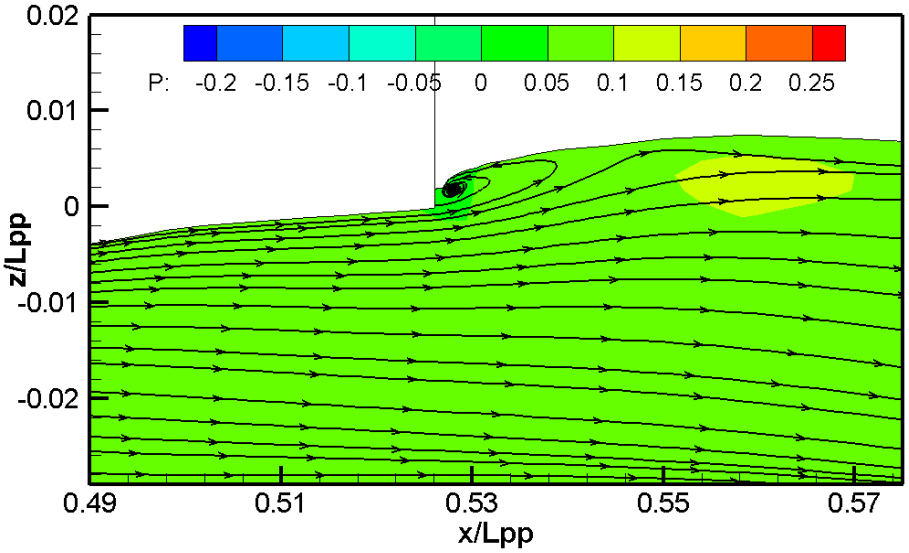

(a) Initial

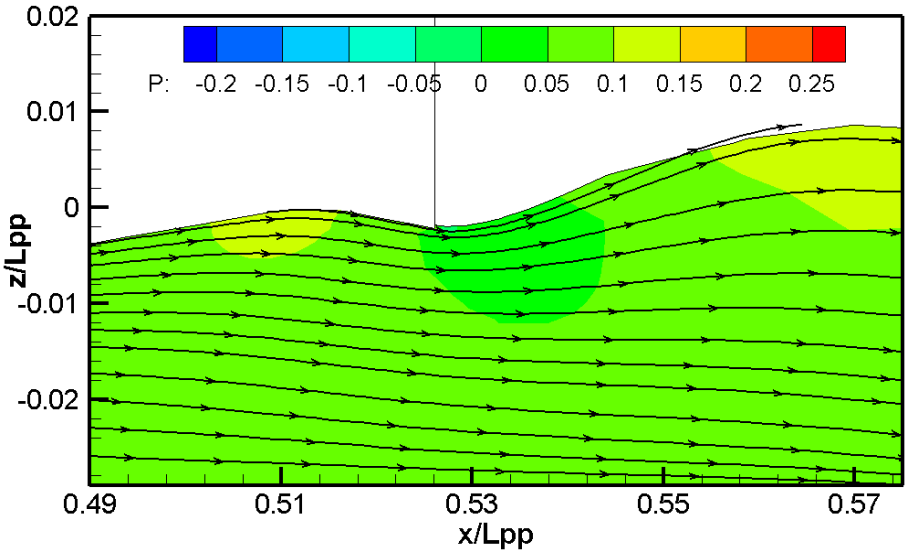

(b) Optimized

Figure 3.30: The simulated streamlines under initial and optimized transom bottoms using $x_{st} = 0.5$.

The simulated streamlines in the symmetry plane of the initial and optimized ship hulls by using $x_{st} = 0.5$ are compared in Figure 3.30. Similarly to the optimized stern by using $x_{st} = 0.51$, the upward stern shape makes flows under the initial transom bottom can

rise up. A part of the rising up flows is separated behind the stern end making a vortex is created there (Figures 3.17(b) and 3.30(a)). However, with the downward stern shape that makes the transom bottom lower than the still water level and the optimized overhang is immersed at rest, streamlines near the hull surface of the optimized hull form move down following the change of hull geometry. The flow separation phenomenon is eliminated behind the optimized stern end and the vortex which appears in the initial ship hull is not created there (Figure 3.30(b)). The flow speed behind the optimized stern end plane also increases.

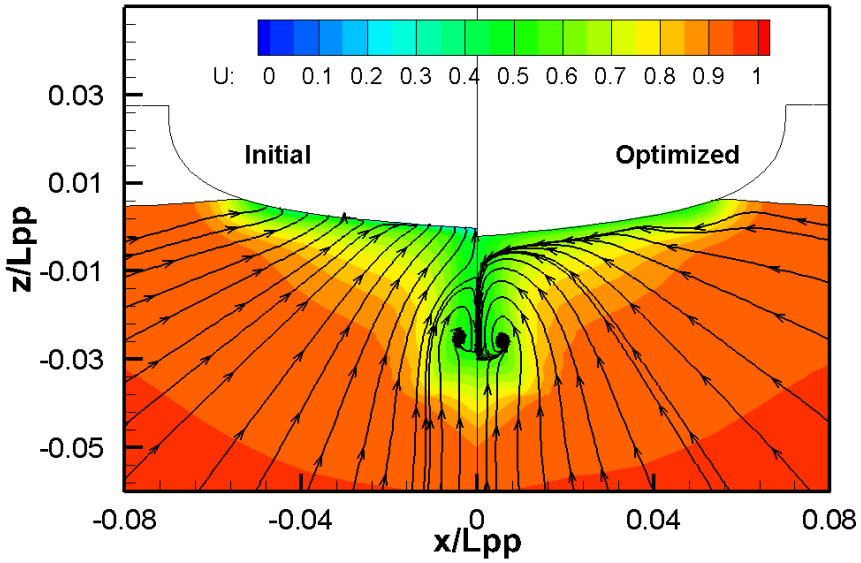

(a) Streamlines

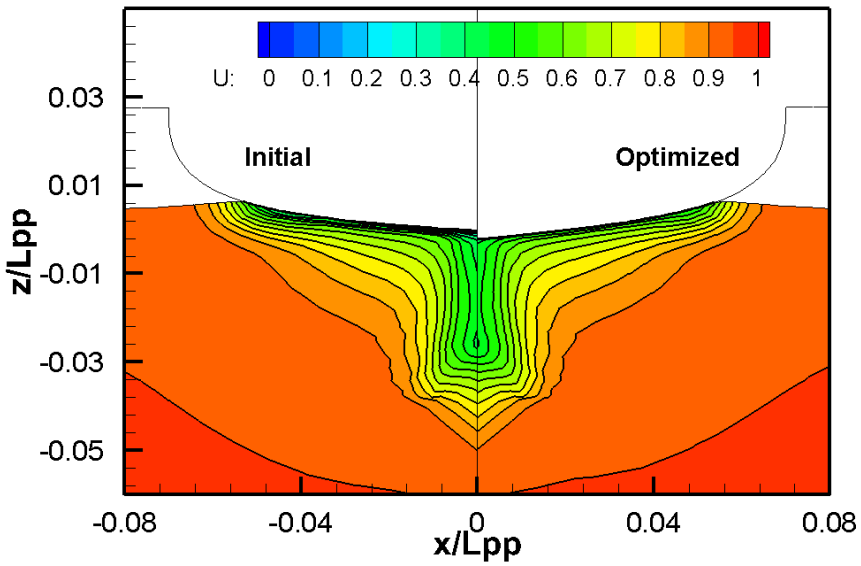

(b) Velocity

Figure 3.31: Streamlines and the axial distribution of velocity at the stern end plane of the initial and optimized hull forms by using $x_{st} = 0.5$.

Figure 3.31 compares the simulated streamlines and velocity patterns under transom bottom at the stern end plane ($x/L_{pp} = 0.526$) of ship hulls. With the upward stern shape, flows under the initial transom bottom are risen up. Streamlines under the initial transom bottom, thus, go up mostly. While, by decrease of the transom height making the optimized transom bottom lower the still water level, streamlines of the optimized ship hull go down and meet each other at the wake region. In addition, the velocity patterns of ship hulls are almost the same. The boundary layer under the optimized hull does not show big differences compared to that of the initial one.

3.2.4 Effects of the weight function to the final optimization results

As shown in Figure 2.9, following the change of the modification functions (from linear form to sine form), the modified framelines are slightly different. The final optimized results of the optimization process, therefore, maybe differ from each other. In order to investigate effects of the modification functions on the optimized results, optimization processes by using different modification functions should be carried out and compared with each other. In this section, the optimized hull form based on the sine form (Equation (2.62)) are compared to that of the optimized hull form by using the linear form (Equation (2.61)). The optimization processes are performed with the initial values of the design variables are set as $x_{st} = 0.5$ and $d_z = 0.0$, respectively. The constraints assigned on the design variables are set the same as those of the previous cases.

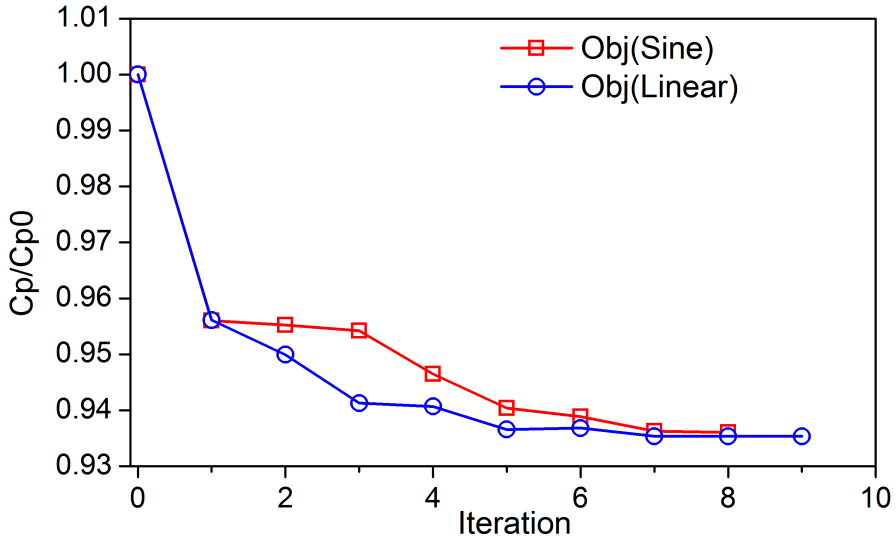

Figure 3.32: Pressure reduction during the optimization processes using different weight function.

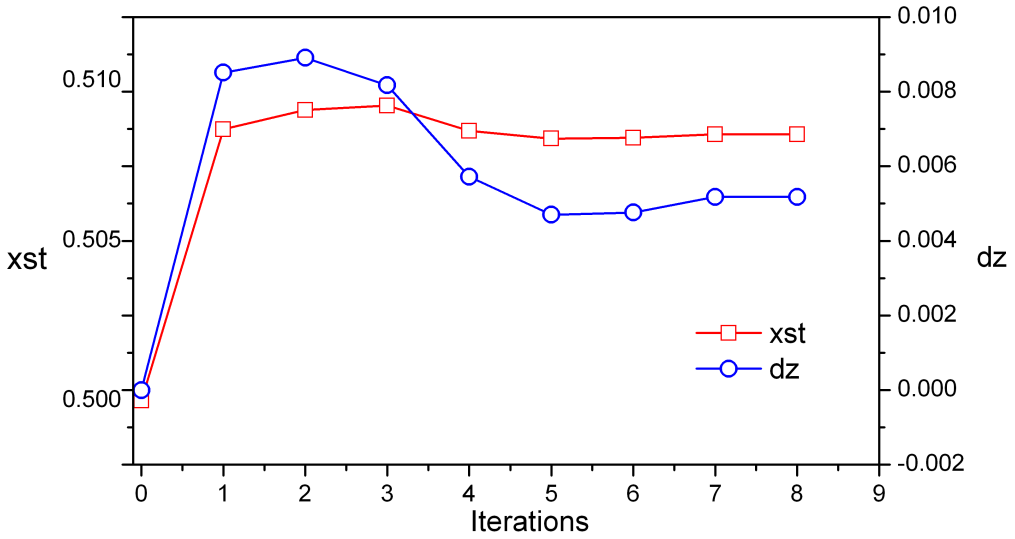

Figure 3.33: Histories of the design variable values during the optimization process using sine weight function.

Histories of the objective function of the optimization processes by using the sine and linear modification functions are compared in Figure 3.32. The determined values of the design variables at each iteration step through the optimization process using the sine function are depicted in Figure 3.33. As shown in Figure 3.32, the minimized values of the objective functions by using the linear and sine functions are almost the same with reductions of pressure resistance are approximately 6% from that of the initial one. In contrast with the linear weight function that makes the iteration process converge after 9 iteration steps, the optimization process using the sine form terminates after 8 iteration loops when the change in successive values of the design variables became too small. Values of the design variables determined by the SQP method in the last two iteration steps are almost the same as shown in Figure 3.33.

Table 3.8: The computed resistance coefficients.

Coef.	Total resistance $C_t = \frac{R_t}{0.5\rho U^2 L_{pp}^2}$	Frictional resistance $C_f = \frac{R_f}{0.5\rho U^2 L_{pp}^2}$	Pressure resistance $C_p = \frac{R_p}{0.5\rho U^2 L_{pp}^2}$
Initial	8.21×10^{-4}	5.14×10^{-4}	3.07×10^{-4}
Optimized	8.02×10^{-4}	5.14×10^{-4}	2.89×10^{-4}

The computed resistance coefficients of the initial and optimized ship hulls by using the sine function are compared in Table 3.8. The computed results show the same ten-

dency as those of two previous cases. The difference of frictional resistance between the initial and optimized hull forms can be negligible. The decrease of total resistance (approximately 2.31%) is mostly due to the reduction of pressure resistance (approximately 6%) by the change of stern shape of the optimized ship hull.

Figure 3.34 compared the optimized overhang shape using the linear and sine functions. The centerline profiles and framelines at the stern end plane of the initial hull form together with the optimized ones by using the linear and sine functions are compared in Figure 3.35. As shown in Figure 3.35(a), while the linear weight function decreases the initial transom height at the stern end, the optimized transom height by using the sine weight function increases making the optimized transom bottom move up and become a convex shape. Following the reduction of transom height, the optimized frame line also rises up completely from the still water level (Figure 3.35(b)). The optimized overhang by using the sine weight function, therefore, is in the air.

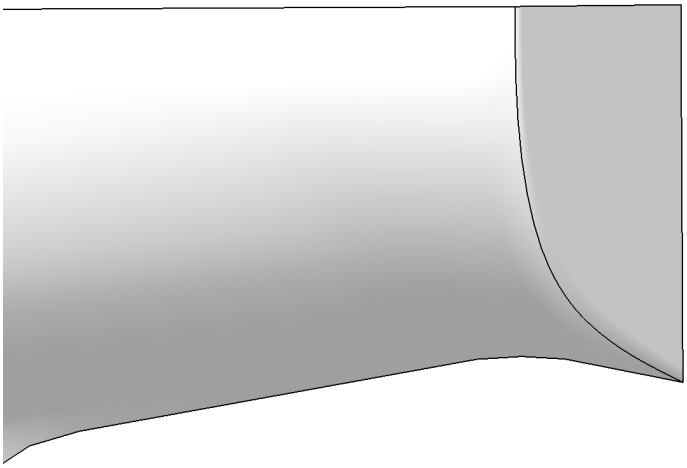

(a) Optimized by linear function

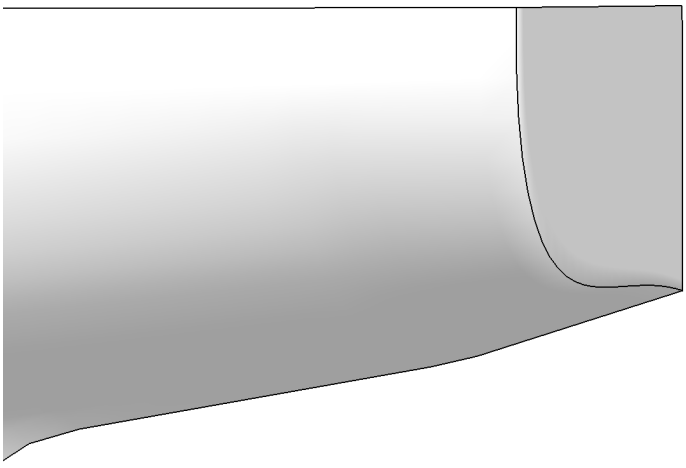

(b) Optimized by sine function

Figure 3.34: Comparison of the optimized overhang by using linear and sine functions.

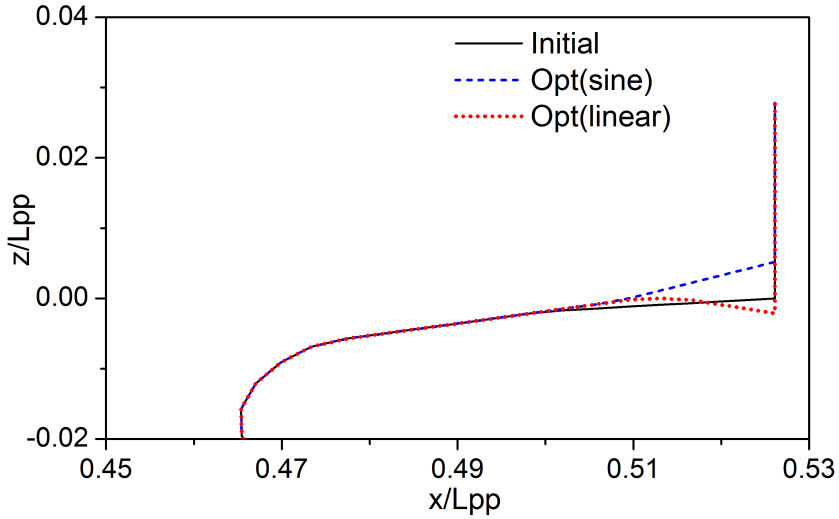

(a) Bottom profiles

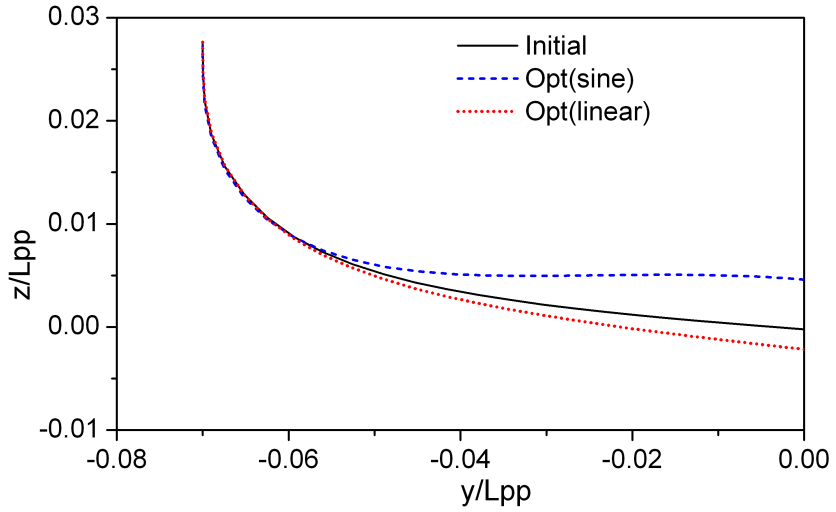

(b) Frame lines

Figure 3.35: Bottom profiles at the center plane and framelines at the stern end plane (x/L_{pp} = 0.526) of the optimized hull forms using different functions.

Figures 3.36-3.40 show comparisons of the distributions of pressure on the overhang surfaces and on the hull surfaces of the aft part, the wave patterns around the transom stern as well as the velocity pattern and streamlines at the stern end plane of the optimized ship hull by using the linear and sine modification functions. With the upward stern shape and also based on the computed and simulated results, it can be concluded that flow field around the optimized stern shape by using the sine modification function is similar to that of the optimized ship hull by using x_{st} = 0.51.

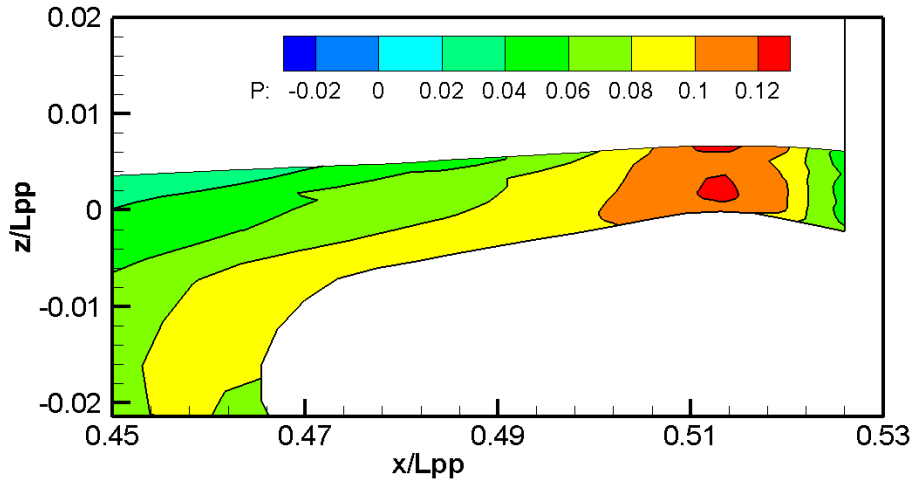

(a) Optimized by linear weight function

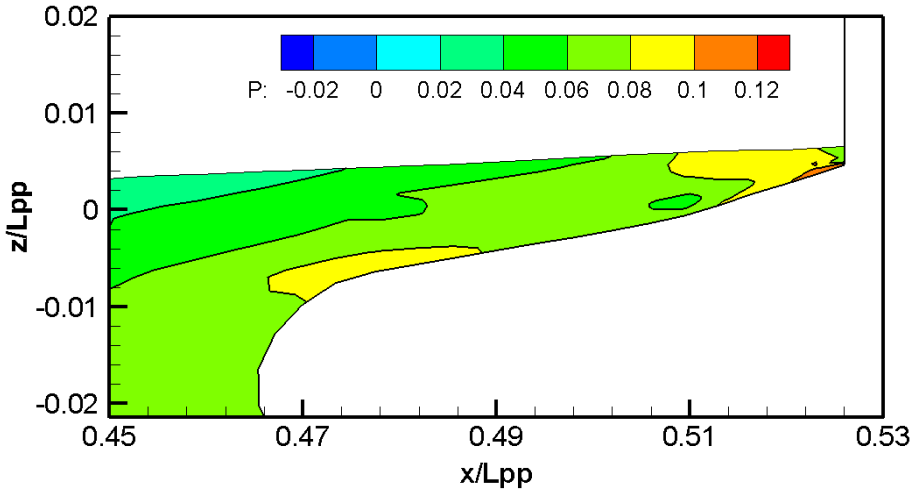

(b) Optimized by sine weight function

Figure 3.36: Pressure patterns on the optimized overhang surfaces by using different modification functions.

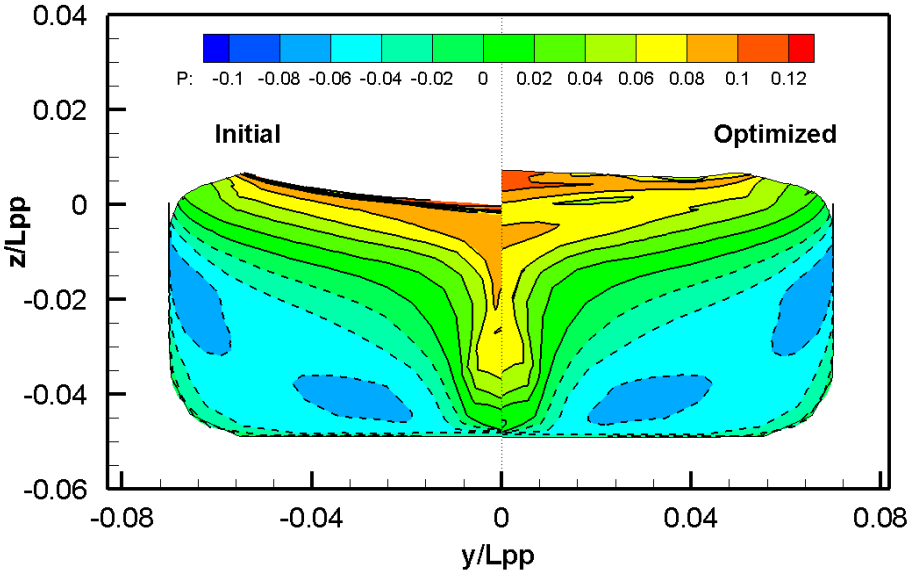

Figure 3.37: Pressure distributions on the aft part of the optimized hull surfaces by using the linear and sine weight functions.

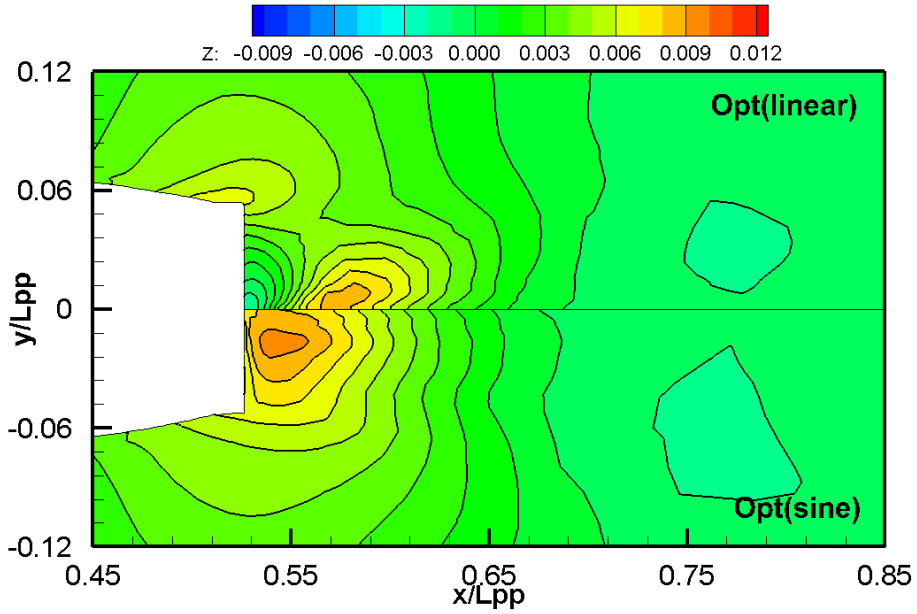

Figure 3.38: Wave patterns around the optimized transom sterns using the linear and sine weight functions.

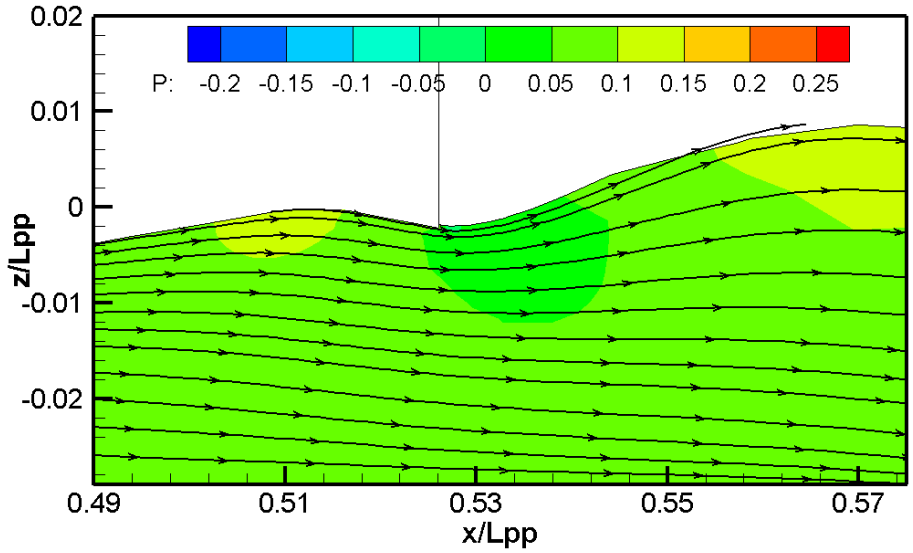

(a) Optimized by linear weight function

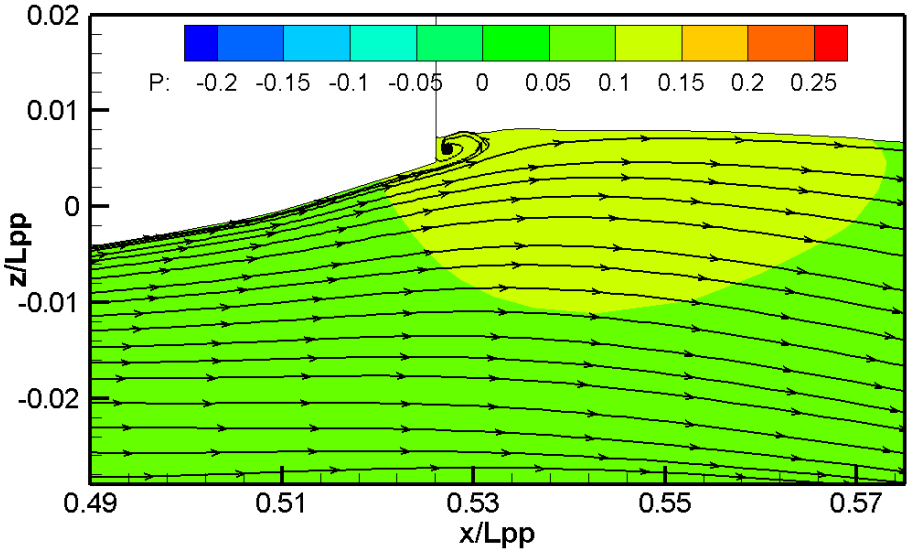

(b) Optimized by sine weight function

Figure 3.39: Comparison of the streamlines in the center plane of the optimized ship hulls by using the different modification functions.

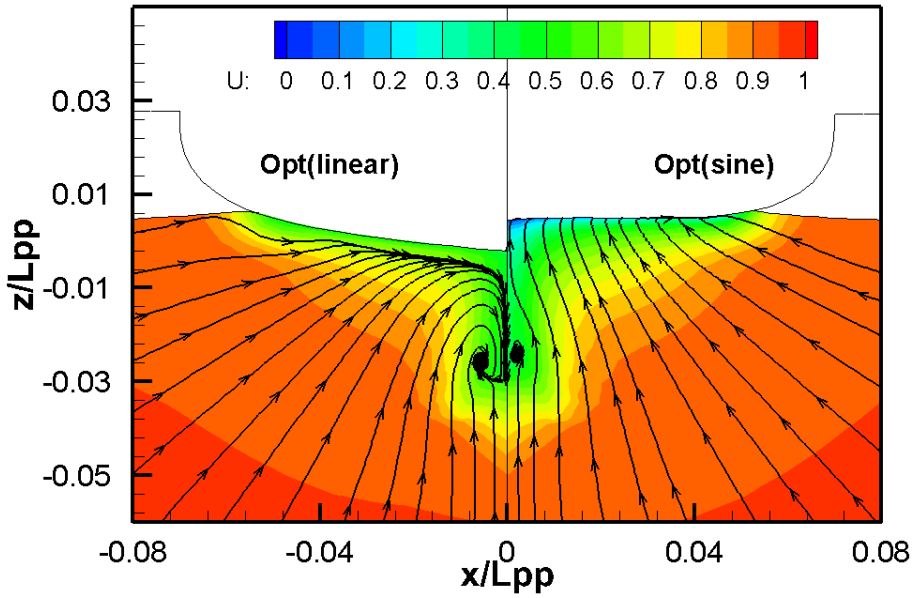

(a) Streamlines function

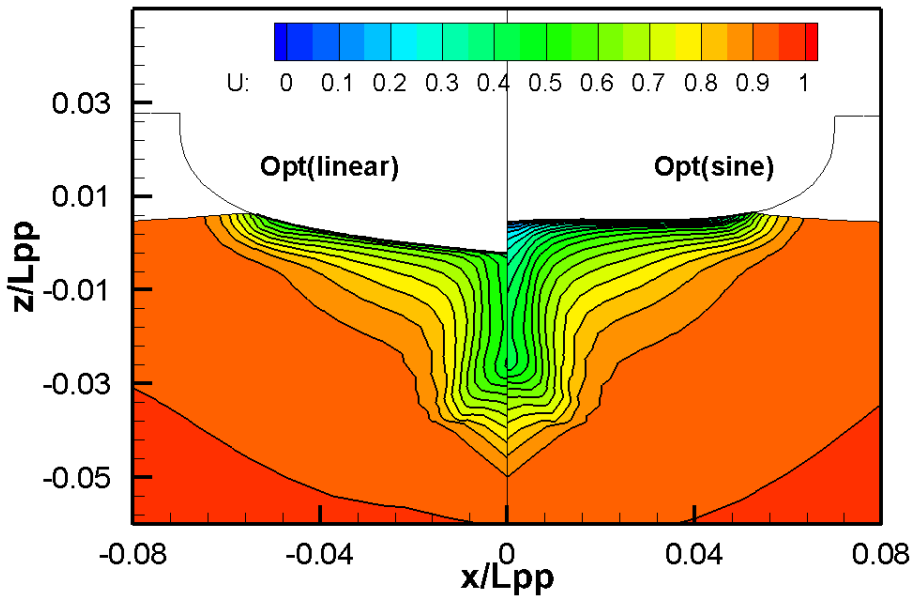

(b) Wake

Figure 3.40: Comparison of streamlines and wakes at the stern end plane of optimized hull form using different modification functions.

3.2.5 Dependences of the optimized results on the initial designs and modification functions

As presented and discussed in the previous sections whenever either the initial value of x_{st} or the frameline modification functions change, the optimized results are significantly different between each other. It can be concluded that the optimized result for all cases are not unique. Therefore, it is necessary to examine the effects of the initial design

variables as well as of the modification functions to the final optimized results. Fours optimization cases defined as presented in Table 3.9 are selected in the investigation for this purpose in this study.

Table 3.9: Optimization cases.

	Case I	Case II	Case III	Case IV
Initial $-x_{st}$	0.51	0.5	0.5	0.51
Initial $-d_z$	0.0	0.0	0.0	0.0
Modification function	Eq. (2.61)	Eq. (2.61)	Eq.(2.62)	Eq. (2.62)

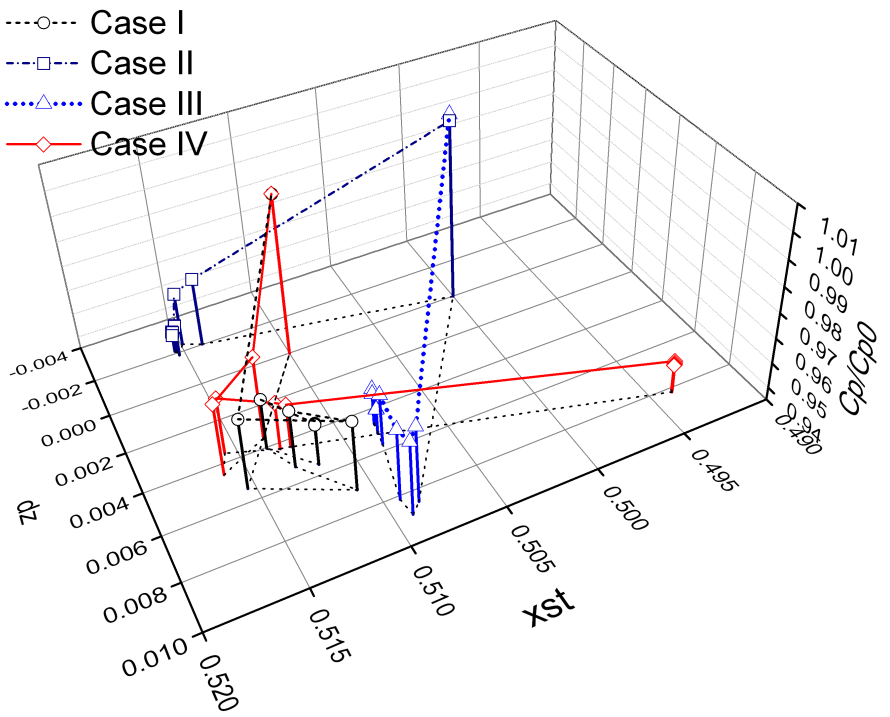

Figure 3.41: Dependence of the optimized results on the initial designs and modification functions.

Table 3.10: Optimized values of the design variables.

	Case I	Case II	Case III	Case IV
Objective function	0.951	0.935	0.936	0.944
Optimized $-x_{st}$	0.5084	0.515	0.5083	0.494
Optimized $-d_z$	5.865E-3	-2.118E-3	5.183E-3	8.122E-3

Figure 3.41 shows histories of the objective function together with design values of x_{st} and d_z throughout the optimization processes. The optimized values of the design variables in each case are presented in Table 3.10. Obviously, the optimized design variables are significantly different following the changes of the initial values and of the framline modification functions. While the designed values of d_z at each step in the optimization processes of the Case I, Case III and Case IV are positive, they are negative in the Case II. The designed values of x_{st} at each iteration step of the optimization processes also show the different tendencies (Figure 3.41). The differences of the designed variables values come from the fact that the gradients of the objective function have different signs between each case. With the same increment step ε of the design value d_z, the pressure resistance coefficient of the hull form created by value of $d_z + \varepsilon$ of the Cases I, II and IV is smaller than that of the hull form created by value of d_z–ε. The gradient of objective function in these cases, thus, is negative. The line search procedure then increases value of the design variable d_z for the next iteration steps (Table 3.11). On the contrary, the pressure resistance coefficient of the ship hull created by value of $d_z + \varepsilon$ is larger than that of the hull form created by value of $d_z - \varepsilon$ during the optimization process of the Case II. The gradient of objective function in this case is positive and the subsequent line search procedure decreases value of d_z for the next iteration steps (Table 3.12). The final optimized transom shapes in this case, thus, are completely different from that of the three other cases, consequently (Figures 3.42, 3.43). In addition, since the optimized solutions are significantly different, it can be concluded that the optimized solutions in each case are the local solutions of the present method. A better algorithm such as the Genetic Algorithm that can solve efficiently this kind of problem should be developed for finding the final optimized solutions.

Table 3.11: Sensitivity analysis the gradient of the objective function of the Case I.

Case I			
$x_{st} = 0.51, d_z = 0.0d0, \varepsilon =$ 1.0E-3			
$x_{st}, d_z \pm \varepsilon$	C_p	$\partial C_p/\partial d_z$	$d_z^{(1)}$
0.51, 1.0E-3	1.514E-4	-2.91E-3	5.424E-3
0.51, -1.0E-3	1.536E-4		

Table 3.12: Sensitivity analysis the gradient of the objective function of the Case II.

Case II			
$x_{st} = 0.51, d_z = 0.0d0, \varepsilon =$ 5.0E-4			
$x_{st}, d_z \pm \varepsilon$	C_p	$\partial C_p / \partial d_z$	$d_z^{(1)}$
0.50, 5.0E-4	1.542E-4	3.180E-4	5.424E-3
0.5, -5.0E-4	-2.025E-4		

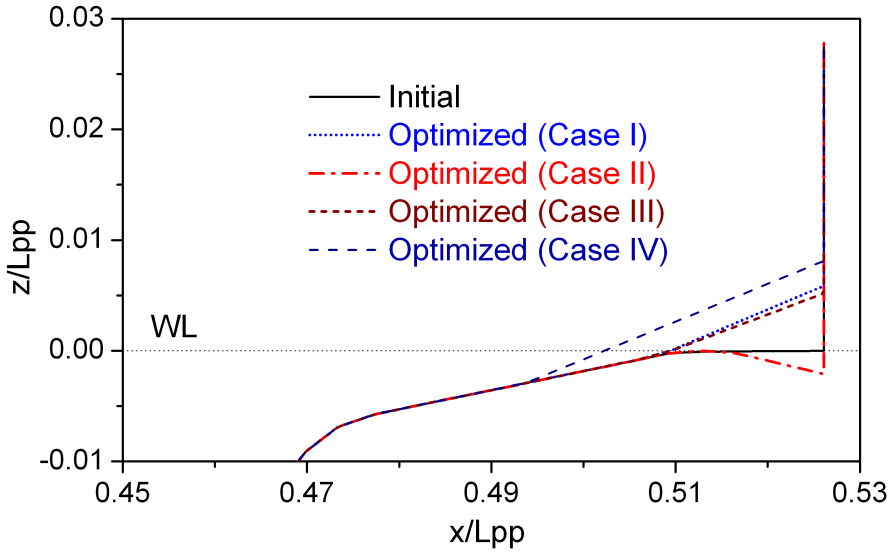

(a) Profiles.

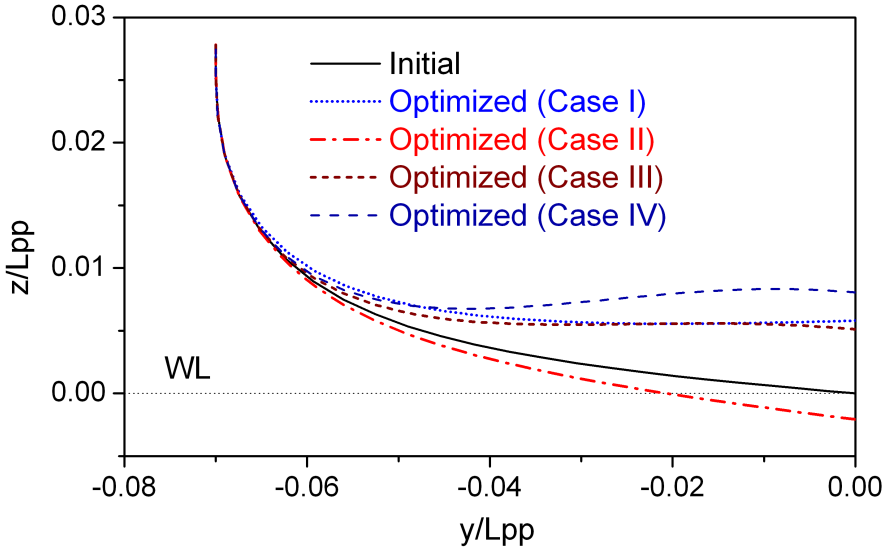

(b) Framelines

Figure 3.42: Comparison of the initial and optimized overhangs

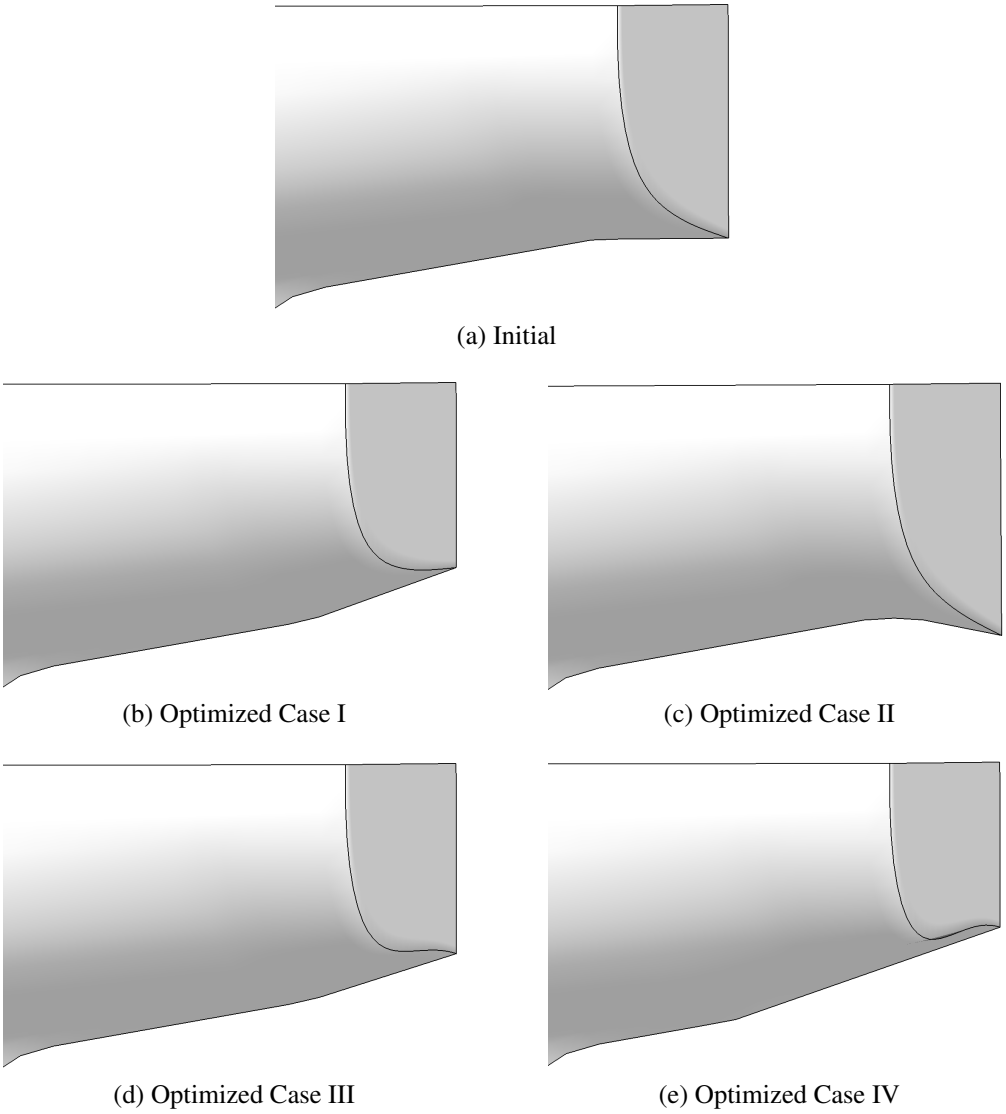

(a) Initial

(b) Optimized Case I

(c) Optimized Case II

(d) Optimized Case III

(e) Optimized Case IV

Figure 3.43: Comparison of the initial and optimized overhangs.

Figure 3.44 show contour of the pressure resistance coefficient of the hull forms following the changes of the design variables values. The computed pressure resistance coefficients are presented in Tables A.1 and A.2 of the Appendix A. For some cases with short distance from the x_{st} to the x_{end} and deep values of d_z, i.e., for instance $x_{st} = 0.525$ and $d_z = -0.003$ that makes the negative skewness of the computational domain, the computed pressure resistance coefficients could not be estimated. Then, the corrected data are used in approximation of contour as shown in Figure 3.44. Obviously, for both the linear and sine functions the pressure resistance coefficients of the corresponding hull forms show the same tendency, i.e., the lower zone of pressure resistance coefficient is in the ranges of $0.51 \leq x_{st} \leq 0.525, -0.003 \leq d_z \leq 0.0$ or $0.49 \leq x_{st} \leq 0.52, 0.003 \leq d_z \leq 0.009$. This is consistent with the optimized results of all 4 cases as shown above. In order

to get the best optimized hull form, a better algorithm such as the Genetic Algorithm that can solve efficiently this kind of problem should be developed.

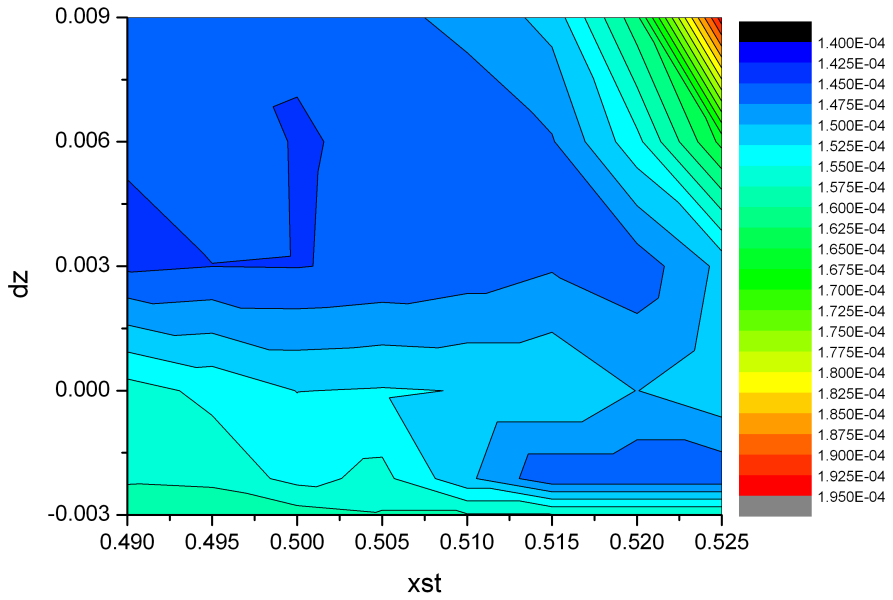

(a) Contour of the pressure resistance coefficients of ship hulls generated by the linear function

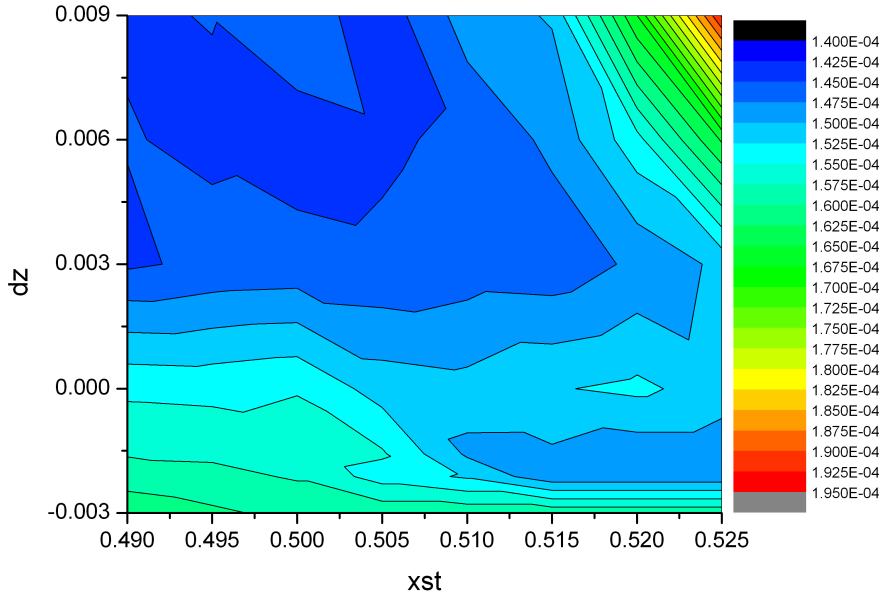

(b) Contour of the pressure resistance coefficients of ship hulls generated by the sine function

Figure 3.44: Contours of the pressure resistance coefficient of the hull form generated by different design variables values.

3.2.6 Grid dependency study

Grid dependency test is essential for CFD analysis, especially in the hull form optimization problem, since the CPU time needed for one computation is expensive, the computational grid is usually made as coarse as possible to obtain the objective function fast. Thus, the computations based on the fine grids should be carried out to validate the optimized results. In the present study, the optimized result of the Case III is selected as a representative one for the grid dependency test. The fine grids are generated based on the coarse grids used for the optimization process. The comparisons of grid dimensions of the fine and coarse grids are shown in Table 3.13. Partial views of the computational domains around the ship stern of the coarse and fine grids are depicted in Figure 3.45.

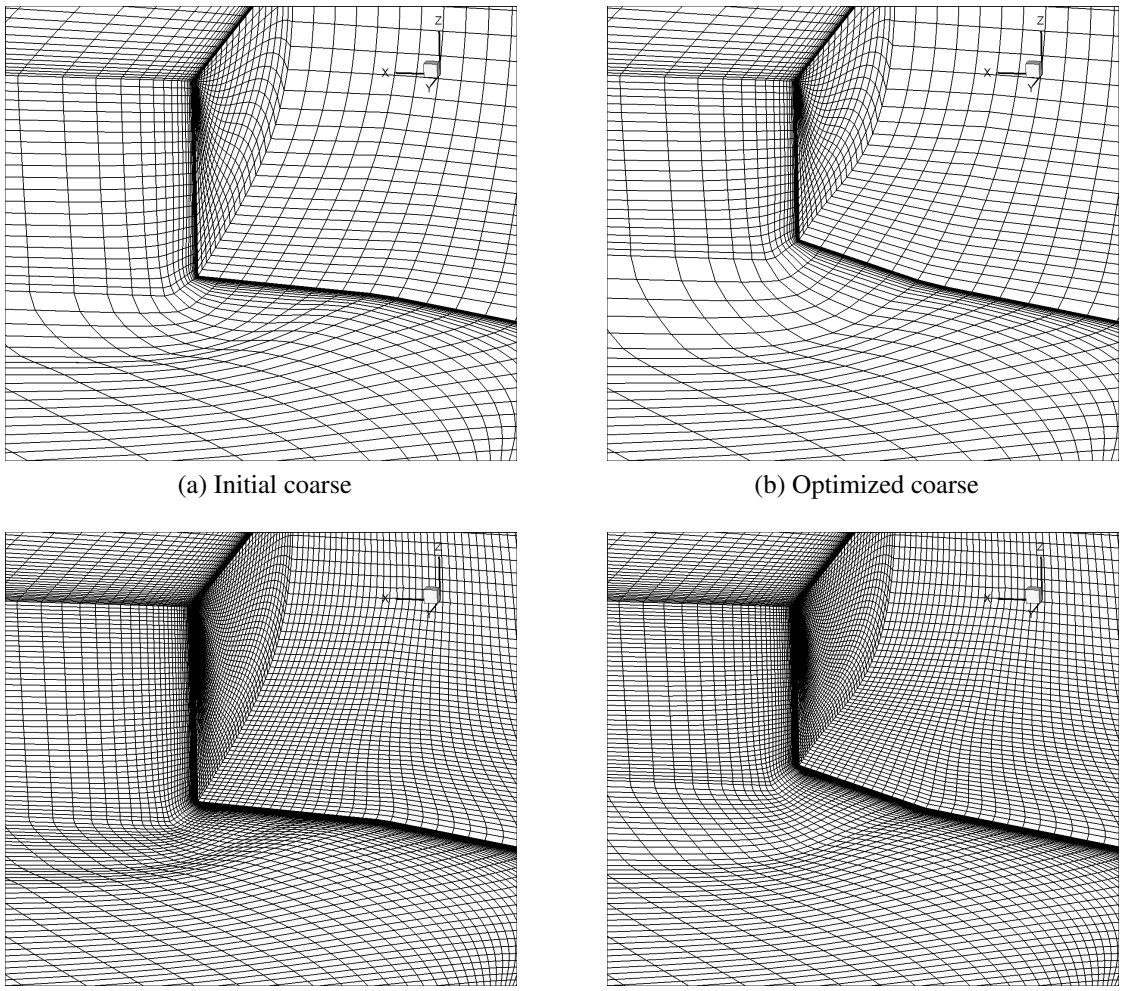

(a) Initial coarse

(b) Optimized coarse

(c) Initial fine grid

(d) Optimized fine grid

Figure 3.45: Computational grids around the ship stern.

Table 3.13: Comparison of the grid dimensions

	Coarse	Fine
Dimensions	121×25× 41	241×51× 81
No.Cells	115200	960000
No.Nodes	123041	991521

The computed hydrodynamic resistance coefficients based on the coarse and fine grids are compared in Table 3.14. Obviously, the absolute values of the fine grids are smaller than those of the coarse grids. The fine grid solutions are closer to the actual value since the measured data of the original KCS hull form is 6.38×10^{-4} [40]. While reduction of the pressure resistance coefficient in case of the coarse grids is approximately 6.2%, the computed pressure resistance coefficient of the optimized fine grid reduces approximately 5.7% from that of the initial fine grid. Furthermore, since the frictional resistance coefficients do not change between the initial and optimized hull forms for both grids, reduction of the pressure resistance coefficients yields the total resistance coefficients decrease. Reductions of the total resistance coefficients of the fine and coarse grids are approximately 1.6% and 2.4%, respectively. In summary, although the absolute values are different, the trends due to hull form modification are the same between the coarse and fine grids. Therefore, it can be concluded that the optimized results are validated through the grid dependency test.

Table 3.14: The computed resistance coefficients.

	Total resistance $C_t = \frac{R_t}{0.5\rho U^2 L_{pp}^2}$	Frictional resistance $C_f = \frac{R_f}{0.5\rho U^2 L_{pp}^2}$	Pressure resistance $C_p = \frac{R_p}{0.5\rho U^2 L_{pp}^2}$
Initial (coarse)	8.21×10^{-4}	5.14×10^{-4}	3.07×10^{-4}
Optimized (coarse)	8.02×10^{-4}	5.14×10^{-4}	2.89×10^{-4}
Initial (fine)	6.87×10^{-4}	4.95×10^{-4}	1.92×10^{-4}
Optimized (fine)	6.76×10^{-4}	4.95×10^{-4}	1.81×10^{-4}

Chapter 4

Concluding Remarks

The system of the stern shape optimization has been developed in this study. The system is the combination of a nonlinear optimizer by using the SQP method, a Navier-Stokes solver together with the hull shape modification method. The shape deformation is carried out by using modification function in such a way that the design variables are able to define efficiently new transom shapes which can minimize the objective function.

The present system has also been used for optimizing a stern shape of a hull form that is based on the original KCS to demonstrate the applicability of the present method with the pressure resistance coefficient is selected as the objective function. The optimized results decrease significantly from its initial values with the reductions of pressure resistance coefficient are more than 5% depending on the initial design values and the frameline modification functions.

The effects of the initial design variable values and of the modification functions to the final optimized results have been examined in this study. By the change of initial values x_{st} and the modification function from a linear form to a sine form, the final optimized results are significantly different in both reduction of pressure resistance and the optimized stern shapes. The difference of the final optimization result comes from the fact that the gradient of the objective function have different sign in each case whereupon the subsequent line search procedure carried out the search of vector d_z in the different directions. Therefore, it can be concluded that the optimized results are the local minimum solutions by using the present optimization method. An optimization method based on a better method such as the Genetic Algorithm (GA) method, therefore, should be taken into account to improve the present system.

The grid dependency test have also carried out for one representative case (Case III)

in the present study. The test results show good agreement with the optimization results. Then, it can be concluded that the optimized results are validated.

Further investigations on the transom shape optimization in combination with effects of the propellers, rudders, etc., should be taken into account to investigate the applicability of the present method in the practical design of a hull form.

Appendix A

Computed pressure resistance coefficients

A.1 The computed pressure resistance coefficients using linear function

Table A.1: Computed pressure resistance coefficient using the linear modification function

Linear function			
xst	dz	Computed Cp	Corrected Cp
0.49	-3.00E-03	1.60E-04	1.60E-04
0.49	0	1.56E-04	1.56E-04
0.49	3.00E-03	1.45E-04	1.45E-04
0.49	6.00E-03	1.45E-04	1.45E-04
0.49	9.00E-03	1.45E-04	1.45E-04
0.495	-3.00E-03	1.60E-04	1.60E-04
0.495	0	1.54E-04	1.54E-04
0.495	3.00E-03	1.45E-04	1.45E-04
0.495	6.00E-03	1.46E-04	1.46E-04
0.495	9.00E-03	1.45E-04	1.45E-04
0.5	-3.00E-03	1.59E-04	1.59E-04
0.5	0	1.52E-04	1.52E-04
0.5	3.00E-03	1.45E-04	1.45E-04

0.5	6.00E-03	1.45E-04	1.45E-04
0.5	9.00E-03	1.45E-04	1.45E-04
0.505	-3.00E-03	1.58E-04	1.58E-04
0.505	0	1.53E-04	1.53E-04
0.505	3.00E-03	1.45E-04	1.45E-04
0.505	6.00E-03	1.45E-04	1.45E-04
0.505	9.00E-03	1.47E-04	1.47E-04
0.51	-3.00E-03	999.9	1.58E-04
0.51	0	1.52E-04	1.52E-04
0.51	3.00E-03	1.46E-04	1.46E-04
0.51	6.00E-03	1.46E-04	1.46E-04
0.51	9.00E-03	1.48E-04	1.48E-04
0.515	-3.00E-03	999.9	1.58E-04
0.515	0	1.52E-04	1.52E-04
0.515	3.00E-03	1.47E-04	1.47E-04
0.515	6.00E-03	1.47E-04	1.47E-04
0.515	9.00E-03	1.51E-04	1.51E-04
0.52	-3.00E-03	999.9	1.58E-04
0.52	0	1.50E-04	1.50E-04
0.52	3.00E-03	1.46E-04	1.46E-04
0.52	6.00E-03	1.54E-04	1.54E-04
0.52	9.00E-03	1.62E-04	1.62E-04
0.525	-3.00E-03	999.9	1.58E-04
0.525	0	1.52E-04	1.52E-04
0.525	3.00E-03	1.51E-04	1.51E-04
0.525	6.00E-03	1.66E-04	1.66E-04
0.525	9.00E-03	1.94E-04	1.94E-04
0.49	-2.12E-03	1.57E-04	1.57E-04
0.495	-2.12E-03	1.57E-04	1.57E-04
0.5	-2.12E-03	1.54E-04	1.54E-04

0.505	-2.12E-03	1.56E-04	1.56E-04
0.51	-2.12E-03	1.51E-04	1.51E-04
0.515	-2.12E-03	1.46E-04	1.46E-04
0.52	-2.12E-03	999.9	1.46E-04
0.525	-2.12E-03	999.9	1.46E-04

A.2 The computed pressure resistance coefficients using sine function

Table A.2: Computed pressure resistance coefficient using the sine modification function

Sine function			
xst	dz	Computed Cp	Corrected Cp
0.49	-3.00E-03	1.61E-04	1.61E-04
0.49	0	1.54E-04	1.54E-04
0.49	3.00E-03	1.45E-04	1.45E-04
0.49	6.00E-03	1.45E-04	1.45E-04
0.49	9.00E-03	1.45E-04	1.45E-04
0.495	-3.00E-03	1.60E-04	1.60E-04
0.495	0	1.54E-04	1.54E-04
0.495	3.00E-03	1.46E-04	1.46E-04
0.495	6.00E-03	1.45E-04	1.45E-04
0.495	9.00E-03	1.45E-04	1.45E-04
0.5	-3.00E-03	1.59E-04	1.59E-04
0.5	0	1.55E-04	1.55E-04
0.5	3.00E-03	1.46E-04	1.46E-04
0.5	6.00E-03	1.44E-04	1.44E-04
0.5	9.00E-03	1.46E-04	1.46E-04
0.505	-3.00E-03	1.59E-04	1.59E-04
0.505	0	1.51E-04	1.51E-04

0.505	3.00E-03	1.45E-04	1.45E-04
0.505	6.00E-03	1.45E-04	1.45E-04
0.505	9.00E-03	1.44E-04	1.44E-04
0.51	-3.00E-03	999.9	1.59E-04
0.51	0	1.51E-04	1.51E-04
0.51	3.00E-03	1.46E-04	1.46E-04
0.51	6.00E-03	1.45E-04	1.45E-04
0.51	9.00E-03	1.49E-04	1.49E-04
0.515	-3.00E-03	999.9	1.59E-04
0.515	0	1.52E-04	1.52E-04
0.515	3.00E-03	1.46E-04	1.46E-04
0.515	6.00E-03	1.48E-04	1.48E-04
0.515	9.00E-03	1.50E-04	1.50E-04
0.52	-3.00E-03	999.9	1.59E-04
0.52	0	1.53E-04	1.53E-04
0.52	3.00E-03	1.48E-04	1.48E-04
0.52	6.00E-03	1.54E-04	1.54E-04
0.52	9.00E-03	1.67E-04	1.67E-04
0.49	-2.12E-03	1.59E-04	1.59E-04
0.495	-2.12E-03	1.58E-04	1.58E-04
0.5	-2.12E-03	1.57E-04	1.57E-04
0.505	-2.12E-03	1.54E-04	1.54E-04
0.51	-2.12E-03	1.52E-04	1.52E-04
0.515	-2.12E-03	1.48E-04	1.48E-04
0.52	-2.12E-03	999.9	1.48E-04
0.525	-2.12E-03	999.9	1.48E-04
0.49	-1.58E-03	1.57E-04	1.57E-04
0.495	-1.58E-03	1.57E-04	1.57E-04
0.5	-1.58E-03	1.56E-04	1.56E-04
0.505	-1.58E-03	1.55E-04	1.55E-04

0.51	-1.58E-03	1.50E-04	1.50E-04
0.515	-1.58E-03	1.50E-04	1.50E-04
0.52	-1.58E-03	1.48E-04	1.48E-04
0.525	-1.58E-03	999.9	1.48E-04
0.525	-3.00E-03	999.9	1.59E-04
0.525	0	1.51E-04	1.51E-04
0.525	3.00E-03	1.51E-04	1.51E-04
0.525	6.00E-03	1.65E-04	1.65E-04
0.525	9.00E-03	1.93E-04	1.93E-04

References

[1] IMO. *Guide line on the method of calculation of the attained energy efficiency design index (EEDI) for new ship*, 2012. URL http://www.imo.org/OurWork/Environment/PollutionPrevention/AirPollution/Documents/Technical%20and%20Operational%20Measures/MEPC.212%2863%29.pdf.

[2] IMO. *2012 Guide line for the development of a ship energy efficiency management plan (SEEMP)*, 2012. URL http://www.imo.org/OurWork/Environment/PollutionPrevention/AirPollution/Documents/Technical%20and%20Operational%20Measures/MEPC.213%2863%29.pdf.

[3] H. Soonhung Han, L. Yeon-Seung, and B. C. Young. Hydrodynamic hull form optimization using parametric models. *Journal of Marine Science Technology*, 17: 1–17, 2012.

[4] Kawasaki Heavy Industry. Kawasaki sew (stern end wedge). Technical report, Kawasaki Heavy Industry, 2013. URL http://www.khi.co.jp/english/ship/tech/performance/index.html.

[5] Wärtsilä. Boosting energy efficiency. Technical report, Wärtsilä, 2009. URL http://www.shippingtech.it/PDF/convegni%202010/2tecnologie1/Baan.pdf.

[6] L. Larson, F. Stern, and M. Visonneau. *Numerical ship hydrodynamic - An assessment of the Gothenburg 2010 Workshop*. Springer.com, 2014. ISBN 978-97-07-7188-8.

[7] J. B. Wackers, H. C. Raven, A. Vander Ploeg, G. B. Deng A. R. Staker, P. Queutey, M. Visonneau, T. Hino, and K. Ohashi. Free - surface viscous flow solution method for ship hydrodynamics. *Journal of Arch Comput Methods Eng*, 18:1–41, 2011.

[8] Kazuo Suzuki, Hisashi Kai, and Shigetoshi Kashiwabara. Studies on the optimization of stern hull form based on a potential flow solver. *Jounal of Marine Science and Technology*, 10:61–69, 2005.

[9] B. Zang. The optimization of the hull form with the minimum wave making resistance based on rankine-source method. *Journal of Hydrodynamic*, 21(2):277–284, 2009.

[10] B. Zang. Shape optimization of bow bulbs with minimum wave-making resistance based on rankine source method. *Journal of Shanghai Jiaotong University*, 21(2): 277–284, 2012.

[11] T. Hino. Shape optimization of practical ship hull forms using navier-stokes solver analysis. In *Proceeding of 7th International Conference on Numerical Ship Hydrodynamics*, 1999.

[12] Y. Tahara, S. Toyama, and T. Katsuchi. Cfd-based multi-objective optimization method for ship design. *International Journal for Numerical methods in fluids*, pages 499–527, 2006.

[13] Y. Tahara, D. Peri, and E. F. Campana dnd F. Stern. Computational fluid dynamics-based multiobjective optimization of a surface combatant using a global optimization method. *Journal of Marine Science and Technology*, 13:95–116, 2008.

[14] Y. Tahara, D. Peri, and E. F. Campana dnd F. Stern. Single - and multi objective functions design optimization of a fast multihull ship: numerical and experimental results. *Journal of Marine Science and Technology*, 16:412–433, 2011.

[15] M. G. Parsons, D. J. Singer, and C. M. Gaal. Mutlicriterion optimization of stern flap design. *Journal of Marine Technology and SNAME News*, 43:42–54, 2006.

[16] H. Kim and C. Yang. Hydrodynamic optimization of multihull ships. In *The 11th International Conference n Fast Sea Transportation FAST*, 9 2011.

[17] G. K. Saha, K. Suzuki, and H. Kai. Hydrodynamic optimization of a catamaran hull with large bow and stern bulbs installed on the center plane of catamaran. *Journal of Marine Sience and Technology*, 10:32–40, 2005.

[18] H. Miyata, Y. Doi, S. Takeuchi, H. Kajitani, and M. Kanai. Some effects of stern configurations on resistance and propulsion properties. *The Japan Society of Naval Architects and Ocean Engineers*, 193:45 –52, 1984.

[19] T. Yamano, F. Kuratani, T. Ogawa, T. Ikebuchi, and I. Funeno. Effects of transom stern bottom profile form on stern wave resistance a consideration on the effects of real stern end immersion. *Journal of Kansai Society of Naval Architechts*, 240: 11–19, 2003.

[20] T. Yamano, Y. Kusukoni, F. Kuratani, T. Ogawa, T. Ikebuchi, and I. Funeno. A consideration on desgin of wave-less transom stern form. *Journal of The Kansai Society of Narval Architects, Japan*, pages 55–61, 2005.

[21] A. Maki, J. Arai, K. Suzuki, T. Tsutsumoto, and Y. Miyachi. Research on resistance reduction due to stern flap installed on a surface ship (2nd report). *Journal of the Japan Society of Naval Architects and Ocean Engineering*, 18:407–410, 2014.

[22] P. T. Boggs and J. W. Tolle. *Sequential Quadratic Programming*, volume 4. ActaNumerica, 1995. URL http://journals.cambridge.org/abstract_S0962492900002518.

[23] T. Hino. Cfd-based estimation of propulsive performance in ship design. *Proceeding of the 26th Symposium on Naval Hydrodynamics*, Sept. 2006.

[24] T. Hino. Navier stokes computation of ship flows on unstructured grid. *Jounal of the Society of Naval Architects of Japan*, 182:9–15, 1998.

[25] T. Hino. An interface capturing method for free surface flow computation on unstructured grid. *Jounal of the Society of Naval Architects of Japan*, pages 177–183, 1999.

[26] T. Hino. A 3d unstructured grid method for incompressible viscousflow. *The Society of Naval Arcitects of Japan*, 19:9–15, 1997.

[27] P. L. Roe. Characteristic-based schemes fo the euler equations. *Annual Review of Fluid Mechanics*, 18:337 – 365, 1986.

[28] T. J. Barth. A 3-d upwind euler solver for unstructured meshes. *AIAA paper 91-1548-CP*, 1991.

[29] T. J. Barth and D. C. Jespersen. The design and application of upwind schemes on unstructured meshes. *AIAA paper 89-0366*, 1991.

[30] T. Hino. A study of grid dependence in navier-stokes solutions for free surface flows around ship hull. *Jounal of the Society of Naval Architects of Japan*, 1994.

[31] R. D. Rausch, J. T. Batina, and H. T. Y. Yang. Spatial adaption procedures on unstructured meshes for accurate unsteady aerodynamic flow computation. *AIAA Paper 91-1106*, 1991.

[32] D. C . Wilcox. *Turbulence Modeling for CFD*. July 1993.

[33] N. Hirata and T. Hino. A comperative study of zero- and once-equation turbulence model for ship flows. *Journal of Kansai Society Naval Architects*, 234:17–24, 2000.

[34] P. R. Spalart and S. R. Allmaras. A one-equation turbulence model for aerodynamic flows. *AIAA*, 1:5 – 21, 1994.

[35] M. Sussman, P. Smereka, and S. Osher. A level set approach for computing solutions to incompressible two - phase flow. *Journal of Computational Physis*, 146:114–159, 1994.

[36] SIMMAN 2008. Moeri container ship. In *SIMMAN 2008*. 2008. URL http://www.simman2008.dk/KCS/container.html.

[37] ITTC. *Recommended Procedures and Guidelines. CFD, Resistance and Flow Uncertainty Analysis in CFD Examples for Resistance and Flow*, 1999.

[38] ITTC. *Recommended Procedures and Guidelines. Uncertainty Analysis in CFD Verification and Validation Methodology and Procedures*, 2008.

[39] T. Hino. *CFD Workshop*. National Maritime Research Institute, March 2005.

[40] SH. Van, WJ. Kim, GT. Yim, DH. Kim, and CJ. Lee. Experimental investigation of the flow characteristics around practical hull form. *Proceedings of the 3rd Osaka colloquium on advanced CFD applications to ship flow and hull form design*, pages 215–227, 1998.